THE IMPACT OF PERTURBATIONS

ON FRUSTRATED MAGNETS

OREN OFER

THE IMPACT OF PERTURBATIONS ON
FRUSTRATED MAGNETS

RESEARCH THESIS

SUBMITTED IN PARTIAL FULFILLMENT OF THE

REQUIREMENTS

FOR THE DEGREE OF DOCTOR OF PHILOSOPHY

OREN OFER

ACKNOWLEDGMENT

Contents

CONTENTS

List of Figures

h

List of Tables

Abstract

Liquids are expected to crystallize at low temperatures. The only exception known is Helium, which can remain a liquid at 0 K, due to quantum fluctuations. Similarly, the spins in a magnet are expected to order at a temperature set by their Curie-Wiess temperature, θ_{CW}. Geometrically frustrated magnets represent an exception. In these systems, the pair-wise spin interactions cannot be simultaneously minimized due to the lattice symmetry. This frustration leads to unconventional magnetic ground states and macroscopic degeneracies.

In antiferromagnets, the spins align anti-parallel with each other. In the case of a triangular lattice, only two spins can align anti-parallel leaving the third spin frustrated and "baffled" not knowing what to do. The question we are interested in is: what will happen in this situation. So far, we've studied three examples of triangular frustrated lattices, the 2-dimensional kagome Zn-paratacamite, and the 3-dimensional pyrochlore lattice $Y_2Mo_2O_7$ and $Tb_2Ti_2O_7$. In the Zn-paratacamite we've found that the spins continue to fluctuate down to 60mK meaning no spin freezing, also μSR didn't detect any lattice deformation, NMR T_1 revealed that the excitation spectrum is gapless. In the $Y_2Mo_2O_7$ pyrochlore, we found that appearance of two (with a hint of a third) non-equivalent Y sites indicating two (or 3) domains or phases, high resolution x-ray powder diffraction revealed a magneto-elastic mechanism.

r

List of Symbols

T	Temperature
T_1	Spin-Lattice relaxation
T_2	Spin-Spin relaxation
J	Exchange Interaction
$\mathbf{S}$	Electronic Spin
$\mathbf{H}$	External Field
g	g-factor
μ_B	Bohr Magneton
$\mathbf{D}$	Dzyaloshinsky-Moriya vector
θ_{CW}	Currie-Weiss Temperature
C	Currie-Weiss constant
k_B	Boltzmann constant
ϵ	Normalized energy
P_μ	Muon polarization
ω	Angular Frequency
R_{LF}	Longitudinal Field Relaxation rate
R_{TF}	Transverse Field Relaxation rate
T_2^*	Inverse Transverse Field Relaxation

I	Spin Operator
$\rho(A)$	Distribution of couplings
ω_0	Larmor velocity
ν_0	Larmor frequency
γ	Gyromagnetic ratio
$\hbar$	Plank constant
K	Knight shift tensor
$\delta\phi$	Phase difference
e	Electron charge
i	Supercurrent
λ	Wavelength

Chapter 1

Frustrated Lattices

In this chapter we introduce the notion of geometric frustration in magnetic systems (§1.1)and focus on two lattices, the 2D kagomé (§1.2) and it's 3D equivalent pyrochlore (§1.3) lattices. The kagomé lattice is based on the triangular lattice by omitting a spin from every other site on every other line (see Fig.1.2a). The pyrochlore is the 3-dimensional cousin of the kagomé lattice, e.g. instead of having two dimensional triangles building up the lattice, the tetrahedra is the single unit cell, where in this case each tetrahedron has **2** spins frustrated (see Fig.1.4). The pyrochlore structure can be thought of alternating layers of triangular and kagomé lattices, with interaction between the planes (see Fig. 1.5).

1.1   Introduction

In a physical system, frustration arises from the fact that one cannot simultaneously minimize the different energies corresponding to multiple interactions that occur in the system. Here we focus on frustration that occurs due to the topology i.e., due

to the geometric constraints of the lattice. The interactions are the same for all spins on the lattice and it may include interactions between first, second .. nearest neighbors. For example, in an antiferromagnetic ising spins system situated on a triangular lattice one bond will always be *geometrically* frustrated (see Fig. 1.1).
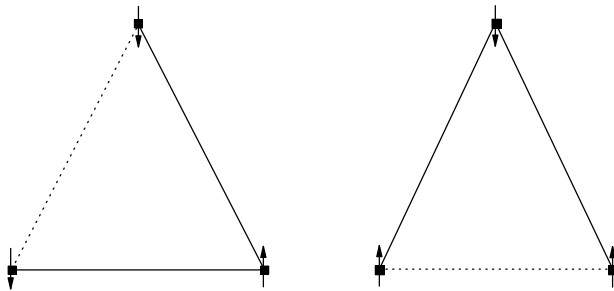
Figure 1.1: Geometric Frustration occurs when it is impossible to satisfy all bonds simultaneously. The dotted (full) line represents a frustrated (satisfied) bond.

In an antiferromagnetic lattice, there are two ways to frustrate. One, as shown above, the system can be frustrated due to the geometry (topological frustration). This is the case for three spins on a triangle, which can be expanded for the kagomé or pyrochlore lattices. A second way to frustration, is due to interactions. Such is the case in spin glasses where the crystallographic disorder creates a disorder in the interactions, i.e., the distance between magnetic moments is random thus so is the interaction.

Highly frustrated lattices have in common a large degenerate ground state ('super-degenerate ground-state'). This can easily be seen using the classical nearest-neighbor

antiferromagnetic heisenberg hamiltonian,

$$H = J \sum_{<i,j>} \mathbf{S}_i \cdot \mathbf{S}_j \qquad (1.1)$$

where the sum $< i, j >$ is over nearest-neighbor spins, and J is the strength of the exchange interaction. For q interacting spins, the hamiltonian can also be written,

$$H = J \sum_{<i,j>} \mathbf{S}_i \cdot \mathbf{S}_j = \frac{J}{2} \sum_{\Delta} \left(\sum_{i=1}^{q} \mathbf{S}_i \right)^2 - \frac{J}{2} \sum_i S_i^2 \qquad (1.2)$$

where the last sum is over triangles or tetrahedra. Without the constant term

$$H = \frac{J}{2} \sum_{\Delta} \mathbf{L}^2 \qquad (1.3)$$

where $\mathbf{L} = \sum_{i=1}^{q} \mathbf{S}_i$ is the total spin of a unit cell (when $\mathbf{S}$ are classical vector of unit length; $Jq\Delta S^2/2$ is just a constant). Therefore, we can see that the ground state is composed of states where the total spin $\mathbf{L}$ vanishes. Since there's an extensive possibilities to achieve such state, the ground state is degenerate macroscopically. This implies that at zero temperature the entropy is non zero and finite, which violates the third law of the thermodynamics. For example, it was calculated that on the kagomé lattice, the $S(T = 0) \simeq 0.502$ [6]. However, it is not necessary to have a macroscopic degeneracy in order to have a finite entropy as $T \to 0$. It is sufficient that the system will be gapless in its energy spectrum and that its density of states increases exponentially with the size of the system[7][8].

With the application of an external field, $\mathbf{H}$, the Hamiltonian (Eq.1.3) will now be added with a field term (Zeeman) $\mathcal{H}_Z = - \sum_i g\mu_B \mathbf{S}_i \cdot \mathbf{H}$, this yields the Hamiltonian,

$$\mathcal{H} = \frac{J}{2} \sum_{\Delta} \left(\mathbf{L}^2 - \frac{g\mu_B}{J} \mathbf{H} \cdot \mathbf{L} \right) = \frac{J}{2} \sum_{\Delta} \left(\mathbf{L} - \frac{\mathbf{h}}{2} \right)^2 - \frac{\mathbf{h}^2}{4} \qquad (1.4)$$

where $\mathbf{h} = (g\mu_B/J)\mathbf{H}$. Thus, the ground state will be such that $\mathbf{L} - \mathbf{h}/2 = 0$ or,

$$2J \sum_{i=1}^{q} \mathbf{S}_i - g\mu_B \mathbf{H} = 0.$$

We still have an extensive ways of producing such states. Furthermore, all states in this situation bare the same magnetization.

1.2   Kagomé Lattice

As seen in Eq. 1.3 the energy of the heisenberg model on this lattice can be minimized by placing the spins on each triangle pointing in three different dirrection 120° away from each other. Let us denote these three dirrection by A, B and C. Two configuration are known to posses long range order. One configuration is known as the $q = 0$ configuration. In this configuration the spins along any line of the kagomé is repeated in an alternating way (i.e., ABABAB or ACACAC etc.). The other configuration is known as the $\sqrt{3} \times \sqrt{3}$. In this case, the spins are aligned in a rotating sequence (i.e., ABCABC..). The extensive equivalent ground states is greatly enhanced since the spins do not have to be on the same plane ('noncoplanar' state). In Fig. 3.1b we demonstrate how the ground state degeneracy grows with the system size.

On the kagomé lattice, there are two mechanism which destroy such long range order. One is a chiral domain walls, in which spins are arranged in a different sense of rotation. (see Fig. 1.3). The generation of such a wall costs no energy however it increases the entropy. Another possibility is tunneling of spins from the A (or B) direction to the B direction (or A)[9]. This situation is possible in the $\sqrt{3} \times \sqrt{3}$ state.

a

b
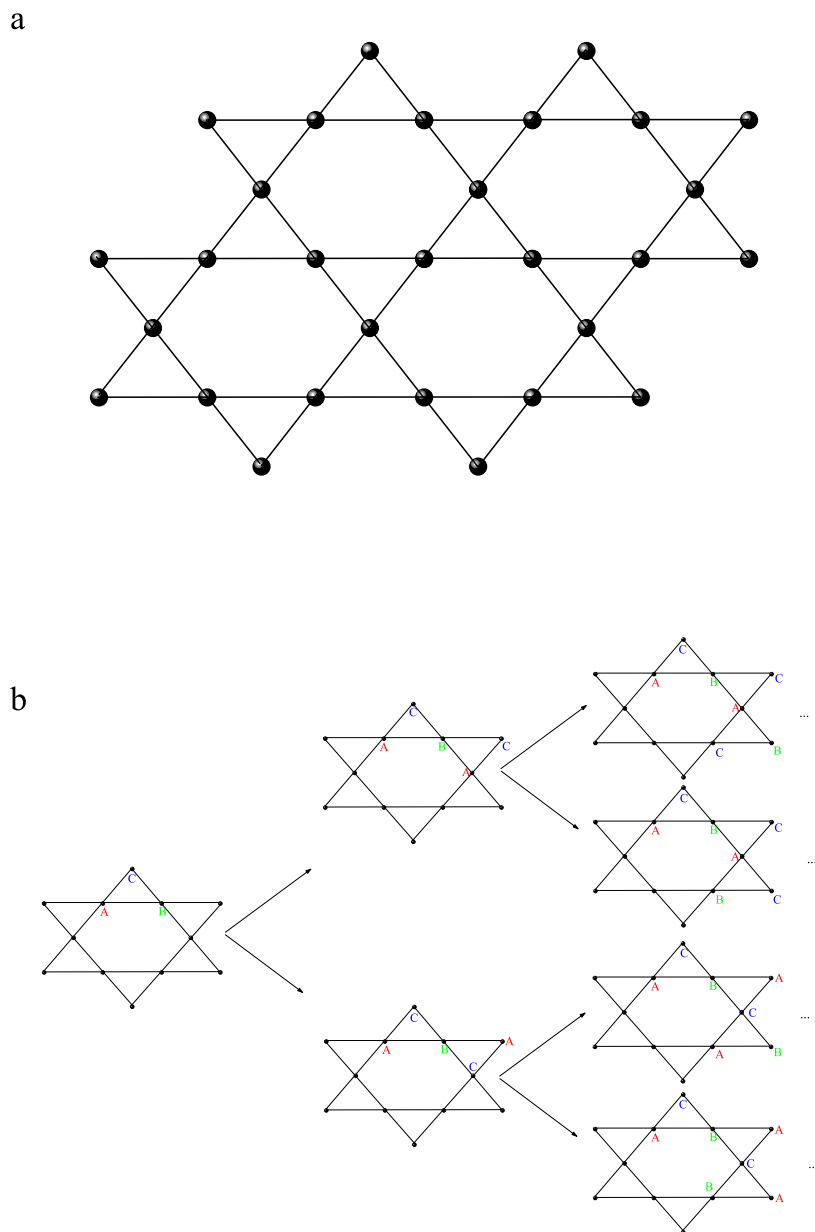
Figure 1.2: (a) The kagome lattice, (b) the possibility of the extensive ground state grows with the systems size
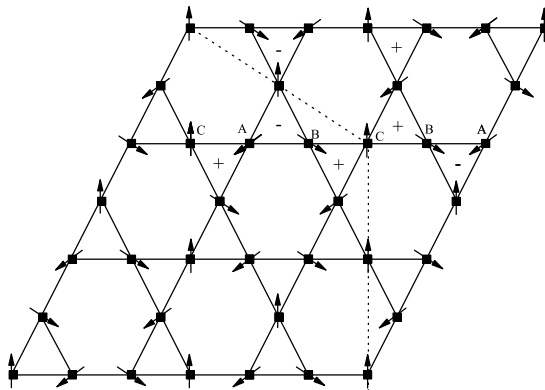
Figure 1.3: A possible chiral wall on the kagomé.

1.3 Pyrochlore Lattice

As in the kagomé case, the minimum energy state in the heisenberg model (as dictated by Eq.1.3), for each tetrahedron, is when the sum of the spins of a single unit vanishes. This constraint leaves two degrees of freedom which can be parameterized as two angles, as in Fig. 1.6, one is the angle between two spins, α, the other between two pairs of spins, φ.

Placing the tetrahedra on a lattice, imposes further constraint; however, we are still left with one degree of freedom for each tetrahedron. Therefore, each ground state can be described by a number of continuous degrees of freedom which is proportional to the number of units creating the macroscopic lattice.

The presence of a macroscopically degenerate ground state has a profound impact on the low temperature modes of the system. In the harmonic approximation the pyrochlore lattice exhibits soft modes, in which have zero energy. These soft
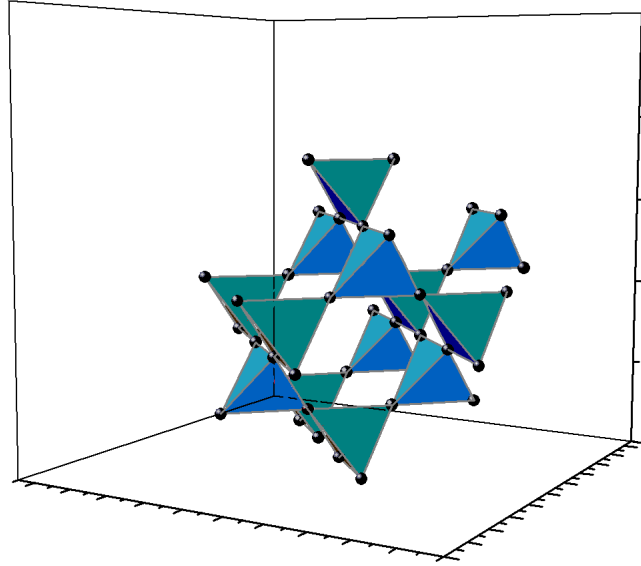
Figure 1.4: The pyrochlore lattice - a corner sharing tetrahedra.

modes correspond to displacements in phase space that lie within the ground state manifold[10]. If a finite number of spins are able to rotate without an energy cost, then correlations can effectively be destroyed.

Thermal Fluctuations and quantum flucuations

In most materials thermal fluctuations destroy any long-range order however, in a geometrically frustrated magnet thermal fluctuations can create ordering[11]. In a geometrically frustrated magnet the degeneracy is very sensitive to small perturbations. Thus, a thermal fluctuation can preferentially select a subset from the ground
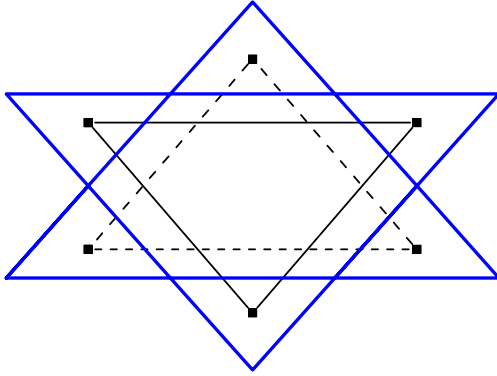
Figure 1.5: The (100) projection of the pyrochlore lattice. The projection shows the layered structure of the lattice - triangular (dashed black lines), kagomé (blue lines), triangular (black lines)
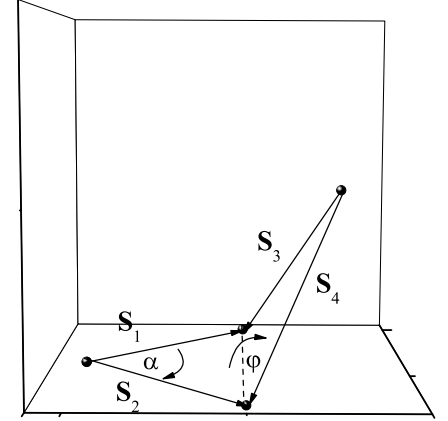
Figure 1.6: Four spins that satisfy $\sum_{i=1}^{4} \mathbf{S}_i = 0$

state manifold. Therefore long-range order can form in the system at low temperatures. Due to the ground state degeneracy, one can go between states with no energy cost. Therefore, in a system that doesn't go order by disorder there should not be a phase transition out of the paramagnetic state. It was pointed out that in a geometrically frustrated magnet with sufficiently large levels of defects, such as a doped pyrochlore antiferromagnet should undergo a phase transition into a spin-glass at a finite temperature[12]. In the kagomé lattice however, the situtation is different. In a pure kagomé thermal fluctuations cause the system to select a nematic state (no topological order but long-range orientational order) and not a conventional spin glass behavior.

In addition to thermal fluctuations, in frustrated magnets, quantum fluctuations

can help select a specific configuration. These fluctuations arise from the Heisenberg uncertainty principle, i.e., from our inherent inability to specify S_x, S_y and S_z simultaneously. Thus, when two neighboring spins are, on average, parallel ($\hat{z}$), there is still residual interaction between their perpendicular ($\hat{x}$ or $\hat{y}$) components.

1.3.1   Breaking the groundstate degeneracy

The Heisenberg hamiltonian, Eq. 1.3 therefore leads to macroscopic degeneracy. Thus the frustrated system is very sensitive to additional terms in the hamiltonian. We concentrate on 3 possible cases: lattice distortions (through a magneto-elastic term), changes in the susceptibility (through a Dzyaloshinsky-Moriya interaction) and an exchange anisotropy. There are other possibilities such as next nearest neighbors interactions[13] or dipolar interactions[14] or others that we do not expand on here.

Magnetoelastic Distortion

In order to break the groundstate degeneracy, it has been suggested that the lattice distorts[15][16]. In such distortions, the increase in the elastic energy is outweighed by a reduction in the magnetic energy. This is similar to a cooperative Jahn-Teller effect where a degeneracy of the electron groundstate in a molecule is broken by a distortion of the molecule. The difference of course, is that in geometrically frustrated magnets there is a spin rather than an electronic degeneracy that drives the distortion.

A magnetoelastic term causes a distortion which results in shorter and larger bonds in each unitcell (tetrahedron or triangle). Assuming $J = J(r)$, the shorter and longer bonds will posses $J_s > J$ and $J_l < J$ respectively. Thus, it becomes favorable to align the spins anti-parallel in the short bonds and parallel in long bonds. The

hamiltonian with a magnetoelastic term can be written as,

$$\mathcal{H} = J \sum_{<i,j>} \mathbf{S}_i \cdot \mathbf{S}_j - \frac{1}{3k} \left(\frac{dJ}{dr}\right)^2 \sum_{i>j} (\mathbf{S}_i \cdot \mathbf{S}_j)^2 \qquad (1.5)$$

where k is the elastic energy (spring) constant. Thus, the magnetoelastic term causes the spins to grow closer or farther depending on their relative orientation and the sign of the derivative of the exchange constant. In the most spectacular case the magneto-
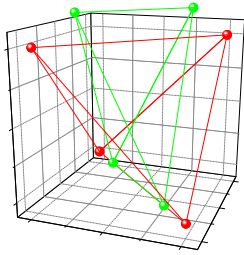
Figure 1.7: A perfect (red) and a distorted (green) pyrochlore
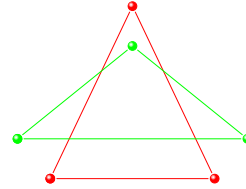
Figure 1.8: A perfect (red) and a distorted (green) triangle.

elastic coupling has been evidenced to lead long range spin order accompanied by a new lattice structure such as in $ZnCr_2O_4$ [17] and $CdCr_2O_4$[18]. Alternatively, this coupling might also be responsible to a short range spin order and short range lattice deformation in $Y_2Mo_2O_7$[19, 5, 20], in which the original lattice structure is preserved on average.

Dzyaloshinsky-Moriya

It has been shown, both theoretically[21, 22, 23, 24] and experimentally[25], that Dzyaloshinky-Moriya Interactions (DMI) can be significant in the magnetic behavior of kagomé and pyrochlore lattices. The DMI term in the hamiltonian is represented

as,

$$\mathcal{H}_{DM} = \sum_{<i,j>} \mathbf{D}_{ij} \cdot (S_i \times S_j)$$

where $\mathbf{D}_{ij} \ll J_{ij}$ is the DM vector which defines the interaction. $\mathbf{D}_{ij}$ is antisymmetric with regards to site permutation, $\mathbf{D}_{ij} = -\mathbf{D}_{ji}$. A rigorous derivation of the contribution of this interaction term is presented in Appendix B, here we outline the contributions of the DM interaction in mean field approach.

In this approach, we write the Hamiltonian with DMI as,

$$\mathcal{H} = -\sum_i \mathbf{S}_i \cdot \left(J \sum_{j \neq i} \mathbf{S}_j + \mathbf{D}_{ij} \times \mathbf{S}_j + g\mu_B H \right). \tag{1.6}$$

By replacing this $\mathbf{S}_j$ with $M/g\mu_B$ the Hamiltonian of Eq. 1.6 can be written as $\mathcal{H} = -g\mu_B \sum_i \mathbf{S}_i \cdot \mathbf{H}_{eff}$ where

$$\mathbf{H}_{eff} = \frac{1}{g\mu_B} \cdot \sum_i \left(J\mathbf{S}_i + \mathbf{D}_{ij} \times \mathbf{S}_j \right) + H$$

However, in the kagome (see Fig.1.9) and pyrochlore lattices

$$\sum_{j \neq i} \mathbf{D}_{ij} = 0 \tag{1.7}$$

and the DM interaction does not contribute in the mean field level.

Exchange Anisotropy

The exchange anisotropy Hamiltonian is written as,

$$\mathcal{H} = -\sum_{<i,j>} \left(J_z S_i^z S_j^z + J_\perp S_i^\perp S_j^\perp \right) - g\mu_B \sum_i \mathbf{S}_i \cdot \mathbf{H} \tag{1.8}$$

we take a mean field approximation, and receive that the magnetization measured in different directions differs,

$$\mathbf{M} = \frac{C}{T} \cdot \mathbf{H}_{eff} \tag{1.9}$$

$$M_{z,\perp} = \frac{C}{T + \theta_{CW}^{z,\perp}} \cdot H_{z,\perp} \tag{1.10}$$
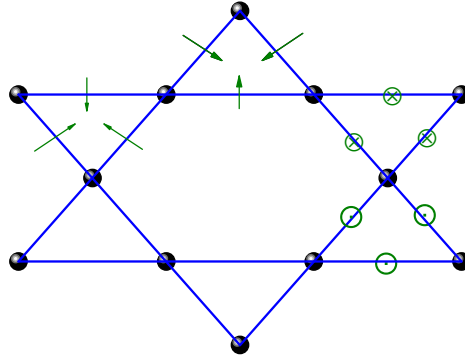
Figure 1.9: Orientation of the in-plane and out-of-plane components of the DM vector.

where $\theta_{CW}^{z,\perp} = C(g\mu_B)^{-2}J_{z,\perp}$.

In the kagome case exchange anisotropy leads to an unusual ground state. Accordingly the spins are coplanar, with a single angle, φ, which determines the direction of the spins (see Fig. 1.12). We look at the anisotropic super-exchange hamiltonian, $\mathcal{H} = \sum_{<i,j>} J_x S_i^x S_j^x + J_z S_i^z S_j^z$, and assume all spins are of the same size. Thus, we can write the energy as a function of the super-exchange constants and the angle φ. We observe the contributions of spins in the $\hat{x} - \hat{z}$ plane along each axis,

$$\mathbf{S}_1 = S(\sin\varphi, 0, \cos\varphi) \tag{1.11}$$

$$\mathbf{S}_2 = S(-\sin\varphi, 0, \cos\varphi)$$

$$\mathbf{S}_3 = S(0, 0, 1) \tag{1.12}$$

thus,

$$E(J_x, J_z, \varphi) = -J_x \sin^2\varphi + J_z \cos\varphi(\cos\varphi + 2) \ . \tag{1.13}$$
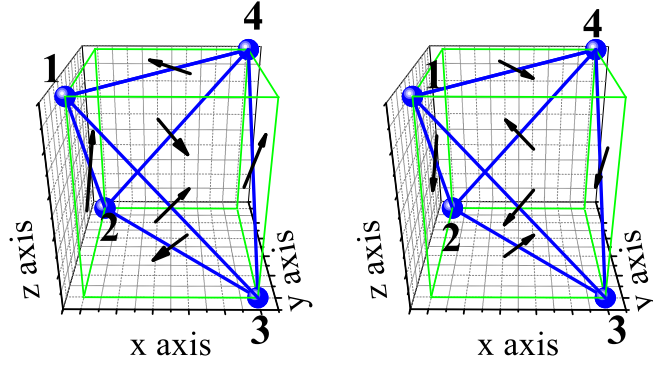
Figure 1.10: DM vectors on the pyrochlore lattice are possible in two scenarios.

Minimizing the energy with respect to φ results in,

$$\cos \varphi = -\frac{J_z}{J_z + J_x} \ . \tag{1.14}$$

Thus, in the isotropic case (where $J_z = J_x$), $\cos \varphi = -1/2$ hence $\varphi = 120°$ as expected and the magnetization vanishes. In the anisotropic case this leads to a finite magnetization: the magnetization per spin along $\hat{z}$ would be,

$$M = \frac{1 + 2\cos\varphi}{3} \tag{1.15}$$

the $1/3$ factor is for 3 spins, $1 + 2\cos\varphi$ is from one spin pointing along $\hat{z}$ and the two others pointing anti-parallel with an angle φ. Thus, the anisotropic kagomé is expected to have a ferromagnetic ground state.
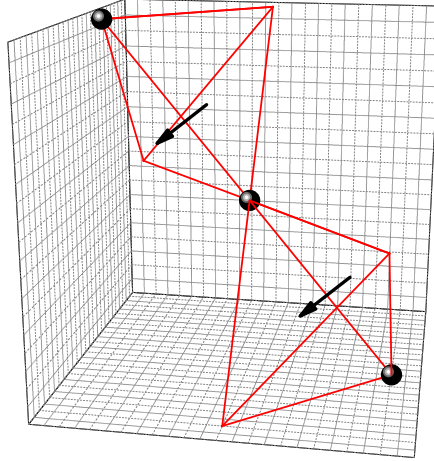
Figure 1.11: Expansion of the single tetrahedra DMI onto the pyrochlore lattice.

1.4 Existing Data

Strongly frustrated compounds have also a characteristic susceptibility fingerprint (See Fig.1.13)- their inverse susceptibility, χ^{-1}, follows the usual Curie-Wiess law down to temperatures well below of their expected ordering temperature θ_{CW}. At some temperature, $T = T_F \ll \theta_{CW}$, a deviation from the linear behavior occur. Different compounds enter different states at $T < T_F$. This state can be ordered (such is the case in $Y_2Ru_2O_7$) or glassy (as in the case of $Y_2Mo_2O_7$). In some circumstance it can be neither, such is the case of $Y_2Tb_2O_7$, this compound remains in a fluctuating state down to extremely low temperatures (50 mK). The smallness of the frustration parameter, $f = T_F/\theta_{CW}$, represents a 'strong' geometric frustration. At $T > \theta_{CW}$ the state is usually paramagnetic, whereas at $T < T_F$ the state differs from one
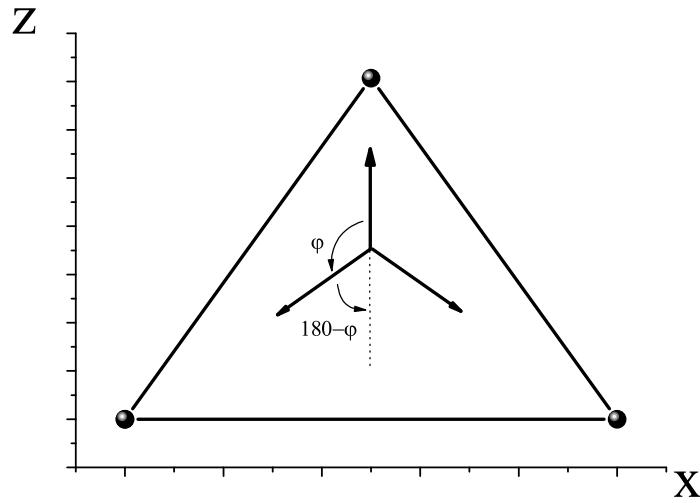
Figure 1.12: The Ising kagomé lattice has one angle which defines the orientation of the spins in the triangle unit cell.

compound to another. At $T_F < T < \theta_{CW}$, the intermediate regime, is the cooperative paramagnetic, where spin correlations remain weak although the temperature is below the scale set by the interactions.

1.4.1   Spin $1/2$ Kagomé $\mathbf{Zn}_x\mathbf{Cu}_{4-x}(\mathbf{OH})_2\mathbf{Cl}_2$

The Herbertsmithite is considered the Holy Grail compound since it is the first experimental realization of a perfect S=1/2 Kagomé structure. It is a part of the Paratacamite family $Zn_xCu_{4-x}(OH)_6Cl_2$. The Herbertsmithite ($x = 1$) is named after Herbert Smith who first discovered it in a mine in Chile in the early 1970s. The Paratacamite family can be found in mines in Iran as well. Unfortunately, the naturally occurring single crystals lack the purity needed for physical measurements. The
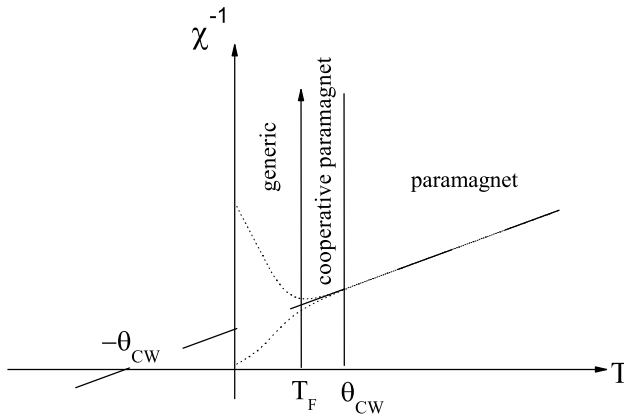
Figure 1.13: Characteristic susceptibility of a highly frustrated compound, below T_F the susceptibility behavior is compound specific.

magnetism of the Paratacamite family is obtained from the Cu^{2+} electronic spin carrying a S=1/2. The electronic spin couple to its nearest neighbors through oxygen super-exchange.

The parent compound of the family is the Clinoatacamite, ($x = 0$, $Cu_2(OH)_3Cl$) which has a distorted pyrochlore structure. The system consists of Cu tetrahedra with a distortion along and perpendicular to the kagomé planes. The structure reveals three different Cu sites, two in the plane and another out of the plane (see Fig.1.14). At $x > 0.33$ the distortion along the kagomé plane is removed and the system consists of two different Cu sites. The Cu sites in the kagomé plane are identical, leaving elongated tetrahedra. When all out-of-plane Cu^{2+} are replaced with non-magnetic Zn^{2+} we obtain the Herbertsmithite, where the kagomé planes are fully decoupled (see Fig.1.14).

X-ray diffraction reveals the unit cell parameters of the Herbertsmithite, which is
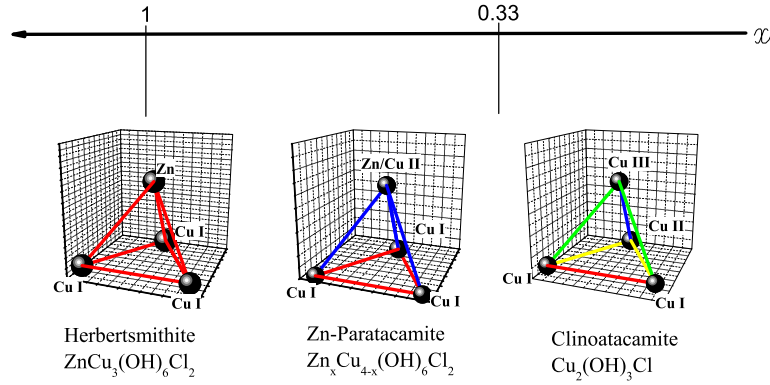
Figure 1.14: Three members of the paratacamite family. Each bond color represent a different bond length. The two extremes, the Clinoatacamite and the Hebertsmithite, $x = 0$ and $x = 1$, are shown on the left and right hand-sides respectively.

found to have a=b=6.834Å and c=14.032Å, the three vectors of the unit cell form the angles $\alpha = \beta = 90°$ and $\gamma = 120°$. Thus the planes are well separated, thereby creating a perfect kagomé lattice. The octahedron around a planar Cu site consists of four groups of hydroxyl (OH^-) and two chlorine ions (Cl^-). This octahedron is elongated along the Cl-Cl axis. On the other hand, the octahedron around a Zn site (between planes) has six hydroxyl groups, all with the same bond lengths creating a symmetric octahedron. Thus, this site is of higher symmetry relative to the in-plane Cu site. The original sample makers note that because of this symmetry difference, during the synthesis of the sample, Cu occupy preferentially the plane sites whereas

the Zn remain out the plane. Furthermore, X-ray powder diffraction analysis indicate a better likelihood of a 100% Cu on the kagome site and the interlayer site covered with 100% Zn. [26].

Various compositions of the paratacamite family were studied by susceptibility measurements[27]. The inverse susceptibility (χ^{-1}) data shows antiferromagnetic correlations, but shows no signature of a transition at the measured temperature range $2 < T < 350$ K. At high temperatures $(T > 100$ K) the susceptibility shows a Curie-Wiess behavior and a linear fit to $\chi^{-1}(T > 100)$ reveals θ_{CW} to be in the 200-300 K range (200 K for $x = 0$ then increases almost linearly to 314 K for $x = 1$). The exchange constant is can then be calculated from[28]

$$\theta_{CW} = \frac{zJ}{2k_B}$$

$$J = 190 \ K \sim 170 \ meV.$$

Below ~ 75 K a sharp increase in the susceptibility occurs, deviating from the ideal kagomé Heisenberg model[27] [29]. This upturn was accounted for by DMI [22, 30] or anisotropy in the bonds [31, 32]. Recent low temperature[33] $(0.1 < T < 3$ K) magnetization of the hebertsmithite was measured using dc-magnetization with a squid magnetometer. At low temperatures, $0.1 < T < 10$ K the susceptibility increases more rapidly down to $\simeq 0.5$ K where it eventually saturates. Even at these low T there is no sign of a magnetic transition. The study suggested that the low temperature magnetization is dominated by defect contribution[33].However, free impurities, or even interacting impurities that generate an additional ferromagnetic Curie-Weiss law [22][34], have been shown not to describe this upturn completely.

Several neutron studies [35, 36, 37] performed on powder samples of Herbert-smithite. Ref. [35, 36] indicated that there might be a presence of defects in the

system. They attributed the anomalous behavior to a substitution of Cu^{2+}-Zn^{2+}. In such a case there's two magnetic defects: (i) an introduction of a non-magnetic Zn^{2+} ion in the kagomé plane, and (ii) the presence of a magnetic Cu^{2+} ion between the planes. Calculation suggests approximately 8% Zn ions in the kagomé plane. However, The super exchange interaction between nearest-neighboring Cu^{2+} moments mediated via oxygen is very sensitive to the Cu-O-Cu bond angle, θ, and it changes from strongly antiferromagnetic when $\theta = 180°$, to zero when $\theta \sim 95°$ to ferromagnetic $\theta < 95°$. From neutrons data refinement, θ found to be $115 \lesssim \theta < 119.2°$, indicating that the interactions between the kagome Cu^{2+} and the doped triangular Cu^{2+} spins are weak, which makes the Cu moments at the triangular sites almost independent spins and thus makes $Zn_x Cu_{4-x}(OH)_6 Cl_2$ a weakly coupled kagome system for all Zn concentrations $x < 1$. Susceptibility measurements from the same group suggested a 5% to 10% defects.

Local probes measurements were also performed. NMR was performed on different nuclei (for the atomic environment, see Fig. 1.15), ^{1}H[3], ^{17}O in enriched samples[1], ^{63}Cu[2] and ^{35}Cl[2].

Proton

The proton posses a nuclear spin 1/2 which has a big gyromagnetic ratio ($\gamma = 42.57$ MHz/T) and gives an excellent NMR signal. The NMR spectrum does not reveal any shift, which indicated the absence of hyperfine coupling between the protons and the copper atoms. Thus this nuclei could not reveal susceptibility information on the kagome planes.[3]
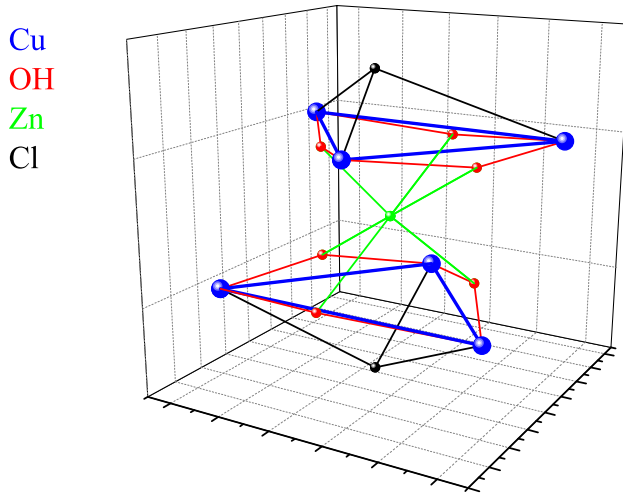
Figure 1.15: The structure of the Hertbertsmithite. Two Cu triangles of successive kagome planes are represented.

Copper

The copper nuclei has two isotopes carrying both a spin 3/2. The NMR spectrum was studied in detail at temperature $1.9 < T < 40$ K[2]. Above that temperature the relaxation becomes too fast so Cu NMR signal cannot be detected. The ^{63}Cu NMR shift measurements were not successful due to technical difficulties. However, T_1 measurements were carried out indicating that below 30 K, $1/T_1$ decreases with negative curvature revealing that paramagnetic spin fluctuations show no magnetic instabilities.

Oxygen-17

The oxygen is therefore found to be ideal for probing the magnetic kagome planes since they are bound to planar coppers. The ^{17}O carries a spin $5/2$ thus a unique central $-1/2 \rightarrow 1/2$ transition is observed. The shift of this peak reflects the susceptibility of the two neighboring Cu ($K \propto A\chi_{Cu}$ - where $A = 35kG/\mu_B$ is the hyperfine constant between O and Cu^{+2} electronic orbital). This shift is depict in Fig. 1.16 as the intrinsic ^{17}O shift. In the observed ^{17}O line, two different central transitions were found indicating a possibility of the existence of two different environments. As with previous neutrons scattering this second environment was attributed to a possible Zn/Cu interchange. This shift is noted as ^{17}O defect. Spin-lattice relaxation, T_1, were also conducted.
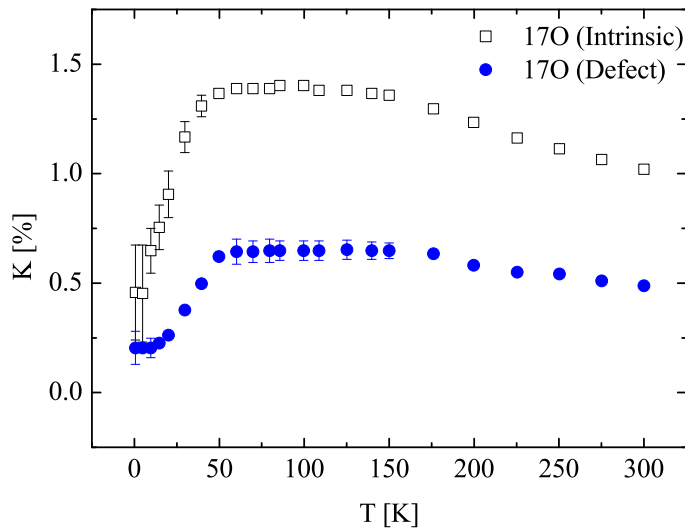
Figure 1.16: ^{17}O NMR Knight shifts. Data is taken from Ref.[1]

Chlorine

In parallel to our work, a different group[2] have taken dynamic and static measurements with great precision on oriented powder samples. Here we describe these measurements.

Due to the orientation of the samples, it was possible to follow the NMR spectrum down to 4.2 K. The center peak of the line, which originated from oriented crystallines, was measured with high accuracy, thus extracting the shift corresponding to this resonance ($^{35}K_{peak}$). Since the ^{35}Cl lineshape begins to tail off to lower fields with decreasing temperatures, an additional shift measurements were taken at the half-intensity position on the lower field side ($^{35}K_{1/2}$) as well at the edge of the line ($^{35}K_{edge}$). These shifts are shown in Fig.1.17 along with the squid measurement from §3.1.1. Clearly, the $^{35}K_{1/2}$ behaves as the bulk squid measurements which therefore represent a bulk average of this susceptibility. The $^{35}K_{peak}$ and $^{35}K_{edge}$ at low-T behaves differently, it follows Curie-Wiess down to ~ 25 K, whereas the bulk susceptibility begins to deviate below ~ 100 K. The $1/T_1$ data agreed with our premier measurements (§3.1.1) ^{17}O and ^{63}Cu NMR.

To conclude these NMR measurements, the T variations of the NMR T_1 of ^{17}O ^{63}Cu and ^{35}Cl are similar. These measurements point to a zero-gap,

$$T_1^{-1} \propto \exp(-\Delta/T) \tag{1.16}$$

where Δ is the energy gap, data fits shows $\Delta < 1\ eV \ll J$. The shift (susceptibility) however, differs one from another as well as from bulk measurements except from ^{35}Cl.
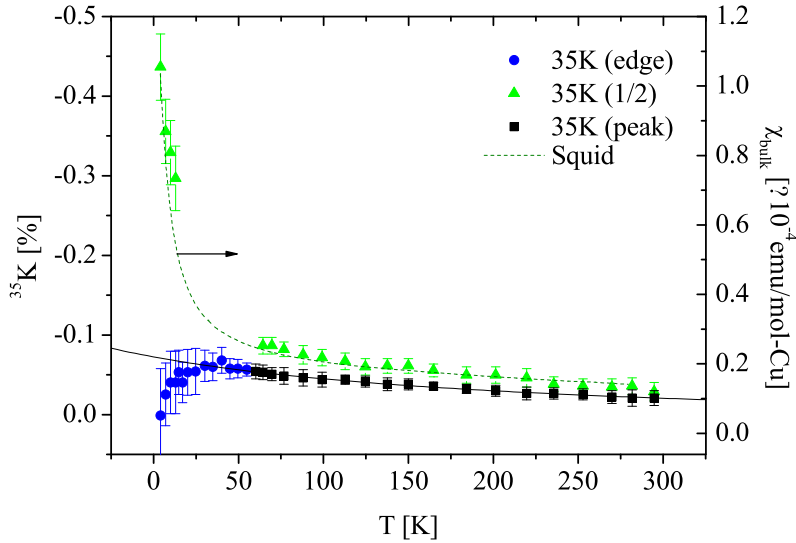
Figure 1.17: ^{35}Cl NMR Knight shifts. The solid line is a fit to a Curie-Wiess behavior, $-22.14973/(x + \theta_{CW}) + 0.02062$ where $\theta_{CW} = -237(40)$ K. Cl shifts are taken from Ref.[2]. The bulk susceptibility, χ_{bulk} measured using a SQUID.

1.4.2 $A_2B_2O_7$ Pyrochlores

The oxide pyrochlores family, with the chemical formula $A_2B_2O_7$, has a variety of magnetic compounds each with its own magnetic characteristics. A more general chemical formula is $A_2B_2O_6O'$. In Fig.1.19 we depict the A, B and O sites. The A and B sites, each form a network of corner-sharing tetrahedra, forming an interwoven kagomé nets. However, the A and B sites differs in their oxygen environment, the A site has an eightfold oxygen coordination and is occupied by a rare-earth ion (such as Y ($S = 1/2$), Nd ($S = 7/2$), Tb ($S = 3/2$) and others). The B site has a six-fold coordination and is occupied by a metal ion (as Mo ($S = 1$), Ru($S = 3/2$, $S = 5/2$), Mn and others). The O' site creates an FCC structure, since the O' sites are situated
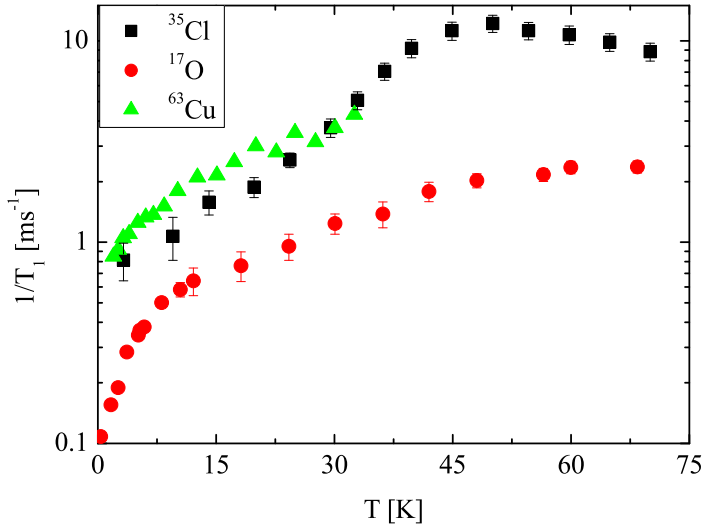
Figure 1.18: Comparison of T_1 measurements for different nuclei, ^{17}O, ^{35}Cl and ^{63}Cu. Data taken from [3] (^{17}O) and [2] (^{35}Cl, ^{63}Cu).

in the middle of the A-site tetrahedra the pyrochlore lattice can be seen as an FCC structure (see Fig. 1.20).

$Y_2Mo_2O_7$

$Y_2Mo_2O_7$ is a narrow band gap semiconductor, its magnetic Mo^{4+} ($S = 1$) forms a pyrochlore lattice. Susceptibility indicates antiferromagnetic interactions ($\theta_{CW} \sim$ 200 K) with an effective moment of $2.55\mu_B$. Early susceptibility measurements reveal evidence for a spin-glass transition at $T_g \sim 22$ K[39][40]. Fig. 1.21 shows the suscep- tibility with (zero) field splitting in the susceptibility which is indicative of spin-glass transition. This transition is appears without the presence of disorder (randomness) since the samples used were of very high purity (less than 1%). This spin glass tran- sition was also observed by nonlinear dc susceptibility, χ_{nl}[39]. χ_{nl} diverges at T_g in
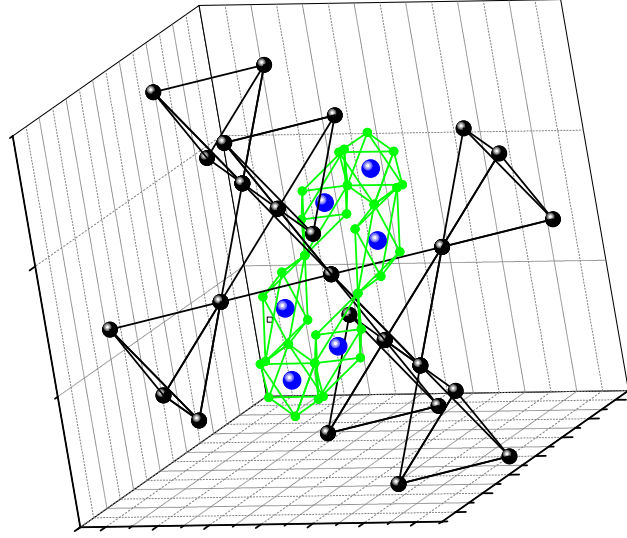
Figure 1.19: The pyrochlore lattice showing the A (black spheres), B (blue spheres)
and O (green circles) sites

a thermodynamic spin glass phase transition as,

$$\chi_{nl} \sim t^{-\gamma} = \left(\frac{T - T_g}{T_g}\right)^{-\gamma} \tag{1.17}$$

a detailed investigations on the critical exponents reveal similarity to those found in
conventional spin-glasses despite the immeasurably small disorder in $Y_2Mo_2O_7$[39].
A similar analysis to other frustrated lattices such as $SrCu_8Ga_4O_19$ (SCGO) demon-
strate resemblance to typical spin glass (a field splitting of the linear susceptibility)
however, scaling of the non linear susceptibility is inconsistent with conventional spin
glasses behavior.

The first indication of randomness (distortion) in the structure of $Y_2Mo_2O_7$ was
found by X-ray absorption fine structure (XAFS)[20]. The Mo-Mo pair distance
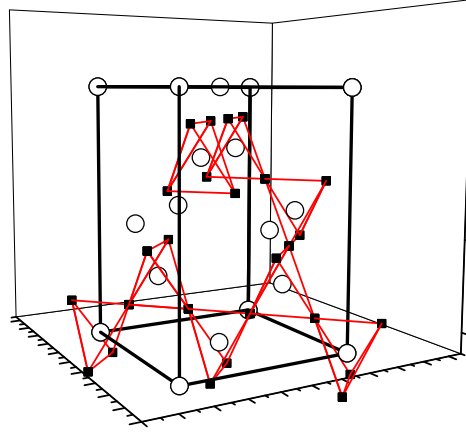
Figure 1.20: The pyrochlore as an FCC. Showing the A (black dots) and O′ (hollow circles) sites

has a relatively large amount of pair-distance disorder (about 0.15Å compared to 3.5Å Mo-Mo mean pair separation). This results indicate that although the high purity of the sample, there is still bond modulation. Thus, a disorder in J exists for spin-glass transition to occur. The second indication of disorder was from ^{89}Y NMR[19]. A multiple discrete values of the local susceptibility at the Y sites were found at $T > 92$ K. These discrete values results from small discrete changes in the Mo-Mo bond lengths. At high temperatures, $T > |\theta_{CW}|$ the NMR line is smooth, whereas as the temperature decreases below θ_{CW}, more discrete changes appear in the spectra. Therefore, this distortion along the Mo sublattice relieves the magnetic geometric frustration. The third indication, of such magneto-elastic distortion, was
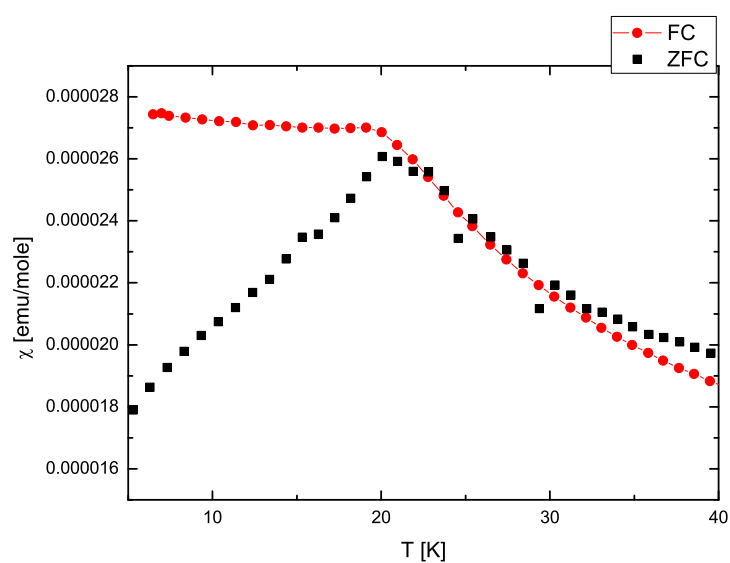
Figure 1.21: Zero-field-cooled (ZFC) and field-cooled (FC) susceptibility measurements of $Y_2Mo_2O_7$. A transition to spin glass is observed at $T \sim 20$ K

from μSR[5]. It was shown that at T_g, the static field distributions, which is associated with lattice deformation, increased with applied magnetic field. Furthermore, the ratio between the static field distribution width, Δ, and the susceptibility was shown to be non linear, hence the distribution of muon coupling to electronic spins is temperature dependent (see §2.1.1). This was concluded to be the result of random lattice distortions similar to that seen in the NMR.

Tb$_2$Ti$_2$O$_7$

The Tb$_2$Ti$_2$O$_7$ is unique in the oxide pyrochlore family A$_2$B$_2$O$_7$ being a spin-liquid; despite its short-range AFM correlations at temperatures lower than 100K, the Tb$_2$Ti$_2$O$_7$ remains in a fluctuating paramagnetic state down to 70mK (susceptibility indicate $\theta_{CW} = -19$ K)[41]. A cluster glassy behavior is observed by susceptibility below 0.2 K[42]. However, it was demonstrated that, under pressure[43] high magnetic field field[44] or both[45], Tb$_2$Ti$_2$O$_7$ does order magnetically. It was suggested that lattice distortions caused by the anisotropic pressure induce the magnetic order.

1.5   Summary

Under the constraints of the classical Heisenberg model with nearest neighbor antiferromagentic couplings, Eq. 1.3 raises the $T = 0$ K ground state condition of $\sum_{i=1}^{q} \mathbf{S}_i = 0$. In frustrated magnets this condition does not uniquely defines the ground state, thus there is an extensive ground state degeneracy.

The presence of a macroscopically degenerate ground state on the classical pyrochlore results in the absence of ordering down to $T = 0$ K. However, all pyrochlores (here we report on Y$_2$Mo$_2$O$_7$, §3.2.1) but one (Tb$_2$Ti$_2$O$_7$ §3.2.2) freeze.

On the kagomé lattice, the situation is reversed. Theoretically, the quantum kagomé $\sqrt{3} \times \sqrt{3}$ state is expected at $T = 0$ K whereas the classical kagomé is predicted to freeze at a finite T. However, the experimental picture is reversed, the only quantum kagomé realized (Herbertsmithite §3.1.1) does not freeze.

1.6 Objectives

The frustrated system is very sensitive to additional terms in the Hamiltonian, we've presented the bi-quadric magneto-elastic coupling which result in lattice distortion, the bi-linear Dzyaloshinksy-Moriya and the linear exchange anisotropy. The most general hamiltonian we consider is,

$$\mathcal{H} = - \sum_{<i,j>} \left(J_z S_i^z S_j^z + J_\perp S_i^\perp S_j^\perp \right) + \sum_{<i,j>} \mathbf{D}_{ij} \cdot (S_i \times S_j) - \frac{1}{3k} \left(\frac{dJ}{dr} \right)^2 \sum_{i>j} (\mathbf{S}_i \cdot \mathbf{S}_j)^2 \ .$$

(1.18)

The aim in this thesis is find such perturbation in various compounds, and investigate their impact of the ground state properties. Using our experimental methods, which we describe in the next chapter, we can probe for exchange anisotropy and magnetoelastic terms. We are unable to detect DMI without heavily relying on theory, since it has no effect at the mean field level (see Eq.1.7).

Chapter 2

Experimental Techniques

In this chapter we describe the various techniques used in the thesis. We begin with an introduction to μSR and elaborate on a Transverse-Field configuration, which was the main tool used in the study of $ZnCu_3(OH)_6Cl_2$ and $Tb_2Ti_2O_7$. We move on to give a description of the NMR technique, discussing the methods for powder-averaging the signal of a powder. This was the main tool in the study of $Y_2Mo_2O_7$. We then turn to describe a SQUID, which complemented all of our studies. We finish with a description of X-ray diffraction which were carried out in the study of $Y_2Mo_2O_7$.

2.1 μSR

μSR is acronym for muon spin rotation/relaxation. The basic idea behind the technique is to measure the time evolution of a muon in a sample, which in turn will tell us about the magnetism of the sample. The positive muon particle (μ^+) is a lepton, the heavy analogue of the positron. The muons are produced through the decay:

$$\pi^+ \rightarrow \mu^+ + \nu_\mu.$$

Thus in order to conserve the total spin 0 of the pion, and since there are only left handed neutrinos (spin is antiparallel to the momenta), the muons created are 100% spin-polarized. The muon is unstable and decays via the weak interaction with an average lifetime of $\tau_\mu \simeq 2.19703$ μsec into a positron and two neutrinos:

$$\mu^+ \rightarrow e^+ + \nu_e + \overline{\nu}_\mu.$$

Because of the parity violation of the weak interaction, the positron from the decay is emitted preferentially in the direction of the spin of the muon at the instant of the decay. By 'preferentially' that is the positron is emitted asymmetrically relative to the muon spin direction, and the angular distribution of the decay positrons depends on their energy. The angular distribution is expressed as

$$dN = \frac{1 + a(\epsilon)cos\theta}{4\pi}\rho(\epsilon)d\cos(\theta)d\epsilon$$

where $a(\epsilon) = (2\epsilon - 1)/(3 - 2\epsilon)$, $\rho(\epsilon) = 2(3 - 2\epsilon)\epsilon^2$ and $\epsilon = E/E_{max}$ is the normalized positron energy, $E = E_{max}$ when both neutrino are emitted in the same direction, $E = 0$ when they are opposite to each other ($E_{max} = m_\mu c^2/2 = 52.8$ MeV). θ is the angle of the positron emission measured from the muon spin direction. After integrating over the energy ϵ the angular distribution obtained is plotted in Fig.2.1 . The radial distance represents the relative probability that a positron is emitted in a given direction.

In conventional magnetic resonance experiments, spin polarization is achieved by a combination of High-Field and low-Temperature. In μSR the muon produced is 100% spin polarized due to the parity-violation decay of the pion. In the rest-frame of the pion, the muon and neutrino are emitted 'back-to-back', and since the neutrino has chirality -1, the muon will also have chirality of -1. The production of the muon beam in a muon facility is basically the following,
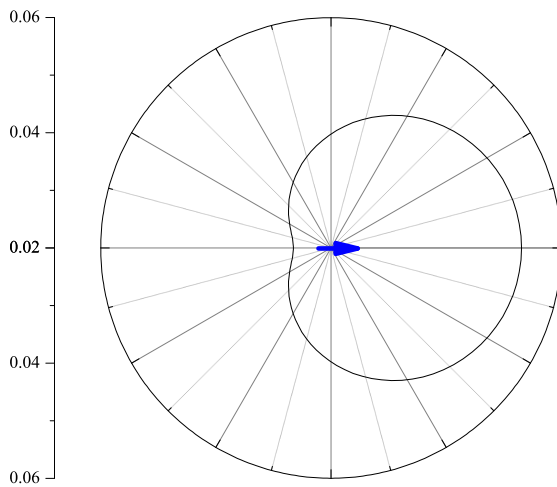
Figure 2.1: The angular distribution of the muon. The radial distance represents the relative probability that a positron is emitted in a given direction.

- A beam of protons is accelerated and aimed at a target such as beryllium or carbon.

- Nuclear reactions occur in target which produce π^+. Some remain in the target, other have some kinetic energy and are emitted.

- The pions decay, the muons have a distribution of momenta. High momentum muons from energetic pions decaying in flight, the low momentum muons from pions within the target.

- A separator is used to filter only muons with a specific momentum which correspond to muons from pions which decay at rest near the surface of the target. These are *surface muons* with a well-defined kinetic energy of 4.1 MeV.

- The beam of the *surface muons* is then focused on the material studied. The

4.1 MeV kinetic energy of the muon can be converted to a mean stopping range of 140 mg/cm².

The decay positrons are detected in one of the scintillator detectors which surround the sample environment. Each detector creates an histogram of the time differences between the muon implantation and decay positron. The number of detected positrons in a histogram of detector i correspond to

$$N_i(t) = N_{i0}e^{-t/\tau_\mu}[1 + A_i\mathbf{P}_\mu(t)] + B_i$$

where N_{i0} is a normalization, B_i is time-independent background, A_i is the experimental asymmetry (typically 0.24), $\mathbf{P}_i$ is the muon polarization function in the direction sample→detector.

The cyclotron based facility in PSI provide us with a continuous muon beam. As a result, a muon counter on the beam path right before the sample is required to record the muon arrival time. The timing resolution is limited by electronics to be of the order of $nsec$ (0.625 nsec in LTF and 1.25 nsec in GPS) and the time window is about 6 to 10sec.

The time differential measurements fall into three categories depending on the direction of the field applied relative to the direction of the muon initial polarization: Longitudinal (LF), transverse (TF) and zero (ZF). The basic idea is to investigate the nature of the changes in the local environment of the muon as the temperature decreases. We determine whether only the spin polarization is changing or whether the lattice is involved as well. Electronic spin polarization contributes to the shift of the muon spin rotation frequency. Lattice distortions are responsible for muon spin polarization relaxation.

ZF μSR is a sensitive site-based probe of static magnetism, in which the muon polarization $\mathbf{P}_\mu$ is determined by the small internal magnetic fields in the sample itself. In a LF configuration, the relaxation (R_{LF}) in $\mathbf{P}_\mu$ is usually exponential and stems from dynamic fluctuating fields within the sample. In a TF configuration, the relaxation (R_{TF}) is a bit more involved. It is a result of both static field inhomogeneities on the time scale of one muon spin turn, and dynamically fluctuating fields. In the next section we deal with the physical parameters we extract in a TF experiment.

2.1.1 Transverse Field Configuration

A schematic diagram of a typical setup of a transverse field configuration is shown in Fig. 2.2 . In a TF geometry, the initial polarization, $\mathbf{P}_\mu(0)$, is perpendicular to $\mathbf{H}$. Thus, $\mathbf{P}_\mu(t)$ exhibits oscillations at the Larmor frequency, $\omega_\mu = \gamma_\mu H$ ($\gamma_\mu = 13.554$ MHz/kG). The TF relaxation (R_{TF}) is a result of both static field inhomogeneities and dynamically fluctuating fields. TF experiment is usually refer to as analogous to a free induction decay in NMR with R_{TF} identified as $(T_2^*)^{-1}$.

As a starting point, we assume a static local field distribution that has an isotropic Gaussian distribution. Thus the muon polarization is exponential gaussian relaxation combined with oscillations at the muon Larmor frequency,

$$P_\mu(t) = P_0 \exp(\frac{-t}{T_2^*}) \cos(\omega t). \tag{2.1}$$

To investigate the relation between the R_{TF} and the susceptibility we look at the muon hamiltonian,

$$H = \hbar \gamma_\mu \mathbf{I} \cdot \mathbf{B} \tag{2.2}$$

where $\mathbf{I}$ is the muon spin and $\mathbf{B}$ is the field the muon experiences, which is the
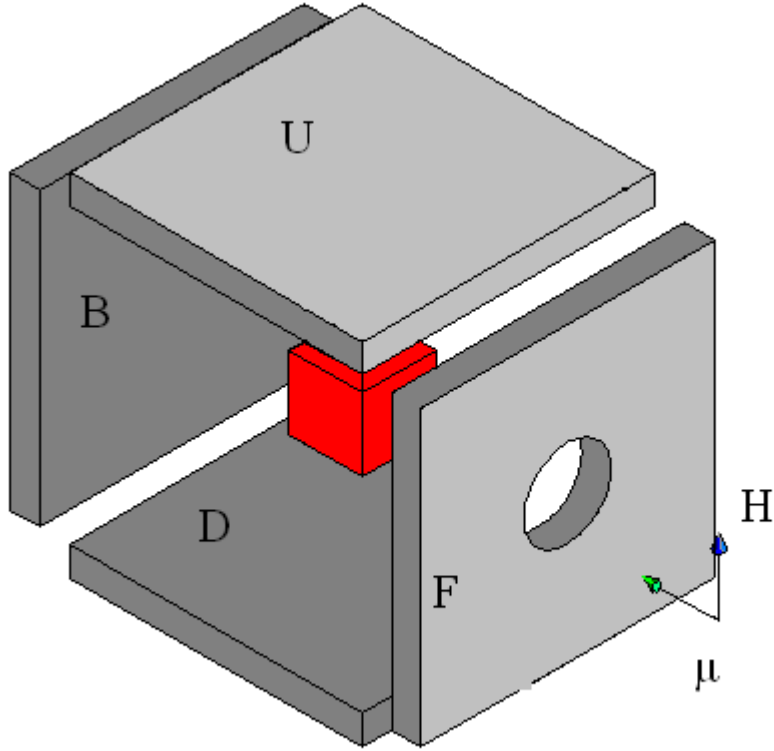
Figure 2.2: A typical TF μSR configuration. The red box indicates the sample.

contribution of the external and internal fields,

$$\mathbf{B} = \mathbf{H}_{TF} + \mathbf{H}_{int} \tag{2.3}$$

$\mathbf{H}_{TF}$ is the applied transverse field and $\mathbf{H}_{int}$ is the magnetic field from neighboring electrons. The internal fields the muon experiences is created by the coupling between the muon and electronic spin,

$$\mathbf{H}_{int} = g\mu_B \sum_j \mathbf{A}_j \cdot \mathbf{S}_j$$

where the sum j runs over the muon's neighboring electrons, $\mathbf{A} = A(r)$ is the coupling

between the muon and the electronic spin and $\mathbf{S}$ is the electronic spin. For simplicity we assume the coupling to only one electronic spin thus $\sum_j A_j \mathbf{S}_j \rightarrow A\mathbf{S}$. By a mean field approximation, we replace $\mathbf{S}$ by its expectation value $\langle \mathbf{S} \rangle = \mathbf{M} = \chi \mathbf{H}$. Thus, the muon experiences a field given by,

$$\mathbf{B} = (1 + A\chi)\mathbf{H}_{TF} \tag{2.4}$$

assuming isotropic couplings A and χ then the muon polarization,

$$P_\mu(t) = P_0 \cos[\gamma_\mu(1 + A\chi)\mathbf{H}_{TF}t] \tag{2.5}$$

by averaging over a distribution of couplings ($\rho(A)$),

$$\overline{P}_\mu(t) = \int P_0 \cos[\gamma_\mu(1 + (\overline{A} + \delta A)\chi)\mathbf{H}_{TF}t]\rho(A)dA \tag{2.6}$$

thus, if the experimental polarization is Eq. 2.1 we can equalize the two equations and extract $\rho(A)$,

$$\rho(A) = \frac{1}{\delta A\sqrt{2\pi}} \exp(-\frac{1}{2}(\frac{\overline{A} + \delta A}{\delta A})^2)$$

where the width of the gaussian,

$$\delta A = |\frac{1}{\chi T_2^* \gamma_\mu H}| \tag{2.7}$$

thus,

$$\frac{1}{T_2^*} = \delta A \gamma_\mu H \cdot \chi \ . \tag{2.8}$$

Therefore, according to Eq.2.7 if the ratio between $(T_2^*)^{-1}$ and χ remains constant as T decreases, one can conclude that δA is T independent and no lattice deformation occur.

In this calculations we assumed that the Longitudinal Field Relaxation, R_{LF}, thus the dynamically fluctuating fields are orders of magnitude smaller than the Transverse

Field Relaxation, $R_{TF} = (T_2^*)^{-1}$, i.e., the static field inhomogeneities. In such case that this assumption is not correct, one has to observe the difference between the relaxation given by the static relaxation rate, $\Delta = \sqrt{R_{TF}^2 - R_{LF}^2}$, this is described in Ref.[46].

2.2   NMR

Nuclear Magnetic Resonance (NMR) was first described by Purcell and Bloch during mid 1940s, they then received the Nobel prize in physics in 1952: "for their development of new methods for nuclear magnetic precision measurements and discoveries in connection therewith". NMR is possible since nuclei of many atoms possess magnetic moments and angular momenta. The magnetic moment (spin) of the nuclei interacts with a static magnetic field $(H = H_0\hat{z})$ in such a way that the field polarizes the nuclear moment (spin) along its direction $(\hat{z})$. The result is that the nuclei (spin) precess about the field. The precession frequency of the moment (spin) is proportional and uniquely determined by the gyromagnetic ratio γ and the strength of the magnetic field H_0,

$$\omega_0 = \gamma H_0 .$$

ω_0 is the Larmor velocity (the larmor frequency is, $\nu_0 = \omega_0/(2\pi)$). The gyromagnetic ratio differs from one nuclei to the other (also, from one isotope to the other) thus the angular momentum (spin) of each nuclei is defined uniquely by $\mu = \gamma I \hbar$.

The NMR phenomena can be described by classical and quantum derivation. In a quantum mechanics treatment, the orientation of a spin in a field is quantized. The number of allowed orientations is $2I + 1$, where I is the nuclear spin quantum number.

The energy of each orientation is described by the schrodinger equation,

$$H|m_I\rangle = E|m_I\rangle$$

$$E = -\hbar\gamma B_z m_I \tag{2.9}$$

therefore a transition between the energy levels, will occur when $\Delta E = \hbar\gamma B_z \Delta m_I$. This transition can be induced by absorption or emission of a photon of frequency ν_0 such that,

$$\Delta E = \hbar\gamma B_z \Delta m_I = h\nu_0. \tag{2.10}$$

This energy transfer occurs when another field H_1 is applied in the $\hat{x} - \hat{y}$ plane. The evolution of the spin under the combined magnetic fields is described by the hamiltonian,

$$i\hbar\frac{\partial}{\partial t}|n\rangle = -\gamma\hbar\mathbf{H} \cdot \mathbf{I}|n\rangle$$

$$= -\gamma\hbar[H_1\left(I_x \cos(\omega t) + I_y \sin(\omega t)\right) + H_0 I_z]|n\rangle \tag{2.11}$$

Since $\hat{R}_z(\beta)\hat{I}_x\hat{R}_z(-\beta) = I_x \cos\beta + I_y \sin\beta$ (where $\hat{R}_j(\beta) = \exp(-i\beta I_j)$ is the rotation operator) this can be further developed to

$$i\hbar\partial_t|n\rangle = -\gamma\hbar\left[H_0 I_z + H_1 e^{-i\omega I_z t}I_x e^{i\omega I_z t}\right]|n\rangle$$

$$= \left[\hat{\mathcal{H}}_Z + \hat{\mathcal{H}}_{rf}\right]|n\rangle . \tag{2.12}$$

Using a rotating reference frame of the spin ($|\tilde{n}\rangle = \hat{R}_z(-\omega t)|n\rangle = \exp(i\omega I_z t)|n\rangle$) will simplify the hamiltonian giving,

$$i\hbar\partial_t|\tilde{n}\rangle = (-\hbar\omega I_z e^{i\omega I_z t} + i\hbar e^{i\omega I_z t}\partial_t)|n\rangle$$

$$= -\hbar\omega I_z e^{i\omega I_z t}|n\rangle + e^{i\omega I_z t}(H_Z + H_{rf})|n\rangle$$

$$= (-\hbar\omega I_z e^{i\omega I_z t} + e^{i\omega I_z t}(\mathcal{H}_Z + \mathcal{H}_{rf}))e^{-i\omega I_z t}|\tilde{n}\rangle \tag{2.13}$$

$$= \tilde{\mathcal{H}}|\tilde{n}\rangle$$

where,

$$\tilde{\mathcal{H}} = e^{i\omega I_z t}(\mathcal{H}_Z + \mathcal{H}_{rf})e^{-i\omega I_z t} - \hbar\omega \ . \tag{2.14}$$

Lets examine a case where H_Z is the only term in $\tilde{\mathcal{H}}$, in that case,

$$\begin{aligned}
\tilde{\mathcal{H}} &= e^{i\omega I_z t}\mathcal{H}_Z e^{-i\omega I_z t} - \hbar\omega I_z \\
&= e^{i\omega I_z t}(-\gamma\hbar H_0 I_z)e^{-i\omega I_z t} - \hbar\omega I_z \\
&= -\gamma\hbar H_0 I_z - \hbar\omega I_z
\end{aligned} \tag{2.15}$$

since rotation along the same axis has no effect. Thus,

$$\begin{aligned}
\tilde{\mathcal{H}} &= -\gamma\hbar H_0 I_z - \hbar\omega I_z \\
&= -(\omega_0 + \omega)\hbar I_z \\
&= \Omega_0 \hbar I_z
\end{aligned} \tag{2.16}$$

In the case with H_{rf},

$$\begin{aligned}
\tilde{\mathcal{H}} &= \Omega_0 \hbar I_z - \gamma\hbar e^{i\omega I_z t}\mathcal{H}_{rf}e^{-i\omega I_z t} \\
&= \Omega_0 \hbar I_z - \gamma\hbar e^{i\omega I_z t}H_1 e^{-i\omega I_z t}I_x e^{i\omega I_z t}e^{-i\omega I_z t} \\
&= \Omega_0 \hbar I_z - \gamma\hbar H_1 I_x \ .
\end{aligned} \tag{2.17}$$

Pulses

The time dependent solution to Eq.2.14,

$$|\tilde{t}\rangle = e^{\frac{i\tilde{\mathcal{H}}t}{\hbar}}|\tilde{n}\rangle \tag{2.18}$$

in the resonance case, where $\omega_0 + \omega = 0 \Rightarrow \Omega = 0$, the expectation value for I will therefore,

$$\langle I_z(t) \rangle \quad = \quad \sum_{\tilde{n}} p_{\tilde{n}} \langle \tilde{n} | e^{-i\gamma H_1 I_x t} I_z e^{i\gamma H_1 I_x t} | \tilde{n} \rangle \tag{2.19}$$

$$= \quad \sum_{\tilde{n}} p_{\tilde{n}} \langle \tilde{n} | I_z | \tilde{n} \rangle \cos(\gamma H_1 t) - p_{\tilde{n}} \langle \tilde{n} | I_y | \tilde{n} \rangle \sin(\gamma H_1 t) \tag{2.20}$$

$$= \quad \langle I_z(0) \rangle \cos(\gamma H_1 t) - \langle I_y(0) \rangle \sin(\gamma H_1 t) \tag{2.21}$$

as a consequence, for I_y the result will be,

$$\langle I_y(t) \rangle \quad = \quad \sum_{\tilde{n}} p_{\tilde{n}} \langle \tilde{n} | e^{-i\gamma H_1 I_x t} I_y e^{i\gamma H_1 I_x t} | \tilde{n} \rangle \tag{2.22}$$

$$= \quad \langle I_z(0) \rangle \sin(\gamma H_1 t) + \langle I_y(0) \rangle \cos(\gamma H_1 t) \tag{2.23}$$

and for I_x,

$$\langle I_x(t) \rangle \quad = \quad \sum_{\tilde{n}} p_{\tilde{n}} \langle \tilde{n} | e^{-i\gamma H_1 I_x t} I_x e^{i\gamma H_1 I_x t} | \tilde{n} \rangle \tag{2.24}$$

$$= \quad \sum_{\tilde{n}} p_{\tilde{n}} \langle \tilde{n} | I_x | \tilde{n} \rangle = \langle I_x(0) \rangle \tag{2.25}$$

$\pi/2$ pulse

The initial conditions dictate the polarization of I, that is all spins are polarized to the direction of $H_0 \hat{z}$,

$$\langle I_z(0) \rangle \quad = \quad \mathrm{Tr} \frac{\exp(-\tilde{\mathcal{H}}/kT)}{Z} I_z \tag{2.26}$$

$$\simeq \quad Z^{-1} \mathrm{Tr} I_z + Z^{-1} \mathrm{Tr} \frac{\gamma \hbar H_0}{kT} I_z^2 \tag{2.27}$$

$$\simeq \quad \frac{1}{2I+1} \frac{\gamma \hbar H_0}{kT} \frac{I(I+1)(2I+1)}{3} \tag{2.28}$$

$$\simeq \quad \frac{\gamma \hbar H_0 I(I+1)}{3kT} \tag{2.29}$$

and for I_x and I_y,

$$\langle I_x(0) \rangle = \langle I_y(0) \rangle = 0 \tag{2.30}$$

thus, when $\gamma H_1 \tau = \pi/2$,

$$\langle I_z(\tau) \rangle = \langle I_x(\tau) \rangle = 0 \tag{2.31}$$

$$\langle I_y(\tau) \rangle = I_z(0). \tag{2.32}$$

When we have electrons producing internal fields in the sample, B, the nuclear spins will experience a distribution of fields thus they will precess at slightly different frequencies.

Spin Echo

The spin echo $(\pi/2 - \tau - \pi)$ sequence is a two-step procedure, the first step, applying a $\pi/2$ pulse. The $\pi/2$ pulse rotates the nuclear magnetization 90° to the $x - y$ plane. The second step takes place after time τ, during which the spin dephase. The second step is applying a π pulse. The π pulse rotates the magnetization 180°. In the top of Fig. 2.3 we plot the spin-echo sequence. At $t = 0 \ldots t_1$, RF is applied producing the $\pi/2$ pulse ($\omega t_1 = \pi/2$). During $\tau = t_1 \ldots t_2$ the spins precess freely. The second pulse is applied at $t_2 \ldots t_3$ such that it produces the π pulse. In the rotating reference frame of the nuclei,

$$
\begin{aligned}
i\hbar \partial_t \psi &= \tilde{\mathcal{H}} \psi \\
&= -\gamma \hbar \left(\left(H_0 - \frac{\omega}{\gamma} \right) I_z + H_1 I_x \right) .
\end{aligned}
\tag{2.33}
$$

During the pulses, $H_1 \gg (H_0 - \omega/\gamma)$, thus we can write the hamiltonian as time dependent as

$$
\tilde{\mathcal{H}}(t) =
\begin{array}{ll}
-\gamma \hbar H_1 I_x & 0 < t < t_1; t_2 < t < t_3 \\
-\gamma \hbar \left(H_0 - \frac{\omega}{\gamma} \right) & t_1 < t < t_2
\end{array}
\tag{2.34}
$$

Although $\tilde{\mathcal{H}}$ is time dependent, in each step it is independent of time so we can use $\psi = \exp\left(-(i/\hbar)\tilde{\mathcal{H}}t\right)\psi$ to solve for ψ. The solution comes about to be,

$$\psi(t_1) = e^{i\gamma H_1 t_1 I_x}\psi(0) \tag{2.35}$$

where during $0 < t < t_1$ we apply the $\pi/2$ pulse i.e., $\gamma H_1 t_1 = \pi/2$. The progressive solutions are therefore,

$$\begin{aligned}
\psi(t_2) &= e^{i(\gamma H_0 - \omega)(t_2 - t_1)I_z}\psi(t_1) \\
\psi(t_3) &= e^{i\gamma H_1(t_3 - t_2)I_x}\psi(t_2) = e^{i\pi I_x}\psi(t_2) \\
\psi(t > t_3) &= e^{i(\gamma H_0 - \omega)(t - t_3)I_z}\psi(t_3)
\end{aligned} \tag{2.36}$$

where at $t_2 < t < t_3$ we apply the π pulse. We now define,

$$\begin{aligned}
T(t) &= e^{i(\gamma H_0 - \omega)t I_z} \\
X(\theta) &= e^{i\theta I_x}
\end{aligned} \tag{2.37}$$

$T(t)$ is the development of ψ during $H_1 = 0$, $X(\theta)$ is the operator rotating the spins by an angle θ, thus for example,

$$\begin{aligned}
X^{-1}(\pi/2)I_y X(\pi/2) &= I_z \\
X^{-1}(\pi)I_y X(\pi) &= -I_y \,.
\end{aligned} \tag{2.38}$$

Now $\psi(t)$ after the second (π) pulse, can be represented as,

$$\psi(t) = T(t - \tau)X(\pi)T(\tau)X(\pi/2)\psi(0) \,. \tag{2.39}$$

Using $X^{-1}(\theta)X(\theta) = X(\theta)X^{-1}(\theta) = 1$ and $X^{-1}T^{-1}X = T$ and $T(\tau)T^{-1}(\tau) = 1$ we can calculate the expectation value for I_x at $t = 2\tau$,

$$
\begin{aligned}
\langle I_x \rangle &= \langle \tilde{n}|X^{-1}(\pi/2)T^{-1}(\tau)X^{-1}(\pi)T^{-1}(\tau)I_xT(\tau)X(\pi)T(\tau)X(\pi/2)|\tilde{n}\rangle \\
&= \langle \tilde{n}|X^{-1}(\pi/2)T^{-1}(\tau)X^{-1}(\pi)T^{-1}(\tau)X(\pi)X^{-1}(\pi)I_xX(\pi)X^{-1}(\pi)T(\tau)X(\pi)T(\tau)X(\pi/2)|\tilde{n}\rangle \\
&= \langle \tilde{n}|X^{-1}(\pi/2)T^{-1}(\tau)X^{-1}(\pi)T^{-1}(\tau)X(\pi)I_xX^{-1}(\pi)T(\tau)X(\pi)T(\tau)X(\pi/2)|\tilde{n}\rangle \\
&= \langle \tilde{n}|X^{-1}(\pi/2)T^{-1}(\tau)T(\tau)I_xT^{-1}(\tau)T(\tau)X(\pi/2)|\tilde{n}\rangle \\
&= \langle \tilde{n}|X^{-1}(\pi/2)I_xX(\pi/2)|\tilde{n}\rangle = \langle \tilde{n}|I_x|\tilde{n}\rangle \\
&= 0 \tag{2.40}
\end{aligned}
$$

since at $t = 0$ the magnetization is completely polarized to $\hat{z}$. We apply the same technique for the calculation of I_y,

$$
\begin{aligned}
\langle I_y \rangle &= \langle \tilde{n}|X^{-1}(\pi/2)T^{-1}(\tau)X^{-1}(\pi)T^{-1}(\tau)I_yT(\tau)X(\pi)T(\tau)X(\pi/2)|\tilde{n}\rangle \\
&= \ldots = X^{-1}(\pi/2)I_yX(\pi/2)|\tilde{n}\rangle = \langle \tilde{n}|I_z|\tilde{n}\rangle
\end{aligned}
$$

thus, the echo we receive at $t = 2\tau$ has the same magnitude of the net magnetization just before the sequence began.

Saturation Recovery and T_1 measurement

At equilibrium, all spins are polarized with the external field, H_0. In order to change the direction of the spins a transverse field H_1 is applied. The time constant which describes how the the spins return to equilibrium is called the spin-lattice relaxation, T_1. T_1 measures the density of excitation in the frequency γH (Eq. 1.16).

The saturation recovery sequence is a technique to measure T_1. The beginning of the sequence is a series of $\pi/2$ pulses at short repetition times ($\sim T_2$), and then a regular spin echo sequence is applied after a delay τ. The multiple $\pi/2$ pulses destroys
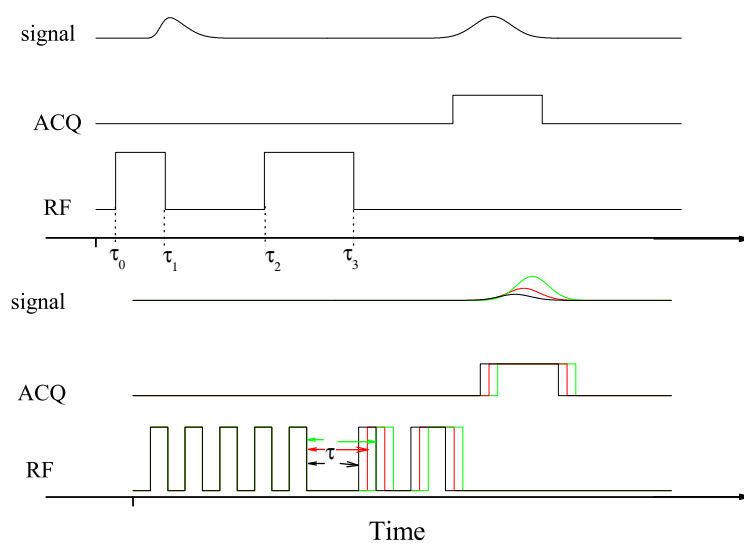
Figure 2.3: Echo sequences, top: the spin-echo sequence, bottom: a saturation recovery sequence, each color represents a different delay time, τ, between the π pulses and the spin-echo sequence.

the magnetization at t right after the pulses. The sequence is executed with different τ's. When $\tau \to 0$ the echo intensity $\to 0$, when $\tau \to \sim 5T_1$ the echo intensity reaches its almost maximal value ($\sim 99.3\%$). Thus at short (long) τ the echo magnitude should be small (approximately the same) compared to its maximum value. The bottom of Fig. 2.3 displays the saturation recovery sequence.

Powder Average

Generally, the greatest amount of information concerning nuclear or paramagnetic sites in solids can be obtained from measurements in single crystals. However, many compounds lack single crystals. In other cases, the difficulty or expense in obtaining a single crystal may not be justified by the nature of the information desired. Thus, the analysis of the powder spectra is essential in order to extract the relevant information. In Appendix A we derive the powder spectrum, here we show an outline for a completely anisotropic sample.

The NMR hamiltonian can be represented as,

$$\mathcal{H} = -\hbar\gamma\mathbf{I} \cdot (1 - \sigma) \cdot \mathbf{H} \tag{2.41}$$

where σ is a magnetic shift tensor, any may represent a chemical shift (in the case of diamagnetic compounds) or a paramagnetic shift (in the case of a strongly paramagnetic compound) or a Knight Shift tensor (in the case of metallic compounds). In any case, all magnetic shifts have the same functionality, so for convenience we concern a Knight shift tensor ($\mathbf{K} = -\sigma$).

In a single crystal, the resonance frequency depends on the orientation of the single crystal with respect to the applied magnetic field. In a polycrystalline, the nuclear spins are randomly oriented with respect to the field, thus the powder pattern is an

average over the resonance condition for all possible orientations of the nuclear site.

The powder average, S(H), represents the amplitude of the magnetic resonance signal at field H comes to be,

$$S(H) = \int \frac{d\varphi}{2H^2} \frac{H_1 H_2 H_3}{\sqrt{(H^2 - H_1^2)}\sqrt{(H_3^2 - H_2^2)}}$$
$$\cdot \frac{1}{\sqrt{1 - \frac{(H_2^2 - H_1^2)H^2}{H_2^2(H^2 - H_1^2)}\sin^2\varphi}\sqrt{1 - \frac{(H_2^2 - H_1^2)H_3^2}{H_1^2(H_3^2 - H_2^2)}\sin^2\varphi}} \quad (2.42)$$

where H_i are the locations in the magnetic field of ordinary singularities and is defined by the principal values of electronic g tensor, $H_i(\nu) = h\nu/(g\hbar\gamma)$. φ is an Euler angle of external magnetic field, H, relative to the principal axis of **K**. Eq. 2.42 has the form of an elliptic integral, $K(k) = \int_0^{\pi/2}(1 - k^2 sin^2\theta)^{-1/2}d\theta = \int_0^1(1 - k^2 t^2)^{-1/2}(1 - t^2)^{-1/2}dt$. Thus in order to simulate the powder pattern we use the elliptic integral polynomial approximation[47],

$$K(m) = [a_0 + a_1 m_1 + \ldots + a_4 m_1^4] + [b_0 + b_1 m_1 + \ldots + b_4 m_1^4]ln(1/m_1) \quad (2.43)$$

where the coefficients a_i and b_i are given in table 2.1 . Where $m = k^2$ and m_1 are the elliptic integral parameter and its complementary parameter respectively, $m + m_1 = 1$,

$$m = \frac{H_2^2 - H_1^2}{H_3^2 - H_2^2} \cdot \frac{H_3^2 - H^2}{H^2 - H_1^2} \quad (2.44)$$

In Fig. 2.4 we present a theoretical powder spectrum for a single site. This demonstrates that a single site contributes one NMR peak under powder averaging.

i	0	1	2	3	4
a	1.38629	0.09666	0.0359	0.03742	0.01451
b	0.5	0.12498	0.0688	0.03328	0.00441

Table 2.1: The polynomial coefficients of Eq.2.43 .
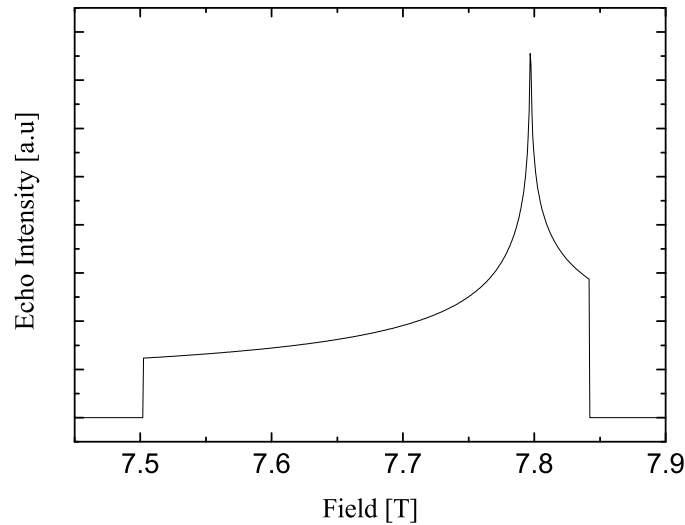
Figure 2.4: A theoretical powder-averaged NMR for a spin-1/2, $\gamma = 2.11\text{MHz/T}$, $\nu = 16.44\text{MHz}$.

2.3   Squid

The SQUID is an acronym for Superconducting Quantum Interference Device. It is one of the most sensitive form of magnetometry. SQUIDs function as a magnetic flux-to-voltage transducers. The physical idea behind the squid are the properties of electron-pair ('cooper pairs') wave coherence and Josephson junctions thus being able to detect very small fields (a squid can measure 1 flux quantum where the earth magnetic field passing through the area of a typical squid correspond to ~ 100 flux quanta).

Cooper pairs are pairs of electrons which carry the resistanceless current in su-perconductors. Each pair can be considered as a single particle with double mass and double charge of a single electron, the velocity of the pair is of the center

of mass of the pair. Each pair can be represented by a wavefunction of the form $\Phi_P = \Phi \exp\left(i(\mathbf{P} \cdot \mathbf{r})/\hbar\right)$, where $\mathbf{P}$ is the momentum of the pair whose center of mass is at $\mathbf{r}$. In a uniform current density all electron wavelengths will be equal and with the superposition of these coherent waves making up the single many-body wavefunction

$$\Psi_P = \Psi \exp\left(i(\mathbf{P} \cdot \mathbf{r})/\hbar\right) \ . \tag{2.45}$$

In a closed superconducting ring, due to the long coherence of the superconducting wavefunction (Eq. 2.45), the phase difference between one point X and another point Y is constant in time,

$$(\delta\phi)_{XY} = \phi_X - \phi_Y = 2\pi \int_X^Y \frac{\mathbf{P}}{h}\hat{\mathbf{r}} \cdot d\mathbf{l} \tag{2.46}$$

where $\hat{\mathbf{r}}$ is a unit vector in the direction of the wave propagation and $d\mathbf{l}$ is an element along the path $X - Y$. In the special case of $X = Y$, $\delta\phi_{XY} = 2\pi$. Using the supercurrent density (which is an analogue to the current density $\vec{j} = nq\vec{v_d}$),

$$j_s = \frac{1}{2}n_s \cdot e \cdot v \tag{2.47}$$

where n_s is the super fluid density thus $1/2n_s$ is the cooper pair density, (thus, $v = 2j_s/(n_s e)$) and we can write Eq. 2.46 as,

$$\delta\phi_{XY} = \frac{2m}{e\hbar n_s} \int_X^Y j_s d\mathbf{l} \ . \tag{2.48}$$

Under applied field the momentum P of the cooper pair must be revised to $\mathbf{P} = 2m\mathbf{v} + 2e\mathbf{A}$ where $\mathbf{A}$ is the magnetic vector potential. The difference in the phase is now written,

$$\delta\phi_{XY} = (\delta\phi_{XY})_j + (\delta\phi_{XY})_B \tag{2.49}$$

where the first term is the contribution from the supercurrent,

$$(\delta\phi_{XY})_j = \frac{2m}{e\hbar n_s} \int_X^Y j_s d\mathbf{l} \tag{2.50}$$

and the second due to the applied field,

$$(\delta\phi_{XY})_B = \frac{2e}{\hbar} \int_X^Y \mathbf{A} d\mathbf{l} \ . \tag{2.51}$$

In a closed encircling path (the path can encircle a non superconducting region), the phase difference can be written as,

$$\delta\phi = \frac{2m}{e\hbar n_s} \oint j_s d\mathbf{l} + \frac{2e}{\hbar} \oint \mathbf{A} d\mathbf{l} \ . \tag{2.52}$$

since $\oint_{\partial\Sigma} \mathbf{F} \cdot d\mathbf{r} = \int_\Sigma \nabla \times \mathbf{F} \cdot d\mathbf{\Sigma}$ (stokes theorem) and $\mathbf{B} = \nabla \times \mathbf{A}$,

$$\delta\phi = \frac{2m}{e\hbar n_s} \oint j_s d\mathbf{l} + \frac{2e}{\hbar} \int_S \mathbf{B} d\mathbf{S} \tag{2.53}$$

where S is the enclosed area. Due to the long coherence of the superconducting wavefunction, the difference in phase of a closed loop (a ring) must equal $2\pi n$ where n is an integer. Thus, we arrive at,

$$\delta\phi = \frac{m}{e^2 n_s} \oint j_s d\mathbf{l} + \int_S \mathbf{B} d\mathbf{S} = n\frac{h}{2e} \tag{2.54}$$

i.e., due to the long coherence, in a closed rings, the flux can only exist in quantized form, where the *flux quantum* value is,

$$\Phi_0 = \frac{h}{2e} \ = \ 2.07 \times 10^{-15} \text{Wb} \tag{2.55}$$

$$= \ 2.07 \times 10^{-7} \text{G-cm}^2 \ . \tag{2.56}$$

The second important physical phenomena needed for a squid to work is *Josephson Tunneling*. When two superconductors are isolated one from another, the phases in each of the superconductors may differ. However, when the two are brought closer together, tunneling may occur and thereby the two superconductor interact. The tunneling of an electron-pair creates a superconducting current. Thus, the supercurrent, i, which flows across a gap between two superconductors which have a phase

difference $\delta\varphi$, is given by,

$$i = i_c \sin \delta\varphi \qquad (2.57)$$

where i_c is the critical current. Hence, the maximum current which can flow across a gap occurs when $\varphi = \pi/2$, giving a current $i = i_c$. The gap can be created by any weak coupling between two parts of a single superconductor - this maybe microscopic point contacts, crystallographic grain boundaries or any weakly conducting layers.

As mentioned previously, the SQUID (specifically the dc-SQUID) is based on the long coherence of the superconducting wavefunction, i.e., on the flux quantum, and on the Josephson effect. The dc-SQUID is a superconducting loop with two Josephson junctions. When a magnetic field is applied perpendicular to the plane of the ring, a screening current, i_s is induced. Normally, i_s can be sufficient to cancel out the field in the ring, but the critical current at the junctions might prohibits this. The magnetic field thus produces a phase difference,

$$\delta\phi_B = 2\pi\frac{\Phi_a}{\Phi_0} \qquad (2.58)$$

where Φ_a is the flux of the applied field. Φ_a may not necessarily be equal to $2\pi n$ therefore to ensure the total phase change is indeed a multiple of $2\pi n$ a small current i flows so that around the loop across the two junctions, $\delta\phi_B + 2\delta\phi_i = 2\pi n$. Using Eq. 2.57 and Eq. 2.58 the current will be

$$i = i_c \sin \pi \frac{\Phi_a}{\Phi_0} \ . \qquad (2.59)$$

Thus, when Φ_a increases from 0 to $\Phi_0/2$ the current i increases, reaching a maximum at $\Phi_0/2$. When Φ_a continues to increase from $\Phi_0/2$, i changes direction and flows the other way. This current is periodic in the applied flux. The overall phase difference, which must be 2π, is a sum of the phases produced by currents across the junctions

and due to the applied field,

$$\varphi_1 + \varphi_2 + 2\pi \frac{\Phi_a}{\Phi_0} = 2\pi n \ . \tag{2.60}$$

where φ is the phase difference across a junction. When a current flows φ_1 and φ_2 are different, however their sum must be constant (since $2\pi\Phi_a/\Phi_0$ and $2\pi n$ are constants), thus,

$$\varphi_1 + \varphi_2 = 2\pi \left(n - \frac{\Phi_a}{\Phi_0} \right) \tag{2.61}$$

hence it is possible to write,

$$\varphi_1 = \pi \left(n - \frac{\Phi_a}{\Phi_0} \right) - \delta \tag{2.62}$$

$$\varphi_2 = \pi \left(n - \frac{\Phi_a}{\Phi_0} \right) + \delta \tag{2.63}$$

where δ is related to the measuring current I. Using Eq.2.57,

$$
\begin{aligned}
I &= i_c \left[\sin \left(\pi \frac{\Phi_a}{\Phi_0} + \delta \right) + \sin \left(\pi \frac{\Phi_a}{\Phi_0} - \delta \right) \right] \\
&= i_c \left[\sin \left(\pi \frac{\Phi_a}{\Phi_0} \right) \cos \delta + \cos \left(\pi \frac{\Phi_a}{\Phi_0} \right) \sin \delta - \left[\sin \left(\pi \frac{\Phi_a}{\Phi_0} \right) \cos \delta - \cos \left(\pi \frac{\Phi_a}{\Phi_0} \right) \sin \delta \right] \right] \\
&= 2i_c \left[\cos \left(\pi \frac{\Phi_a}{\Phi_0} \right) \sin \delta \right] \ .
\end{aligned}
\tag{2.64}
$$

since $|\sin \delta| \leq 1$ thus the absolute critical measuring current is

$$|I(\Phi_a)| = 2i_c |\cos \left(\pi \frac{\Phi_a}{\Phi_0} \right)| \tag{2.65}$$

we now see that we have a periodic dependance on the magnetic flux (and field), with a maximum when $\Phi_a = \Phi_0 n$, with integer n. Assuming that the Josephson junctions are identical when a bias current, $I_{bias} < i_c$, flows across the loop splits to the two junctions. As long as the current through the junctions is small, there will be no voltage detected across the ring. As I increases it reaches a critical measuring current, at which voltage begins to be detected.
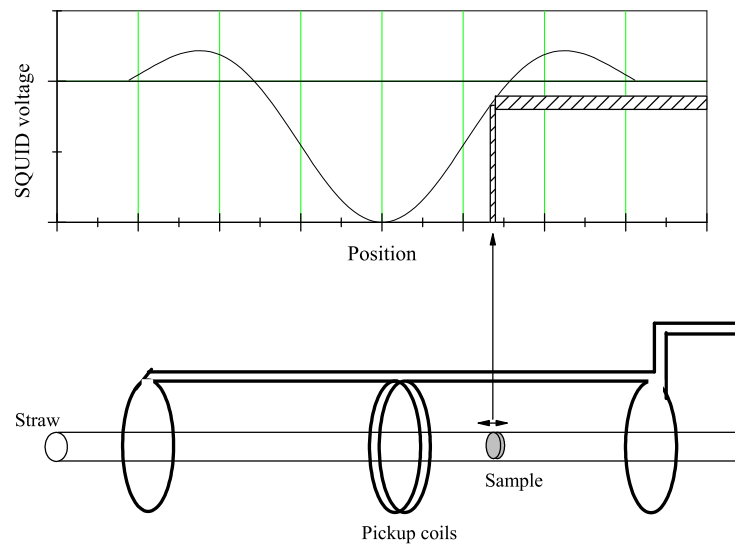
Figure 2.5: A typical paramagnetic SQUID signal. The voltage across the squid as a function of the samples position.

The measurement in the Cryogenic SQUID is performed by moving the sample through the pickup coils. As the sample moves through the coils, the magnetic moments of the sample induces an electric current in the pickup coils thus creating a change in the magnetic flux which is then detected in the SQUID (see Fig. 2.5).

The pickup coils are a set of three coils configured as a second-order gradiometer. In this configuration, the upper coil is a a single turn wound clockwise, the center coil has two turns wound counter-clockwise and the bottom coil is again a single turn wound clockwise. This gradiometer configuration is used to reduce noise in the detection circuit. Over long periods of time currents may build up in the coils thereby producing noise in the system. To prevent this from occurring by heating a small section of the coil circuit.

2.3.1 Experimental Setup

Here we describe the experimental setups which were used in the various experiments conducted in the lab's Cryogenic SQUID magnetometer.

Herbertsmithite and $Y_2Mo_2O_7$

The magnetization measurements were performed in the 'usuall' manner, that is, the measurements performed on powdered samples placed in a gel capsule inside the squid's Helium dewar. A summary of the measurements is given in table 2.2.

Oriented Herbertsmithite

The sample orientation was done by curing $ZnCu_3(OH)_6Cl_2$ powder overnight with Stycast in a field of 8 T. The samples were cured in a Teflon form producing a ball 6 mm in diameter. During the first 40 minutes of the orientation, a shaking mechanism was applied to the sample form. A particularly small amount of powder was used to avoid saturating the Stycast and eliminating powder residues at the bottom of the ball. We prepared a second "test" sample in the same manner, but this time without orientation. In §3.1.2 we refer to the second ball as the powder sample. We also prepared a ball made of Stycast only.

Measurements of the oriented samples were conducted in two configurations. One configuration, which we label as 'z', is when the orienting and the applied (SQUID) fields coincide, $(H||c)$. The other configuration, noted as '$\perp$', is when the oriented sample is rotated by 90° and thus the applied field is in the kagomé plane, $(H \perp c)$.

	T [K]	H [kG]
$ZnCu_3(OH)_6Cl_2$	$2 \leq T \leq 280$	$2 \leq H \leq 60$
Oriented $ZnCu_3(OH)_6Cl_2$	$2 \leq T \leq 280$	$0.1 \leq H \leq 60$
$Y_2Mo_2O_7$	$17 \leq T \leq 290$	$10 \leq H \leq 60$

Table 2.2: Magnetization measurements performed.

2.4 X-ray diffraction

X-ray diffraction is a powerful experimental tool, its uses ranges almost all fields of science, from biological specimen to physical or material engineering samples to medical applications (CT). X-ray is basically an electomagnetic wave. Diffraction uses a wavelength of $0.5 - 2\text{Å}$ which is the order of the distance between planes in a lattice. Impurity atoms can cause lattice distortions which can be detected by x-rays. Therefore it is essential to use high purity samples.

The use of synchrotron radiation gives an outstanding x-ray capabilities which is not available with standard laboratory sources. For example, in such synchrotron facility, the primary beam can be used to generate intense incident radiation, which is monochromatized better than $\Delta\lambda/\lambda < 10^{-4}$. Another aspect, it is possible to choose the optimal x-ray energy for a specific compound, which provides maximum diffraction intensity with a minimization of absorption effects. Thus, with a high brilliance source (the number of photons per phase space volume - photon/s/0.1% $BW/mm^2/mrad^2$ - 0.1%BW denotes a bandwidth $10^{-3}\omega$ centered around the frequency ω) we are able to perform very high resolution diffraction on a very small sample.

The x-ray work shown here has been carried out in the Material Science beam line (MS-X04) at Swiss Light Source (SLS) in PSI, Switzerland[48]. This beam line has

the capability of performing high resolution ($> 0.005°$), which is powerful for the investigation of small crystallographic changes. Calibration of the instrument and wavelength refinement were performed with Si standard samples and NAC ($NaCa_2Al_3F_4$) standard.

The instrument is as such that we apply an external field perpendicular to the incoming beam, $\mathbf{K}_i$. The multi-crystal detector scanned the outgoing wavevector $\mathbf{K}_o$. The angle between $\mathbf{K}_i$ and $\mathbf{K}_o$ is 2θ; thus the field made an angle θ with the scattering wavevector $\mathbf{q} = \mathbf{K}_o - \mathbf{K}_i$ (see Fig. 2.6, 2.7). The geometry is therefore fulfills,

$$\mathbf{q} = \mathbf{K}_o - \mathbf{K}_i$$

$$\mathbf{q}^2 = \mathbf{K}_o^2 + \mathbf{K}_i^2 - 2\mathbf{K}_o \cdot \mathbf{K}_i = \mathbf{K}_o^2 + \mathbf{K}_i^2 - 2K_oK_i \cos 2\theta$$

since we are concerned with elastic scattering ($h\nu = 0$) $|\mathbf{K}_o| = |\mathbf{K}_i| = 2\pi/\lambda$,

$$q^2 = 2k^2(1 - \cos 2\theta) = 2k^2(1 + \sin^2 \theta - 1)$$

thus,

$$q = \frac{4\pi}{\lambda} \sin \theta$$

2.4.1   The von-laue formulation for x-ray diffraction

We regard the crystal as composed of identical microscopic objects (the ions of the lattice) placed at sites $\mathbf{R}$ of a bravais lattice. Peaks will occur in directions and wavelengths for which the xray is scattered constructively.

The condition for constructive interference, for 2 scatterers with a displacement vector $\mathbf{d}$ is derived as follows. The incident x-ray with wavelength λ hence wavevector
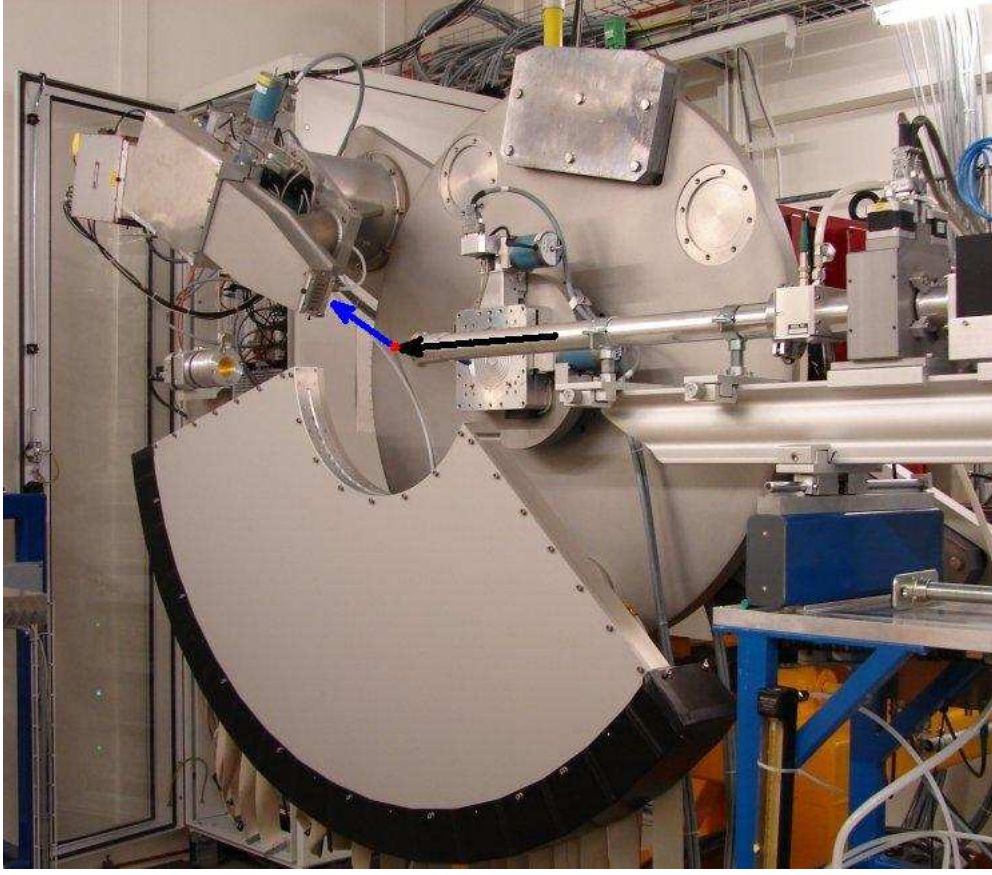
Figure 2.6: The MS X04 experimental hatch. The incoming beam wavevector $\mathbf{K}_i$ is shown by the black arrow, which is diffracted by the sample positioned at the red dot. The outgoing wavevector $\mathbf{K}_o$ is marked by the blue arrow.

$\mathbf{k} = 2\pi/\lambda \hat{\mathbf{n}}$ is diffracted to $\mathbf{k'} = 2\pi/\lambda \hat{\mathbf{n}}\text{'}$. The path difference of the x-ray beam diffracted from the 2 scatterers would be ,

$$d\cos(\theta) + d\cos(\theta') = \mathbf{d} \cdot (\hat{\mathbf{n}} - \hat{\mathbf{n}}'). \tag{2.66}$$

therefore, for a constructive interference,

$$\mathbf{d} \cdot (\hat{\mathbf{n}} - \hat{\mathbf{n}}') = m\lambda \tag{2.67}$$
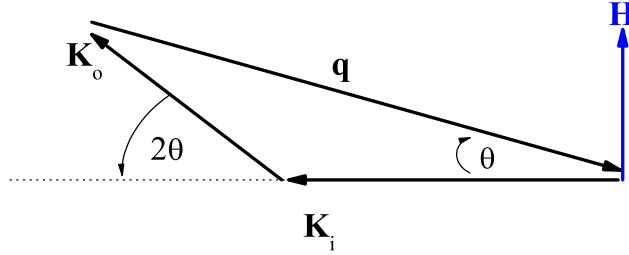
Figure 2.7: The incoming and outgoing wavevectors, $\mathbf{K}_i$ and $\mathbf{K}_o$. The field direction H and $\mathbf{q}$.

or by multiplying $2\pi/\lambda$,

$$\mathbf{d} \cdot (\hat{\mathbf{k}} - \hat{\mathbf{k}}') = 2\pi m \tag{2.68}$$

for an array of scatterers in a Bravais lattice, with $\mathbf{R}$ Bravias lattice vector, this equation turns out to be

$$\mathbf{R} \cdot (\hat{\mathbf{k}} - \hat{\mathbf{k}}') = 2\pi m \tag{2.69}$$

which equivalently is written,

$$e^{i(\hat{\mathbf{k}} - \hat{\mathbf{k}}') \cdot \mathbf{R}} = 1 \tag{2.70}$$

hence, *constructive interference will occur whenever the change in the wave vector,* $\mathbf{K} = \mathbf{k}' - \mathbf{k}$, *is a vector of the reciprocal lattice.* [reminder: $\mathbf{K}$ belongs to the reciprocal lattice of a bravias lattice of points $\mathbf{R}$, provided that $e^{i\mathbf{K} \cdot (\mathbf{r} + \mathbf{R})} = e^{i\mathbf{K} \cdot \mathbf{r}}$ for any $\mathbf{r}$]. An incident wave $\mathbf{k}$ will lead to a diffraction peak if the tip of the wave vector lies on a k-*space* Bragg plane.

2.4.2 Diffraction by monoatomic lattice with a basis

We consider the content of the primitive cell as a set of identical scatterers located at $\mathbf{d}_1, ..., \mathbf{d}_n$ within the cell. If the bragg peak which is associated with a change in the wave vector $\mathbf{K}' = $ k'-k, then the phase difference between the rays scattered at $\mathbf{d}_i$ and $\mathbf{d}_j$ will be $\mathbf{K} \cdot (\mathbf{d}_i - \mathbf{d}_j)$ and the amplitudes of the two rays will differ by a factor of $e^{i\mathbf{K} \cdot (\mathbf{d}_i - \mathbf{d}_j)}$. Thus, the amplitudes of the rays scattered from $\mathbf{d}_1, .., \mathbf{d}_n$ will be $e^{i\mathbf{K} \cdot \mathbf{d}_1}, .., e^{i\mathbf{K} \cdot \mathbf{d}_n}$. The sum of all rays scattered from the sites $\mathbf{d}_i$ is the net ray scattered from the entire primitive cell. It is known as *the geometrical structure factor*,

$$S_{\mathbf{K}} = \sum_{j=1}^{n} e^{i\mathbf{K} \cdot \mathbf{d}_j} \tag{2.71}$$

This factor expresses the extent to which interference of the waves scattered from identical ions within the basis can diminish the intensity of the bragg peak associated with the reciprocal lattice vector $\mathbf{K}$. The intensity of the bragg peak is proportional to the absolute value of the amplitude, therefore, $|S_{\mathbf{K}}|$. However it is not the only $\mathbf{K}$ dependance to the intensity, and therefore cannot be used alone to determine the absolute intensity of the peaks. But it can be used to determine where the intensity vanishes. This occurs when the elements of the basis are arranged so that there is a complete destructive interference for the $\mathbf{K}$ in question.

2.4.3 BCC scattering

since BCC is a bravais lattice, its reciprocal lattice is a FCC. Bragg reflections will occur when $\mathbf{K}$ will be a vector of the FCC. the basis of the BCC can be written by

the primitive vector $a(\hat{x} + \hat{y} + \hat{z})$ with the basis $\mathbf{d_1} = 0$ and $\mathbf{d_2} = a/2(\hat{x} + \hat{y} + \hat{z})$. Hence, the structure factor is

$$S_{\mathbf{K}} = 1 + e^{i\mathbf{K} \cdot \frac{a}{2}(\hat{x}+\hat{y}+\hat{z})} \tag{2.72}$$

A general vector in the reciprocal lattice can be written as

$$\mathbf{K} = \frac{2\pi}{a}(n_1\hat{x} + n_2\hat{y} + n_3\hat{z}) \tag{2.73}$$

therefore, the structure factor (substituting $\mathbf{K}$),

$$\begin{align}
S_{\mathbf{K}} &= 1 + e^{i\pi(n_1+n_2+n_3)} \tag{2.74}\\
&= 1 + (-1)^{n_1+n_2+n_3} \tag{2.75}\\
&= 2, n_1 + n_2 + n_3 \text{ even} \tag{2.76}\\
&\quad 0, n_1 + n_2 + n_3 \text{ odd} \tag{2.77}
\end{align}$$

2.4.4 FCC scattering

FCC is also a bravais lattice, where its reciprocal lattice is a BCC. the basis of the FCC can be written by the primitive vectors $a_1 = a/2(\hat{y} + \hat{z})$, $a_2 = a/2(\hat{z} + \hat{x})$ and $a_3 = a/2(\hat{x}+\hat{y})$. Additionally, the FCC can be written with a four-point basis, $a_1 = 0$, $a_2 = a/2(\hat{x}+\hat{y})$, $a_3 = a/2(\hat{y}+\hat{z})$ and $a_4 = a/2(\hat{z}+\hat{x})$. Therefore, the structure factor,

$$S_{\mathbf{K}} = 1 + e^{i\mathbf{K} \cdot a/2(\hat{x}+\hat{y})} + e^{i\mathbf{K} \cdot a/2(\hat{y}+\hat{z})} + e^{i\mathbf{K} \cdot a/2(\hat{z}+\hat{x})} \tag{2.78}$$

using a general vector in the FCC reciprocal lattice, $\mathbf{K} = 2\pi/a(h\hat{x} + k\hat{y} + l\hat{z})$, getting the structure factor,

$$\begin{align}
S_{\mathbf{K}} &= 1 + e^{i\pi \cdot (h+k)} + e^{i\pi \cdot (k+l)} + e^{i\pi \cdot (l+h)} \tag{2.79}\\
&= 1 + (-1)^{h+k} + (-1)^{k+l} + (-1)^{l+h} \tag{2.80}
\end{align}$$

for example, when $h + k$ odd and $k + l$ even and $l + h$ odd, $S_{\mathbf{K}} = 0$ for other combinations we can arrive to $S_{\mathbf{K}} = 4$ (when all sums are even).

2.4.5 Experimental Setup

The x-ray powder diffraction experiments were conducted in the Swiss Light Source Material Science (SLS-MS) beam line powder diffraction station. A collimated 14.9 keV x-ray beam was used with a high-resolution multicrystal analyzer. In order to perform the field-dependent X-ray diffraction experiment, we constructed a sample holder with two prism-shaped NdFeB permanent magnets (see Fig. 2.8, 2.9). Each prism was chopped at one edge, and the two chopped faces were held parallel and opposite each other at a distance of 1.5 mm. A glass capillary containing the powder sample was placed between these pole pieces in a 1.5 T field. In order to dismiss any grain orientation with the field, the powder was glued upon insertion to the capillary using cyanoacrylic glue (merz+benteli, Cementit CA 10) which is amorphi and doesn't give x-ray reflections.

The sample holder was placed inside a Janis cryostat in such a way that the field was perpendicular to the fixed incoming beam (see §2.4). In this configuration, the field direction could not be changed. The magnets could, of course, be removed for a ZF measurement. With the pole pieces in place the 2θ range was limited to $2\theta = 32°$ giving us access up to a q = 4.18 Å^{-1}, revealing clearly the (222), (440), (400) and (622) Bragg peaks. Other peaks allowed in this q-range have a small structure factor, and although measured they will not be discussed here.
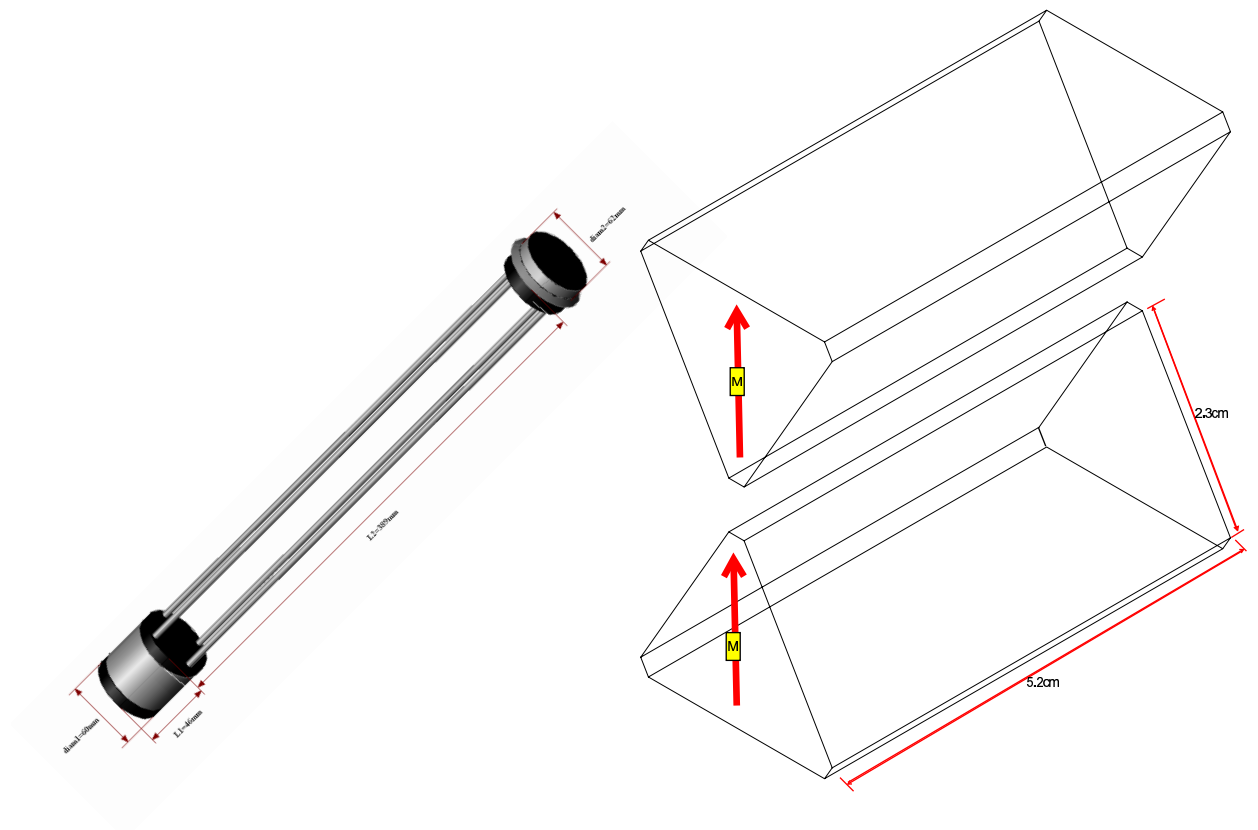
Figure 2.8: A drawing of the sample holder used in the SLS X04 Material Science Beamline.
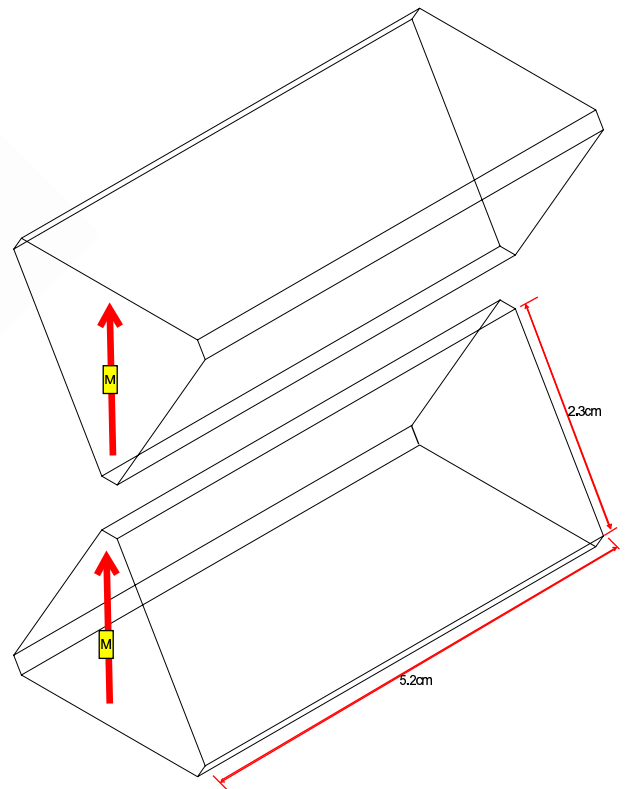
Figure 2.9: A sketch of the NdBFe permanent magnets, the arrows indicate the direction of the magnetic field produced.

Chapter 3

Results

In this chapter we review the experiments conducted. We characterize the $S = 1/2$ Kagomé $ZnCu_3(OH)_6Cl_2$ (§3.1.1 and §3.1.2) using local probes and susceptibility. We investigated the nature of the spin glass-like phase transition in the spin glass pyrochlore $Y_2Mo_2O_7$ (§3.2.1). Finally, in §3.2.2 we describe our study on the possibility of temperature-dependent lattice distortions in the pyrochlore compound $Tb_2Ti_2O_7$ by measuring the internal magnetic field distribution.

3.1   Kagome

In section §3.1.1 we characterize the ground state and excitation spectrum of the Herbertsmithite using the following measurements: SQUID magnetization, muon spin rotation frequency shift and transverse relaxation time T_2^*, and Cl nuclear spin-lattice relaxation T_1. We find no sign of a singlet formation, no long-range order or spin freezing, and no sign of a spin-Peierls transition even at 60mK (4 orders of magnitude lower than expected from Curie-Weiss). We find that the excited states are not gapped. In

section §3.1.2 we show measured data on oriented powder of Herbertsmithite which indicate a dramatic difference in magnetization measurements between in-plane and out-of-plane measurements. This difference is biggest at low applied fields or high-temperature. We believe that this difference emerges from super-exchange anisotropy and that Herbertsmithite is in fact an Ising-like system.

3.1.1 Herbertsmithite

Here, we present a comprehensive study of $ZnCu_3(OH)_6Cl_2$ using local probes. In our study, we address four questions which are at the heart of the investigation of the quantum kagomé system: Do $S = 1/2$ spins on kagomé lattice freeze? Is the ground state magnetic? Is there a gap in the spin energy spectra? Finally, does the lattice distort in order to accommodate spin-Peierls state? We address these questions in the present work using nuclear magnetic resonance (NMR) and muon spin resonance (μSR) local probes. We also use magnetization measurements to calibrate the local probes.

The $ZnCu_3(OH)_6Cl_2$ samples were prepared by hydrothermal reaction by the Nocera group at MIT, where it was first synthesized. Magnetic and pXRD data were consistent with those previously reported for herbertsmithite [27].

Magnetization measurements, m, were performed as described in §2.3.1. In Fig. 3.1 we present mT/H versus T. The data collapse onto a single line, especially at low T, meaning that the susceptibility is field-independent in our range of temperatures and fields. Also, no peak in the susceptibility is observed, indicating the absence of magnetic ordering. The only indication of interactions between spin in these measurements is the fact that mT/H decreases upon cooling whereas in an ideal paramagnetic
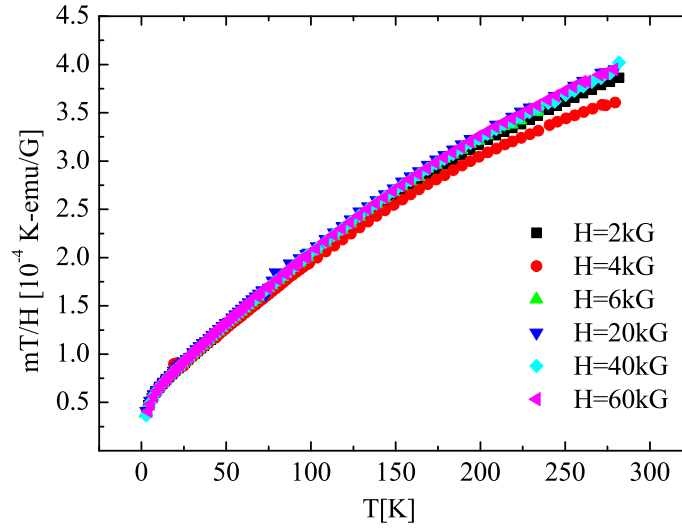
Figure 3.1: Normalized magnetization versus temperature

system this quantity should be constant; a paramagnetic system follows a Curie law,

$$\mathbf{m} = C \cdot \frac{\mathbf{H}}{T}$$

thus, $mT/H = C$ where C is the material Curie constant. In Fig.3.2 we demonstrate the linear fit to the high temperature χ^{-1} which reveals Θ_{CW}. The frustration parameter $T_F/|\Theta_{CW}| \approx 0.22$, where $T_F \sim 70$ K is the temperature at which χ^{-1} is no longer a linear function of T, indicates strong geometric frustration.

Muon spin rotation and relaxation (μSR) measurements were performed at the Paul Scherrer Institute, Switzerland (PSI) in the GPS spectrometer with an He cryostat, and in the LTF spectrometer with a dilution refrigerator. Data were collected at temperatures ranging from 60 mK to 200 K with a constant field of 2 kG. In Fig. 3.3 we show real and imaginary transverse field [TF] data taken at $H = 2$ kG and $T = 100$ K. The data are presented in a rotating reference frame (RRF). This frame
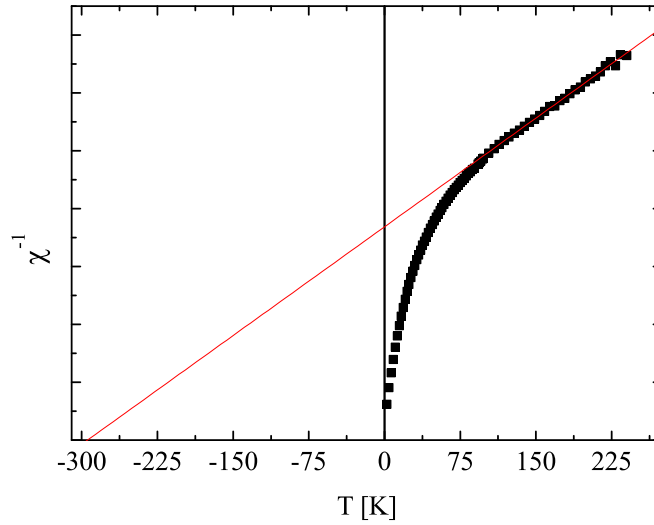
Figure 3.2: The inverse susceptibility, measured at 6 kG, of Herbertsmithite shows a Curie-Weiss constant of $|\Theta_{CW}| \sim 300$ K.

is always at a field of 100 G less than the applied field (2 kG). The TF asymmetry is best described by $A_{TF} = A_0 \exp\left(-t^2/(2T_2^{*2})\right)\cos(\omega t + \phi)$ where T_2^* is the transverse relaxation time, and ω is the frequency of the muon at the RRF. The quality of the fit is represented by the solid line.

In Fig. 3.4 we depict the frequency shift, $K = (\omega_0 - \omega)/\omega_0$ where ω_0 is the free muon rotation frequency in a field of 2 kG. The difference in frequency between free and implanted muons is a consequence of the sample magnetization; therefore, K is expected to be proportional to the susceptibility and field independent (See §2.1.1). Indeed, as shown in Fig. 3.4, for a fixed H there is a linear relation between K and the susceptibility $\chi = m/H$, with the temperature as an implicit parameter; some representative temperatures are shown on the upper axis. In Fig. 3.5 we present
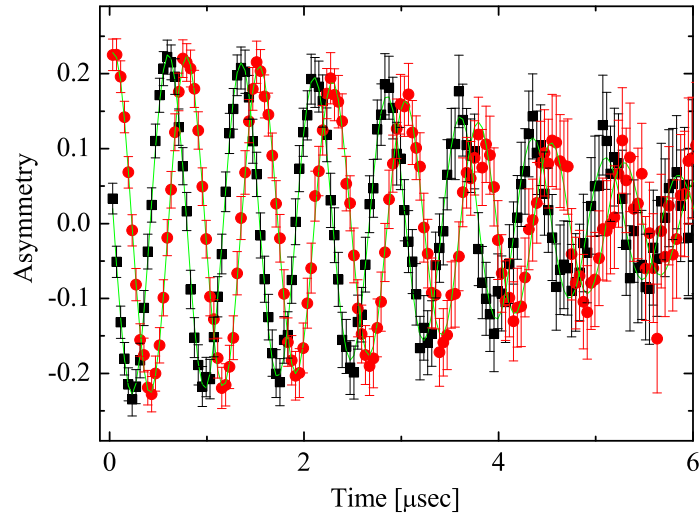
Figure 3.3: A plot of the real and imaginary transverse field asymmetry for
$T = 100$ K.

the field dependence of K at $T = 100$ K. Surprisingly, K is field dependent. This anomalous field dependence of K is not clear at the moment.

In Fig. 3.6, we depict K as a function of temperature down to 60 mK. An additional axis is presented where K has been converted to χ as discussed above. We find that K (and hence χ) increases with decreasing temperatures and saturates below $T \sim 200$ mK at a value of $\chi = 15.7(5) \times 10^{-3}$ cm^3/mol Cu; the error is from the calibration. It should also be pointed out that the energy scale associated with spin 1/2 in a field of 2 kG is 200 mK, and the saturation could be a consequence of the external field. This behavior could also be a consequence of an ising-like kagomé system, which is explained in §3.1.2. The saturation of χ is a strong evidence for the lack of impurities in our sample. More importantly, it indicates the lack of singlet
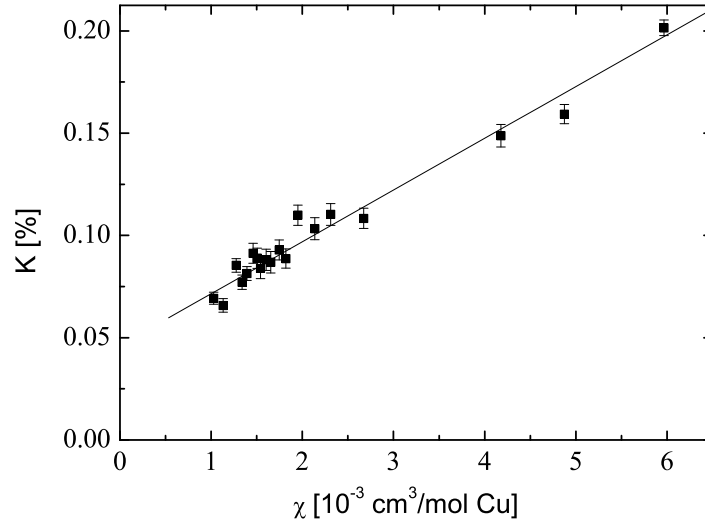
Figure 3.4: The muon shift K against susceptibility.

formation or spin freezing. The last conclusion is also in agreement with neutron scattering measurements [37] and zero field μSR [49].

The muon transverse relaxation rate $1/T_2^*$ is also presented in Fig. 3.6. Roughly speaking, it has the same temperature behavior as the shift (and as the susceptibility). T_2^* relaxation is a result of defects in the sample causing a distribution of muons to electronic spin coupling constants or a distribution of susceptibilities. It has been shown that when the muon relaxation rate behaves similarly to the shift [50](see §2.1.1) (or susceptibility [5][46]) upon cooling, it indicates quenched distribution of either the coupling constants or susceptibilities. In this case the relaxation increases simply because the average moment size increases. Since the coupling constants and susceptibility are functions of distances between muon and electronic spin or between two electronic spins, our results are consistent with a lack of lattice deformation in
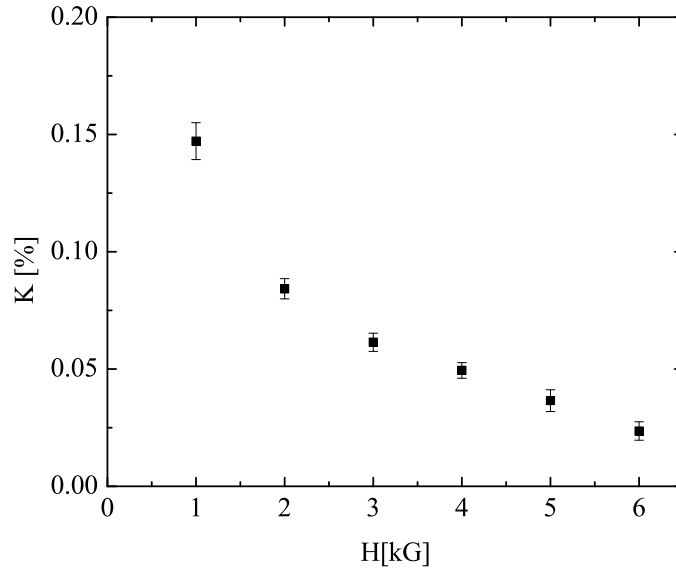
Figure 3.5: The muon shift K versus external field H at $T = 100$ K.

$ZnCu_3(OH)_6Cl_2$.

We also performed ^{37}Cl and ^{35}Cl NMR experiments on the same sample. Using the two isotopes, we are able to determine the origin of T_1. The first step in such a measurement is to find the line shape and to identify the isotopes and transitions. This measurement was done at a constant applied frequency of $\nu_{app} = 28.28$ MHz and a varying external field H. A standard spin-echo pulse sequence, $\pi/2 - \tau - \pi$, was applied, and the echo signal was integrated for each H. In Fig. 3.7 we show a field sweep for both Cl isotopes obtained at $T = 100$ K. A rich spectrum is found and is emphasized using five x-axis and one y-axis breakers. This rich spectrum is a consequence of the Cl having spin 3/2 for both isotopes. In the case where the nuclei reside in a site with non cubic local environment and experience an electric
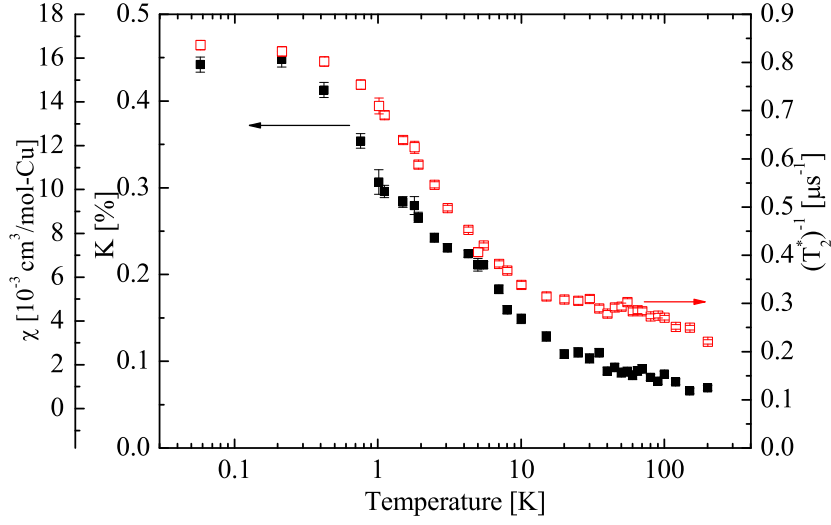
Figure 3.6: A plot of the muon shift K and transverse relaxation time σ, versus temperature.

field gradient, their spin Hamiltonian could be written as

$$\mathcal{H} = -h\nu_l \mathbf{I} \cdot (1 + \mathbf{K}) \cdot \widehat{\mathbf{H}} + (h\nu_Q)/6 \left[3I_z^2 - I^2 + \eta \left(I_x^2 - I_y^2 \right) \right]$$

where ν_Q is the quadrupole frequency, $0 \leq \eta \leq 1$ is the anisotropy parameter, $\mathbf{K}$ is the shift tensor, and $\nu_l = \gamma H/(2\pi)$. The powder spectrum of such nuclei has two satellite peaks corresponding to the $3/2 \longleftrightarrow 1/2$ and $-3/2 \longleftrightarrow -1/2$ transitions, and a central line from the $1/2 \longleftrightarrow -1/2$ transition, which is split due to the powder average. The transition names are presented in the figure. The satellite peaks at $T = 100$ K of ^{35}Cl are at 6.52 and 7.07 T, and for ^{37}Cl at 7.91 and 8.41 T. The lack of singularity in the satellite spectrum indicates that the Cl resides in a site with $\eta > 0$, namely, with no xy symmetry.

In contrast to the two satellites, the splitting of the central lines at $T = 100$ K

is clear, and appear for the ^{35}Cl at 6.778 and 6.801 T and for the ^{37}Cl at 8.148 and 8.161 T. Under some assumptions these values could be used to determine the parameter of the nuclear spin Hamiltonian [51]; assuming that the nuclear spin operators, I_x, I_y and I_z are collinear with the principal axes of the shift tensor, and that the in-plane shift is isotropic with $K_\perp = (K_x + K_y)/2$, we find for both isotopes, $K_\perp \simeq -0.0017(5)$, $K_z \simeq 0.035(9)$ and $\eta = 0.4$, and $^{35}\nu_Q = 3.75$ MHz and $^{37}\nu_Q = 2.55$ MHz. The ratio of ν_Q is as expected from the ratio of the quadrupole moments. Due to the assumptions, the value of K_z should only be considered as an order of magnitude. Nevertheless, it is interesting to compare it to the muon shift. Assuming that K_{rrf} can be extrapolated to 6 T, we expect the muon shift at this field to be $K_{lab} \sim 10^{-5}$ which is much smaller than the Cl shift. This means that Cl experiences a much stronger field generated by the Cu spins, which for muons is usually a dipolar field.

Temperature dependence field sweeps of the ^{35}Cl central line are shown in Fig. 3.8. The intensities are in arbitrary units for clarity. The $\pm 1/2 \longleftrightarrow \mp 1/2$ transitions are easily observed at $T = 300$ and 100 K (indicated by the arrows in the figure) but are smeared out at lower T. In fact, the lines become so broad that the NMR shift cannot be followed to low temperature; hence the importance of the μSR results. In fact, the lack of Cl and H shift on one hand, and the observation of oxygen [52] and muon shift on the other hand are very intriguing and not at all clear. Nevertheless, the ability to detect the Cl signal even at 5 K is a strong indication for the absence of spin freezing at this temperature. For comparison, in the kagomé system $SrCr_8Ga_4O_{19}$, where spin freezing is taking place at 4 K, the NMR signal nearly completely disappears at 10 K [53]. Therefore, the increasing line width with decreasing temperature is a result of a distribution of hyperfine fields and an increasing susceptibility, but without a full
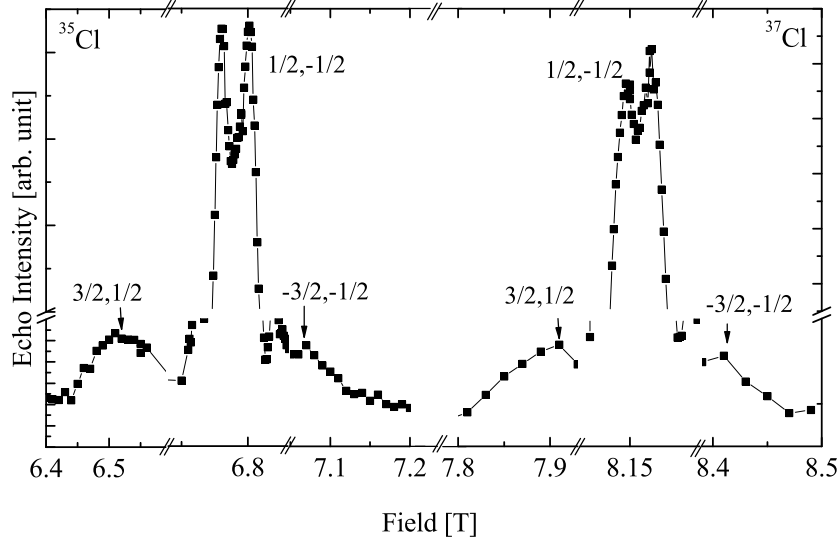
Figure 3.7: A field sweep of ^{35}Cl and ^{37}Cl.

phase transition. Finally, we cannot detect a shift of the Cl line upon cooling in contrast to Ref.[2].

Finally, we measured the ^{37}Cl spin-lattice relaxation rate T_1^{-1} to determine spin gap and excitation spectrum. The data were taken at a field of 8.15 T which corresponds to the low field peak of the central line. We use a saturation recovery pulse sequence. In Fig. 3.9 we depict T_1^{-1} normalized by γ^2 where $^{37}\gamma = 3.476$ MHz/T on a semi-log scale. T_1^{-1} increases upon cooling down to 50 K and then sharply decreases. We also present ^{35}Cl $(T_1\gamma^2)^{-1}$ where $^{35}\gamma = 4.172$ MHz/T below 50 K in order to determine the origin of the dynamic fluctuations. These measurements were done under the same conditions as ^{37}Cl. When considering all temperatures we find that $T_1^{35}/T_1^{37} = 0.75(10)$. From a magnetic relaxation mechanism we expect this
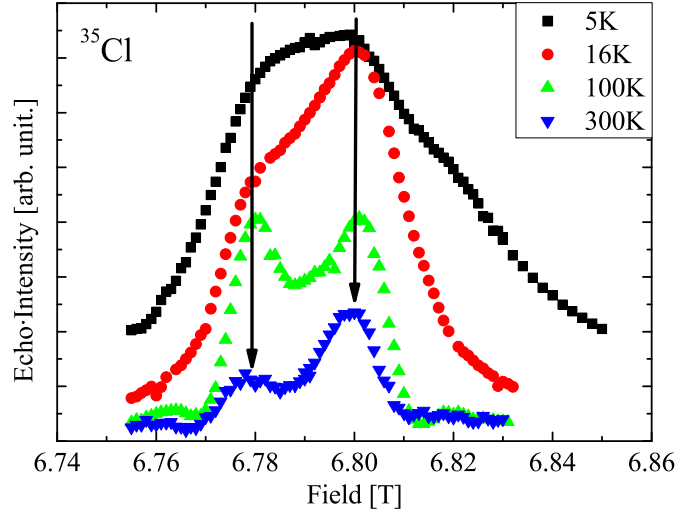
Figure 3.8: ^{35}Cl field sweep ($\nu = 28.28 MHz$) at different temperatures. The arrows indicate the central line singularities observed at high-T but smeared out at low T.

ratio to equal $(^{37}\gamma/^{35}\gamma)^2 = 0.69$. From a quadrupole based mechanism we anticipate $(^{37}Q/^{35}Q)^2 = 0.62$ where Q is the nuclear quadrupole moment. Our finding is in favor of relaxation mediated by a magnetic mechanism as indicated by the overlapping $(T_1\gamma^2)^{-1}$ data points in Fig. 3.9.

The most noticeable feature in this figure is that $1/T_1$ decreases with decreasing temperature much more slowly than Arrhenius law ($k = A\exp(-E/(kT))$) expected when a gap opens. A remanent relaxation at zero temperature $1/T_1^n$ could be due to magnetic fluctuations from other nuclear moments such as the protons or copper, since they continue to fluctuate even when the electronic moments stop. A standard approach to T_1 interpretation is in terms of magnon Raman scattering where

$$\frac{1}{T_1}(T) = \frac{1}{T_1^n} + \gamma^2 A^2 \int_\Delta^\infty \rho^2(E) \cdot n(E) \cdot [n(E) + 1] \, dE \qquad (3.1)$$
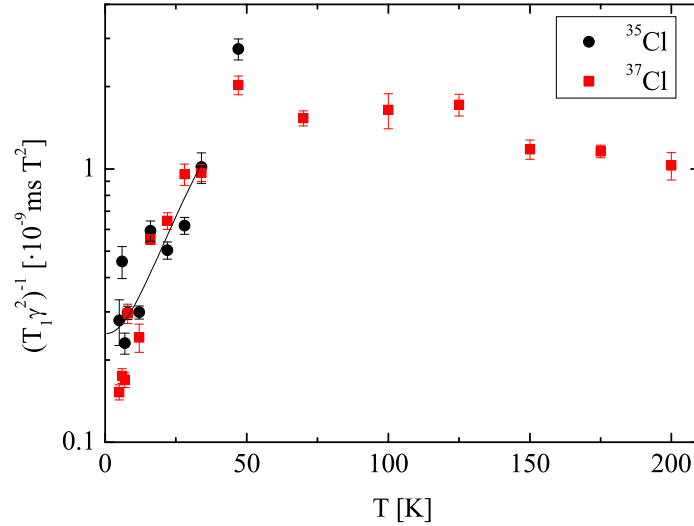
Figure 3.9: A semi-log plot of the Cl inverse spin-lattice relaxation, $(\gamma^2 T_1)^{-1}$, versus temperature.

with ρ being the density of states, Δ the gap, A is a constant derived from the hyperfine coupling, and $n(E)$ the Bose-Einstein occupation factor [54]. This expression is constructed from the population of magnons before and after the scattering, with the associated density of states and the assumption that they exchanged negligible amount of energy with the nuclei since its Zeeman splitting is much less than a typical magnon energy. However, in frustrated magnets the magnon might not be the proper description of the excitations [51, 53]. Nevertheless, with no other available theory we use Eq. 3.1. We assume $\rho(E) \sim E^\alpha$, with α and Δ as fit parameters. The fit of Eq. 3.1 to the data is presented as the solid line in Fig. 3.10. We find $\alpha = 0.23(1)$ and $\Delta = 0.5(2)$ K. We also present a linear fit, which is the case for a fermionic excitation spectrum, where $T_1 \propto T^{-1}$. In Fig. 3.11 we show similar data presented recently by

Imai *et al.* [2] using oriented powder and stronger magnetic field, and the same fit. In
this case we find $\alpha = 0.59(3)$ and $\Delta = 0.002(3)$ K. A linear function can be ruled out
easily with this data set, thus excluding the fermonic excitation picture. Comparing
to $J \sim 200$ K [37], the gap is negligibly small and indicates that, in fact, there is no
gap in the spin energy spectra, in agreement with Ref. [37]. Both data sets further
suggest that the density of states at low energy diminishes.
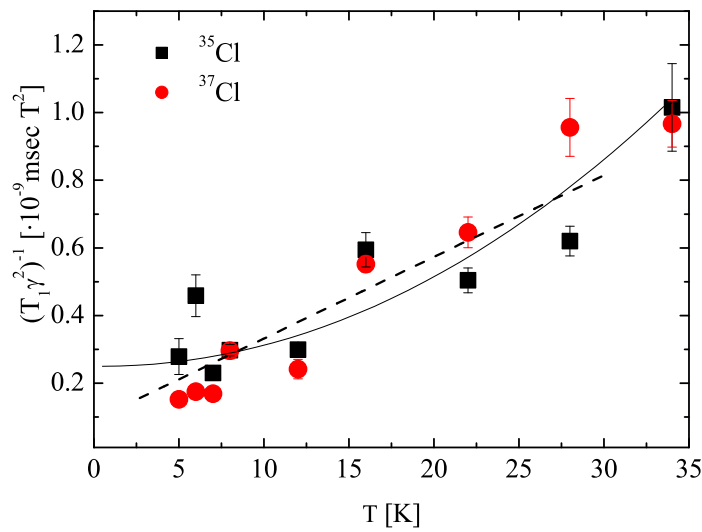
Figure 3.10: The inverse spin-lattice relaxation T_1^{-1}. The solid line is a fit to
Eq. 3.1, the dashed is a linear fit.

To conclude, susceptibility measurements down to 60 mK suggest that there is
no freezing and only a saturation of susceptibility, namely, no singlet formation. The
data also do not support the presence of lattice deformation. Finally, in our Cl NMR
T_1 measurements no sign of a spin gap was detected. Thus, $ZnCu_3(OH)_6Cl_2$ is an
exotic magnet with no broken continuous symmetry but gapless excitations. It might
be an example of algebraic spin liquid [55].
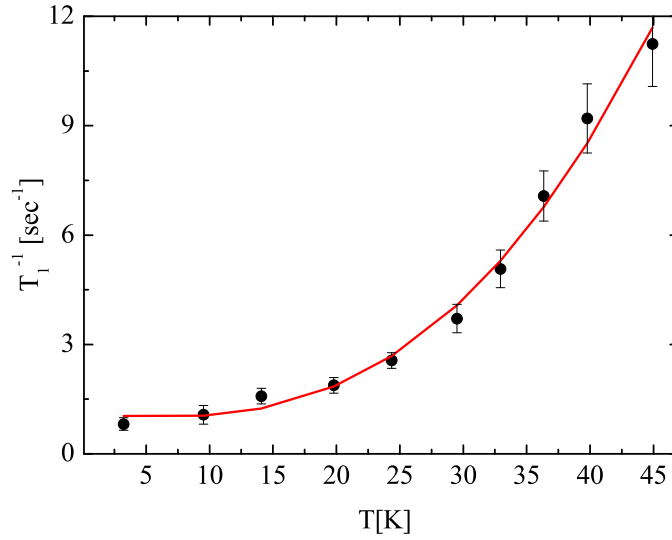
Figure 3.11: The inverse spin-lattice relaxation T_1^{-1} taken from Ref. [2]. The solid line is a fit to Eq. 3.1.

3.1.2 Oriented Herbertsmithite

Unfortunately, Hertbertsmithite is only available as a powder, thus the symmetries of its spin Hamiltonian are not clear despite various experimental studies[1, 30, 33, 35, 36, 49]. To clarify these symmetries we present magnetization measurements on oriented powder of $ZnCu_3(OH)_6Cl_2$ along $(\hat{z})$ and perpendicular to $(\perp)$ the orienting field. The symmetry of the interactions are probed at high temperatures where impurities are not expected to contribute to the susceptibility and all probes roughly agree.

In Fig. 3.12 we plot the x-ray diffraction from the powder and oriented samples. The x-ray momentum transfer is parallel to the orientation field. The Bragg peak intensities are shown in the figure. In the oriented case the (002) and (006) peaks

increased dramatically, while many of the other peaks did not. This x-ray picture shows a high degree of orientation such that the c direction is parallel to the field. The level of orientation will be discussed further below.
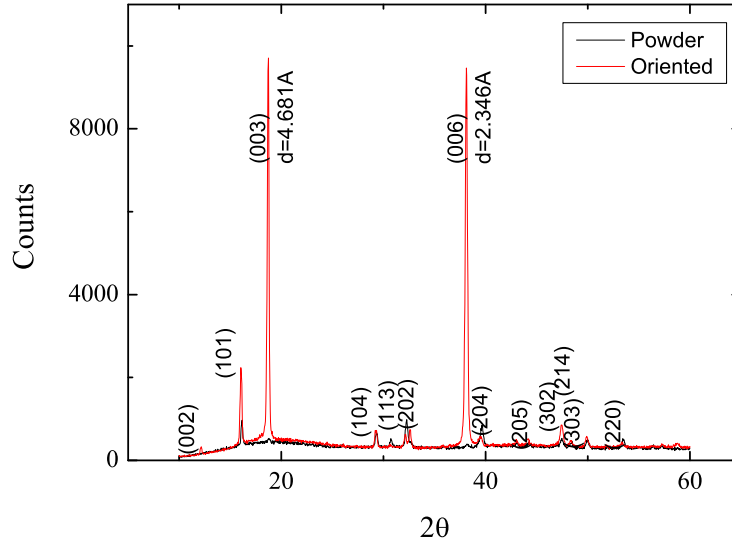
Figure 3.12: X-ray diffraction of powder (black) and oriented powder (red) with the transferred momentum parallel to the orientation field.

DC magnetization measurements, M, were performed as described in §2.3.1. In Fig. 3.13 we present χT ($\chi \equiv M/H$) of the two samples, powder and oriented balls. These measurements were taken at $H = 400$ G. They are conducted as follows: we first measured the powder sample and then the oriented sample in both configurations. Finally, we repeated the powder measurements for a second time, but rotated the powder ball as if it was oriented. All powder measurements collapse into a single curve, as expected, demonstrating the reproducibility of the measurement. The Stycast

sample showed a very small diamagnetic signal also depicted in Fig. 3.13. The core diamagnetic susceptibility of $ZnCu_3(OH)_6Cl_2$ is -16.7×10^{-5} cm^3/mole [56]. The Van-Vleck contribution is expected to be of the same order of magnitude, but with a positive sign [57]. Both are much smaller than the measured susceptibility at room temperature of 1×10^{-3} cm^3/mole.
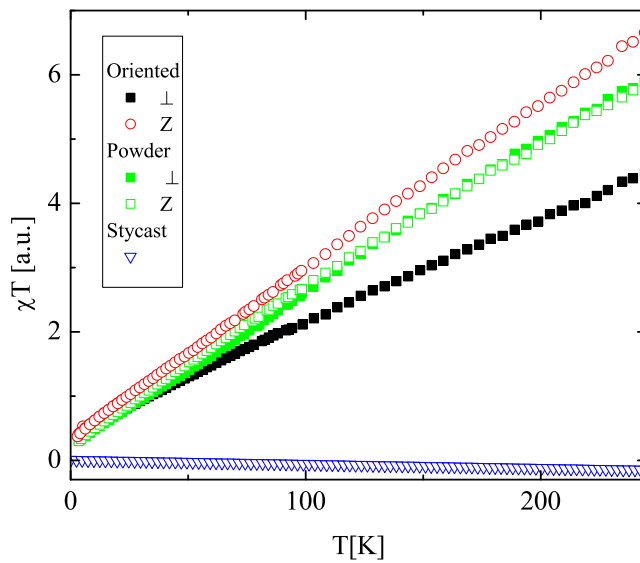
Figure 3.13: Susceptibility times the temperature versus temperature at external field of 400 G for oriented sample in two directions, powder sample in two directions as if it was oriented, and Stycast sample.

In Fig. 3.13 no special energy scale is found in either one of the measurements. In fact, this measurement is similar to the previously observed powder high field measurements (see §3.1.1)[38]. Again, the only indication of an interaction between spins is the fact that χT for both direction and the powder decreases with decreasing T. However, χT of the powder is smaller than $\chi_z T$ and larger than $\chi_\perp T$ of the oriented

sample. A comparison of the absolute value of the susceptibility of the powder and the oriented sample is not accurate. We did try to have an equal amount of sample in both balls but there is no telling how successful we were. A more relevant comparison is between the susceptibilities in the different directions of the oriented sample; $\chi_z T$ increases faster than $\chi_\perp T$, and at room temperature $\chi_z = 1.6 \chi_\perp$. Thus the ratio between the z and $\perp$ directions increases as the temperature increases.
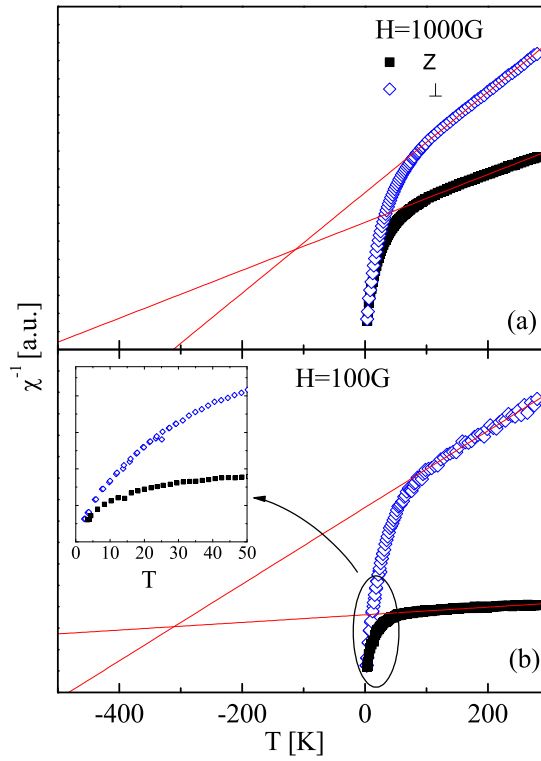
Figure 3.14: Inverse susceptibility versus temperature at $H = 1$ kG (a) and at $H = 100$ G (b). The solid lines are linear fits to the high temperature (> 150 K) data. (a) In inset of (b) we plot the low-temperature behavior of χ^{-1} at 100 G.

In Fig. 3.14 we plot the inverse susceptibility versus temperature for two fields,

1000 and 100 G and for the two orientations. In the inset of Fig. 3.14(b) we plot

the inverse susceptibility at low temperatures ($T < 50$ K); clearly, χ_z linearizes at

$T \sim 30$ K whereas $\chi_\perp$ linearizes at a much higher temperature ($T \sim 100$ K). θ

, and C in arbitrary units are extracted from a linear fit of the high-temperature

($150 < T < 280$ K) data to $\chi_{\perp,z}^{-1} = (T + \theta_{\perp,z})/C_{\perp,z}$. The fits are shown by the solid

line.

In Fig. 3.15 we plot $\theta_{\perp,z}$, and $\sqrt{C_{\perp,z}}$ which is proportional to the $g_{\perp,z}$ factor (if the

sample was fully oriented) versus the applied field. $\theta_\perp$ increases slowly with decreasing

applied field and saturates below 400 G. On the other hand, θ_z increases rapidly below

2 kG. The Curie constant has a similar behavior. The powder average of $\theta_{\perp,z}$ at low

fields does not reconcile with $\theta \sim 300$ K measured in a powder and there must be

some extrinsic contribution to the susceptibility in the partially aligned samples at

low fields. In contrast, at high fields, $H > 2$ kG, θ of the two directions is hardly

distinguishable and on the order of the powder value. In addition, useful information

can be extracted from the CW temperature only if it is obtained by measurements

at $T \gtrsim \theta$. Therefore, we concentrate on the results obtained by $H \geq 2$ kG, as shown

in the inset of Fig. 3.15.

In order to convert, the measured susceptibility χ presented above to the intrinsic

susceptibility χ^i in different directions, it is important to estimate the level of orien-

tation. This can be done using the x-ray data. The ratio (R) of the x-ray intensity

(I) from two different planes is,

$$R = \frac{I(00h)}{I(kk0)} \ . \tag{3.2}$$

We now assume that there are N grains composed of two sets and α is the probability

that a grain orients. Thus αN are grains that orient perfectly with the field, and
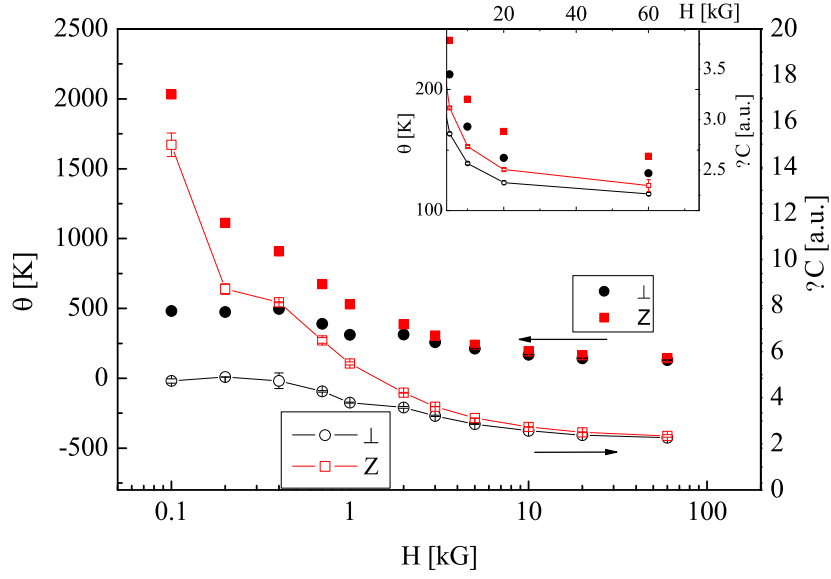
Figure 3.15: The Curie-Wiess temperatures and square root of the Curie constant of the oriented sample perpendicular to and in the kagomé plane. The inset show a zoom on the high field data.

$(1 - \alpha)N$ that are not effected by the field at all since they are made of a few crystalline, for example. We further define β as the probability that a particular plane will contribute to the scattering intensity in a powder. Therefore Eq. 3.2 can be written as,

$$R = \frac{N\beta a(h)}{N\beta b(k)} = \frac{a(h)}{b(k)} \tag{3.3}$$

where $a(h)$ and $b(k)$ are the intensities from $(00h)$ and $(kk0)$ plane. After orientation we have $N\alpha$ grains that are fully polarized with the field, and are perpendicular to $\mathbf{q}$. We also have $N(1 - \alpha)$ grains that did not change their orientation, out of these $N(1-\alpha)\beta$ planes are perpendicular to $\mathbf{q}$. The x-ray intensity ratio between the same

planes would be,

$$R' = \frac{I'(00h)}{I'(kk0)} = \frac{N\alpha a(h) + N\beta(1-\alpha)a(h)}{N\beta(1-\alpha)b(k)} \qquad (3.4)$$

$$= \left(\frac{\alpha + \beta(1-\alpha)}{\beta(1-\alpha)}\right)\frac{a(h)}{b(k)} = \left(1 + \frac{\alpha}{\beta(1-\alpha)}\right)R \qquad (3.5)$$

Looking at the extremes, if all grains orient and $\alpha = 1$ $R' \to \infty$. If there are no grains that orient and $\alpha = 0$ then $R' = R$. From Eq. 3.5 we find,

$$\beta\left(\frac{R'}{R} - 1\right) = \frac{\alpha}{1-\alpha} \qquad (3.6)$$

We now can estimate β from the width of the peaks which is 0.2° out of 180°, thus $\beta \sim 0.001$ (see Fig. 3.16). For the intensity calculation we need to subtract the
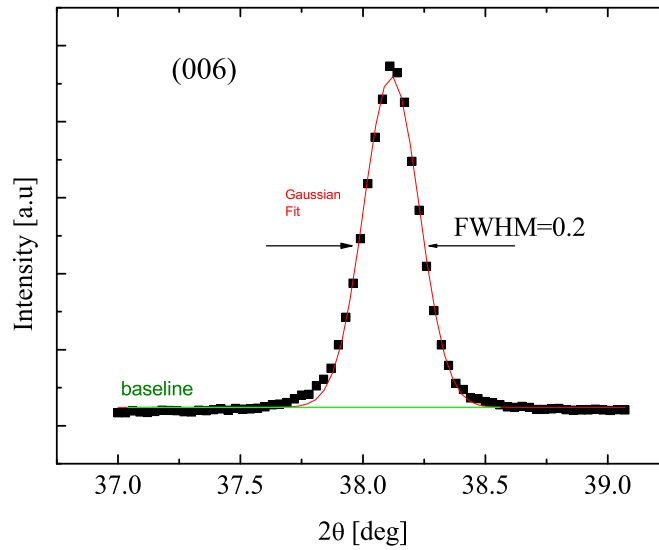
Figure 3.16: A gaussian fit to (006) bragg peak reveals the width of the peak to be $\beta = 0.225(1)°$

background,

$$(006): \begin{pmatrix} I \\ I' \end{pmatrix} = \begin{pmatrix} 385 - 314(2) \\ 9190 - 484(20) \end{pmatrix} = \begin{pmatrix} 71(2) \\ 8706(20) \end{pmatrix} \qquad (3.7)$$

$$(220): \begin{pmatrix} I \\ I' \end{pmatrix} = \begin{pmatrix} 502 - 294(2) \\ 414 - 325(3) \end{pmatrix} = \begin{pmatrix} 208(2) \\ 89(3) \end{pmatrix} \qquad (3.8)$$

thus,

$$R = \frac{71(2)}{208(2)} = 0.34(1) \qquad (3.9)$$

$$R' = \frac{8706(2)}{89(3)} = 97(3) \qquad (3.10)$$

$$\frac{R'}{R} = 285(8) \qquad (3.11)$$

thus, using Eq. 3.6 we find $\alpha = 0.26(2)$. This level of orientation is in agreement with Imai $et\ al.$[2].

In an oriented sample we expect

$$\chi_{z,\perp} = (1 - \alpha)\left(\frac{1}{3}\chi_z^i + \frac{2}{3}\chi_\perp^i\right) + \alpha\chi_{z,\perp}^i. \qquad (3.12)$$

This relation could be inverted to produce $\chi_{z,\perp}^i$. In Fig. 3.17 we present both $1/\chi_{z,\perp}$ and $1/\chi_{z,\perp}^i$ for the susceptibility data taken at $H = 1000$ G. New intrinsic CW temperatures $\theta_{z,\perp}^i$ could be obtained from $1/\chi_{z,\perp}^i$ as demonstrated by the dashed lines. $\theta_{z,\perp}^i$ represent the CW temperature as if the sample was fully oriented. Although α is just an estimate of the level of orientation, the important point is that $\theta_z^i > \theta_z$ and $\theta_\perp^i < \theta_\perp$.

We now turn to discuss the possible origin of the susceptibility anisotropy in terms of superexchange anisotropy and DMI (see §1.2). Since the sum of $\mathbf{D}_{ij}$ around each spin cancels[22]§1.3.1, DM does not contribute to the CW law. If the sample was
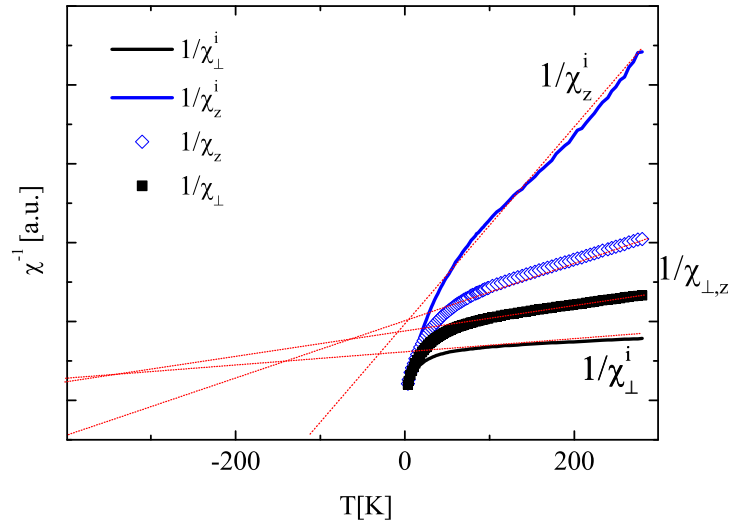
Figure 3.17: inset displays the inverse measured susceptibility $1/\chi_z$ and $1/\chi_\perp$, and the inverse intrinsic susceptibility $1/\chi_z^i$ and $1/\chi_\perp^i$ obtained from Eq. 3.12. The dashed lines demonstrate that $\theta_Z < \theta_Z^i$ and $\theta_\perp > \theta_\perp^i$.

perfectly oriented we would have $\theta_{z,\perp}^i = J_{z,\perp}/k_B$. Since our sample is not perfectly oriented, our high-temperature high field linear fits of $\chi_{\perp,z}^{-1}$ measures a lower bound on J_z and an upper bound on $J_\perp$.

The lower bound on J_z is larger than the upper bound on $J_\perp$. Despite the fact that measurement of χ_z and $\chi_\perp$ are contaminated with $\chi_\perp^i$ and χ_z^i respectively, as indicated by Eq. 3.12, the conclusion $J_z > J_\perp$ is unavoidable. It is robust even against possible core and Van-Vleck corrections. Thus herbertsmithite has an Ising-like exchange anisotropy. This, however, is not the end of the story. If $J_z > J_\perp$, we would expect $\chi_z < \chi_\perp$, in contrast to observation. Therefore, to explain the high susceptibility in the z direction we must invoke an anisotropic g factor as well.

The classical ground state of an antiferromagnet kaogme with exchange anisotropy has a net ferromagnetic order with finite total magnetization (§1.3.1). We believe that this ferromagnetic order contributes to the observed χ at $T \to 0$ by transverse field (TF) muon spin rotation (μSR) experiment [38] (see §3.1.1). In μSR impurities are expected to contribute to the muon line width while most of the sample contributes to the line shift. In what follows we examine what part of the μSR data can be explained by exchange anisotropy only. A complete understanding will of course require taking DMI interaction into account as well.

The μSR data are reproduced in Fig. 3.18. χ increases sharply with decreasing temperatures between ~ 10 K and ~ 1 K and saturates below $T \sim 200$ mK at a value of $\chi = 15.7(5) \times 10^{-3}$ cm^3/mol Cu. This susceptibility mounts to an average moment of $0.006\mu_B$ per Cu, in the direction of the applied 2 kG field. Eq.1.15 indicates a small ferromagnetic moment in an anisotropic kagome. A small field will stabilize this moment and a powder average of its projection on the field direction will be given by,

$$\left\langle \mathbf{M} \cdot \hat{\mathbf{H}} \right\rangle = \frac{\mu_B}{2}(1 + \cos\varphi) \tag{3.13}$$

Solving Eq. 3.13 for the anisotropies gives $J_z/J_\perp = 1.06$. In Fig. 3.3 we show simulations described in Ref. [58], for $J_z/J_\perp = 1.04$ and $J_z/J_\perp = 1.08$ showing similar behavior as the experiment. For this type of exchange anisotropy the expected $T_c/J_\perp = 0.03$ as shown in the inset of Fig. 3.3 also taken from Ref. [58]. For $J_\perp \simeq 200$ K we expect $T_c = 6$ K. This temperature is at the center of the sharp rise of χ. Thus we see that both the very low T and the very high T susceptibility detected by μSR can qualitatively be explained by exchange anisotropy. However, the intermediate T are smoother in the real data, and the sudden increase in the magnetization, predicted in the simulated case, is missing.
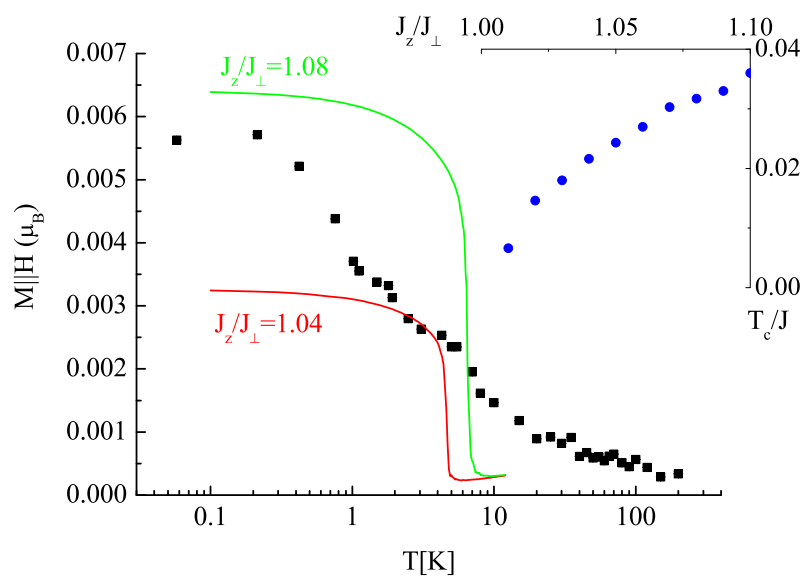
Figure 3.18: A plot of the magnetization detected by muon spin rotation versus temperature, and simulation data for antiferromagnetic kagomé lattice with Ising like exchange anisotropy as in Ref. [4]. In the inset the normalized critical temperature versus the exchange anisotropy is shown.

To summarize, our measurements in $ZnCu_3(OH)_6Cl_2$ reveal an anisotropic intrinsic spin susceptibility with $\chi_z^i > \chi_\perp^i$ possibly due to anisotropic g factor. At fields above 2 kG a CW temperature can be consistently determined in two different directions. By mean-field approximations we were able to show that this phenomenon can be explained only by an anisotropic super-exchange constants where $J_z > J_\perp$. This anisotropy can explain the main features of the susceptibility determined by μSR.

3.1.3   Conclusions

Experimental data has been reviewed on powder and oriented powder samples of Herbertsmithite. μSR, NMR and susceptibility all show different behaviors which could not be fully explained.

Using oriented powder samples reveal an appearance of an Ising-like exchange anisotropy which in turn explains the μSR data. However, it is still an open question regarding the various shifts measured by NMR. Additionally, μSR does not detected any lattice distortions. Cl NMR T_1 measurements indicate zero gap to excitations.

3.2   Pyrochlores

While J anisotropy is found in herbertsmithite, distortion is not observed in this case (§3.1.1). As mentioned earlier (§1.4.2), a magneto-elastic coupling and distortion possibly affects the pyrochlore $Y_2Mo_2O_7$.

3.2.1 $Y_2Mo_2O_7$

However, The smoking gun proof that the distortion in $Y_2Mo_2O_7$ is driven by the magnetic interaction is still lacking. Such evidence could be provided by the experimental observation of lattice distortions upon the application of an externally applied magnetic field. Here we extend previous ^{89}Y NMR measurements[19], which were limited to nitrogen temperature, to the helium range. We also performed field-dependent high-resolution x-ray powder diffraction.

In Fig. 3.19 we plot the cubic (222) (main panel) and (440) (inset) peaks without at zero-field (ZF) at three temperatures (above T_g at 55 K, near T_g, at 28 K, and below T_g at 16 K). The peak intensities are temperature-independent both in shape and intensity, they are progressively shifted up by 10 counts/min for clarity. Additionally, all reflections measured are consistent with the face centered cubic structure; however, they are significantly broader than the instrumental resolution even at room temperature.

In Fig. 3.20 we plot the (440) Bragg peak at three temperatures (above T_g at 220 K, near and below T_g) taken with the application of the field. The only experimental finding, is a narrowing of the (440) peak at $T = 28$ K upon the application of the field. This narrowing occurs only just above T_g, and is absent at higher or lower Ts. The effect of a magnetic field on the lattice properties clearly indicates the presence of magneto-elastic coupling. The fact that T_g is close to the temperature when the distortion is optimized indicates that magnetic interactions drive the distortion and not vice versa. This is not a strong enough proof of the frustration-driven-distortion for which we were looking.

Another interesting experimental finding is that at $T < T_g$, with no field applied, there is a clear indication of multiple discrete peaks with a width comparable to the
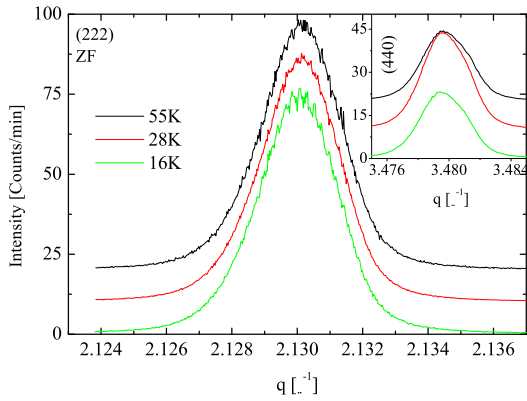
Figure 3.19: ZF x-ray scattering from $Y_2Mo_2O_7$. The (222) Bragg scattering at $T = 55$ K, $T = 28$ K and $T = 16$ K. In the inset, the (440) Bragg reflection.
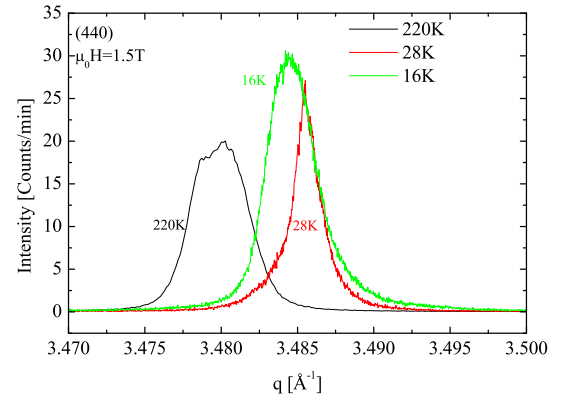
Figure 3.20: X-ray scattering from $Y_2Mo_2O_7$ with $H = 1.5$ T applied. The (440) Bragg scattering at $T = 220$ K, $T = 28$ K and $T = 16$ K.

instrumental resolution. A closer look at the ZF (222) peak at 16 K is plotted in Fig. 3.21. We index the vector, q_{max}, at which the local maxima are found by n. We found that $q_{max}(n)$ is a linear function of n as demonstrated in the right inset of Fig. 3.12b. Interesting similar phenomena were found in real space at much higher temperatures by NMR [19]. At present we do not offer any interpretation for this effect, but we ruled out instrument-related effects.

Similar experiments were performed using neutrons. These experiments were performed on the BT1 powder diffractometer at NIST, Gaithersburg, USA with a field up to 6 T applied perpendicular to the scattering plane. Data were collected at 3 temperatures, 60, 25, and 4.2 K, and at an energy of $E = 34.5$ meV. In Fig. 3.22 we plot the significant part of the diffraction pattern taken. At first glance, no apparent difference is revealed between the measurements with and without the field, and no magnetic order was detected. However, a closer look at the (222), and (440) peaks
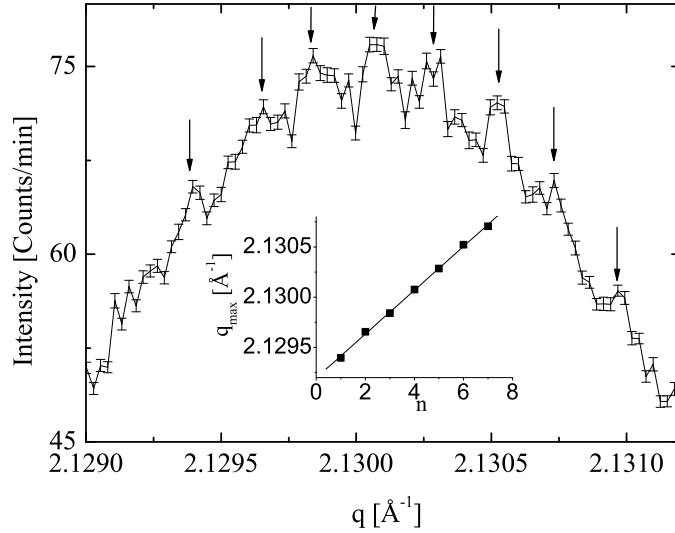
Figure 3.21: The center of the (222) Bragg peak taken at $T = 16$ K. Multiple peaks are observed and are indexed. In the inset, q_{max} versus the index n (see text).

does reveal a field dependence similar to that seen by x-rays. These field-dependent changes are qualitatively the same as seen in the x-ray experiment, but the poorer resolution of the neutron experiment are unable to demonstrate the peak changes. The strongest effect is on the (440), which has the larger structure factor in neutron diffraction. The (222) and (440) Bragg peaks are plotted in Fig. 3.24 and Fig. 3.23 respectively. At $T = 25$ K the (440) Bragg reflection grows slightly when the field is applied. We also plot in Fig .3.23 the (440) peak taken at $T = 60$ K with a baseline shift to demonstrate that the effect is strongest close to T_g and is absent at $T > T_g$. The (222) peak is plotted in Fig. 3.24. This peak only slightly broadens as a result of the field ($\Delta w = 1(2) \times 10^{-4} \text{Å}^{-1}$). This neutron experiment also proves that the effects seen are not instrumental and are related to T_g.
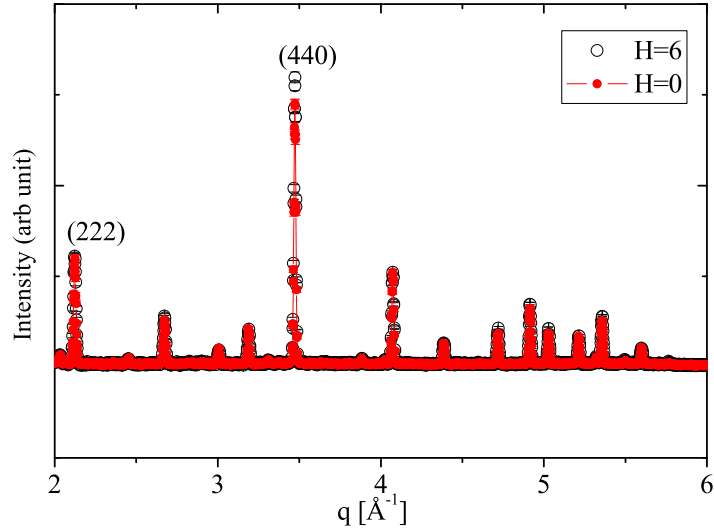
Figure 3.22: Neutron scattering from $Y_2Mo_2O_7$ with and without applied field.

Finally, the nature of the field induced distortion is further explored by NMR. We performed ^{89}Y measurements at temperatures from 300 K to 25 K. We were able to extend the temperature range of previous measurements by constructing a high pressure cell, where the sample and the NMR tank circuit are placed in an He environment pressurized to 2 Atmospheres. In such a configuration higher RF power can be delivered to the sample and the signal is stronger and can be followed to lower temperatures. At each temperature, we obtained the complete NMR spectrum by sweeping the external field, H_{ext}, at a constant applied RF frequency $f = 16.44$ MHz. In each field we used the spin-echo sequence ($\pi/2 - \pi$ pulses) and recorded the echo signal. In Fig. 3.25 and Fig.3.26 we present the NMR spectrum taken at 85 K and 25 K respectively. The width of the 85 K spectrum extends over 0.4 T whereas
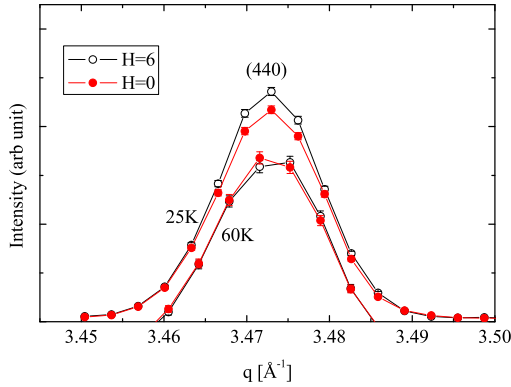
Figure 3.23: The (440) Bragg scattering with and without applied field at $T = 25$ K and $T = 60$ K. The $T = 60$ K is shifted for clarification.
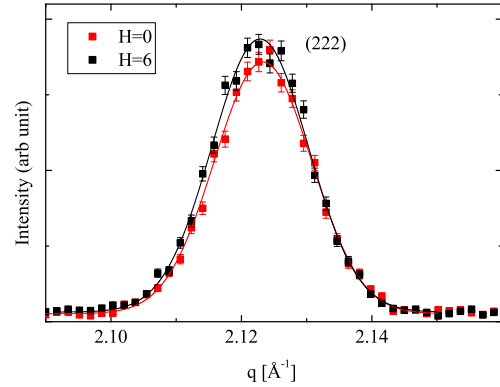
Figure 3.24: The (222) Bragg scattering with and without applied field at $T = 25$ K. The lines are fits to gaussian function.

the width of the 25 K spectrum extends over 1 T. This broadening results in low intensities at each applied field upon cooling. Due to this broad line at low T we gave up on high resolution NMR, as in Ref. [19], and concentrated on the gross features of the spectrum. The most noticeable feature in the $T = 25$ K spectrum is the clear appearance of two peaks, with a hint of a third one.

In order to study the temperature dependence of the shift, we use the powder spectrum (see §2.1.1) convoluted with Lorentzians to fit the NMR spectra. At high temperatures ($T > 250$ K) there is hardly any shift. At intermediate temperatures, $50 \leq T \leq 200$ K, two different sites were needed to fit the data (see Fig. 3.25). Finally, at low enough temperatures, $T < 50$ K, three sites were assumed (see Fig. 3.26). In Fig. 3.27 we demonstrate the contribution of each of the powder-average site to the NMR spectra. In Fig. 3.28 we plot the shift K_y^i, i for each site, versus the magnetization, which was extrapolated to $H = 7.8$ T from SQUID measurements of up to
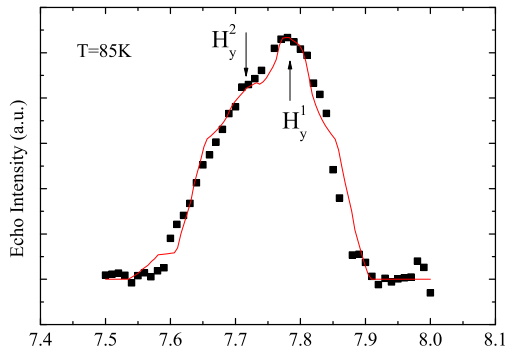
Figure 3.25: NMR spectrum at 85 K. The line is a fit to a spin 1/2 powder average convoluted with lorentzian.
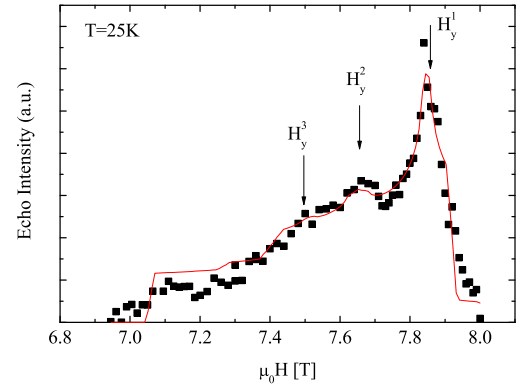
Figure 3.26: NMR spectrum at 25 K. The line is a fit to a spin 1/2 powder average convoluted with lorentzian.

6 T. The temperature in this figure is an implicit parameter. As the susceptibility increases the shift for each site also increases. However, the dependence between shift and susceptibility is not linear, indicating that the lattice contributes to the shift as discussed in Ref. [5].

Further information could be educed by comparing the shift ratios. If the three domains or phase maintain the cubic Fd$\bar{3}$m symmetry of the pyrochlore and only the unit cell size changes, we expect the ratio K_y/K_x to be identical to all domains. In Fig. 3.29 we plot the shift K_y versus the shift K_x for the three sites extracted from our fits. The K's from two sites seem to be on a straight line, thus having the same K_y versus K_x ratio. The original domain or cubic phase has a different ratio. This suggests that Fd$\bar{3}$m is not maintained in the field-enhanced domains or phases.

To conclude, we found field-dependent lattice properties in $Y_2M_2O_7$. The effect is strongest close to T_g. Had the distortion in $Y_2M_2O_7$ been a consequence of electrostatic (chemical) interactions, the magnetic field should not have had an effect on it.
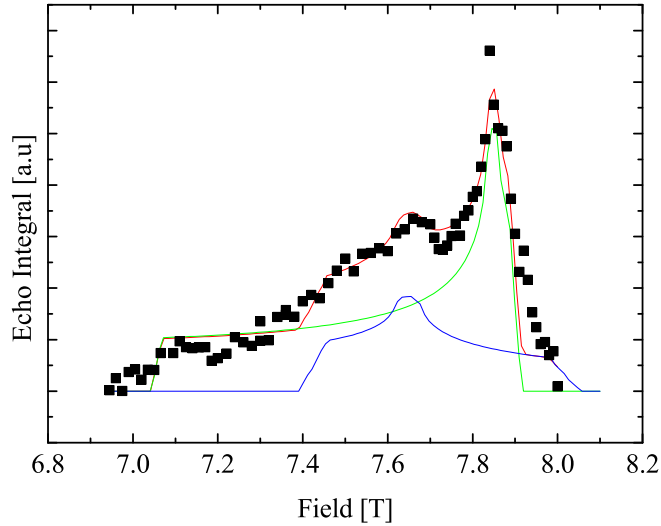
Figure 3.27: The contribution of the 2 sites to the NMR spectra

The x-ray data leave two possible scenarios for the effect of the field; (I) it is strongest when it points in the $\langle 111 \rangle$ direction and in this direction enhances the probability of three special domains, or, it generates a phase transition in part of the sample, of yet unknown nature, regardless of the field direction. The new domains or phases do not conserve the $Fd\bar{3}m$ symmetry. Regardless of the field induced structure, it seems that magnetoelastic coupling controls the freezing properties of the system.

3.2.2 $Tb_2Ti_2O_7$

The $Tb_2Ti_2O_7$ compound has received the term *cooperative paramagnet* due to its lack of a phase transition at all measured temperatures ($T > 50$ mK). Here we probe the possible existence of a magneto-elastic coupling (§1.3.1) in this compound using
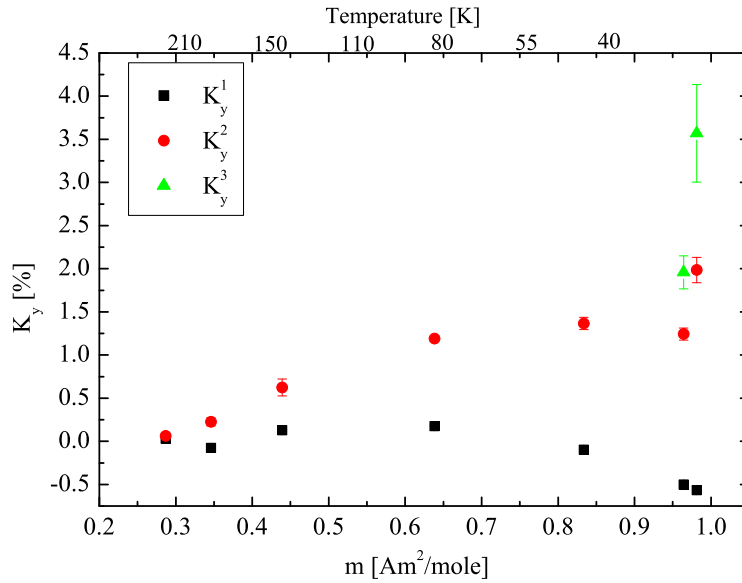
Figure 3.28: The NMR shift, K_y, versus the bulk magnetization m with temperature as an implicit parameter.

μSR (§2.1.1).

Transverse [TF] and longitudinal field [LF] μSR measurements were performed with powder samples. In Fig. 3.30 we show the LF [top] and the TF [bottom] data at two temperatures and applied field of 2kG. The TF data are shown in a reference frame rotating at a field of 1.5kG. Several aspects can be seen in the raw data: From the time scale it is clear that the transverse relaxation is by far greater than the longitudinal one. The longitudinal relaxation increases as the temperature decreases, as was observed previously [59]. Finally, the transverse relaxation increases and the muon rotation frequency decreases upon cooling.
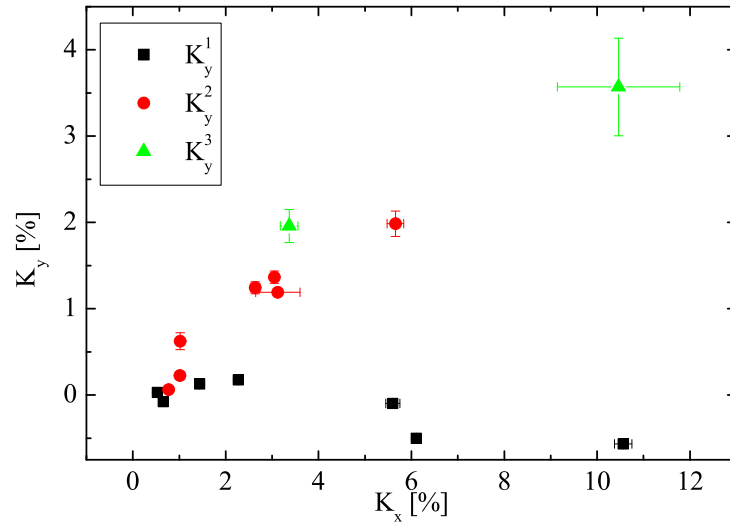
Figure 3.29: The shift K_y versus the shift K_x for the three different Y sites.

The μSR LF polarization is best described by the root exponential

$$P_{LF}(t) = A_{LF}\exp(-(t/T_1)^{\frac{1}{2}}) + B_{LF} \qquad (3.14)$$

where the parameter A_{LF} is set by taking into account the tilt of the muon spin relative to the longitudinal magnetic field, T_1 is the longitudinal relaxation time, B_{LF} is the background, and t is time. Similarly, the TF polarization is best fitted by a root exponential superimposed on a cosine oscillation

$$P_{TF}(t) = A_{TF}\exp(-(t/T_2)^{\frac{1}{2}})\cos(\omega t + \phi) + B_{TF}. \qquad (3.15)$$

Here T_2 is the transverse relaxation time. The other parameters have the same meaning as in Eq. 3.14. The quality of the fits is presented by the solid lines in Fig. 3.30.

Data were collected in the temperature range 60 mK to 100 K and three fields of 2, 4, and 6 kG. The frequency ω as a function of temperature for the three different
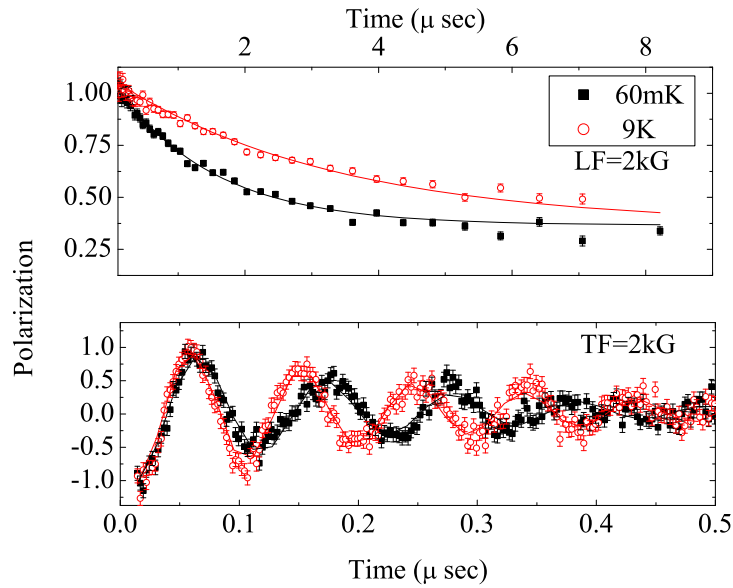
Figure 3.30: The time dependence of the muon polarization at an applied field of 2 kG and at two temperatures. In the top figure the longitudinal polarization and in the bottom, the transverse. The time scale is different between the two directions. The solid lines are fits to Eqs. 3.14 and 3.15.

fields is depicted in the inset of Fig. 3.31. The frequency shift,

$$K = (\omega_0 - \omega)/\omega_0 \qquad (3.16)$$

is shown in the main panel for the same temperatures and fields. We define ω_0 as the frequency of the free muon in the rotating reference frame. Similarly, we present T_2^{-1} in Fig. 3.32, and in the inset T_1^{-1}. The most important aspect of the data is that all quantities saturate as the temperature decreases below $\sim$2K.

Since T_1^{-1}, the LF relaxation, is an order of magnitude lower than T_2^{-1}, the TF relaxation, the contribution to the TF relaxation from dynamic fluctuations is negligible (§2.1.1). Thus, T_2^{-1} could be analyzed in terms of field inhomogeneities only.
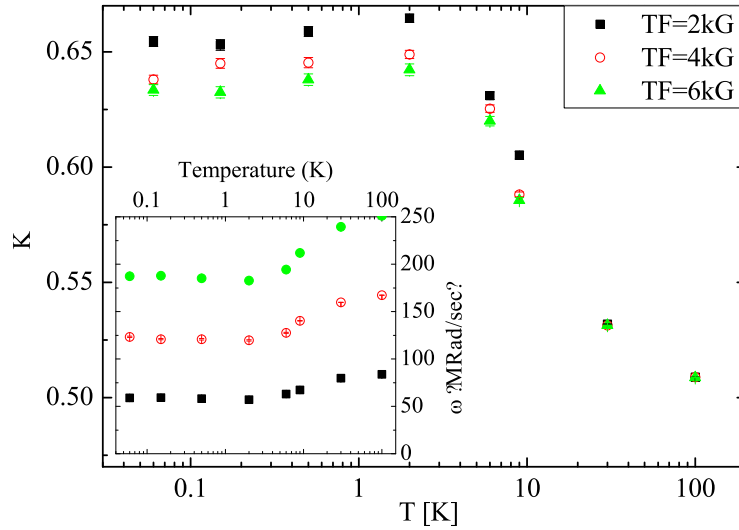
Figure 3.31: Inset: the muon rotation frequency as a function of temperature for different applied fields. Main figure: the shift in the rotation frequency defined in Eq. 3.16.

In Fig. 3.33 we show $(T_2\gamma_\mu H)^{-1}$ versus K with the temperature as an implicit parameter. The two quantities are linearly dependent at all fields. Allowing for a base line shift, which does not originate in localized spins will lead to a proportionality relation between these quantities. This stands in strong contrast to $Y_2Mo_2O_7$ where the muon transverse relaxation grows as a function of χ faster than exponentially. This is demonstrated in the inset of Fig. 3.33 using data from Ref. [5] on a semi log scale. We conclude that in $Tb_2Ti_2O_7$ the muon transverse relaxation has the same temperature dependence as the shift. In fact, by calculating the width of the distributions, δA for each data point using Eq. 2.7 we find that $\Delta(\delta A)/\overline{\delta A}$ is 15% for $Tb_2Ti_2O_7$ and 115% for $Y_2Mo_2O_7$ where $\overline{\delta A}$ and $\Delta(\delta A)$ are the average and standard
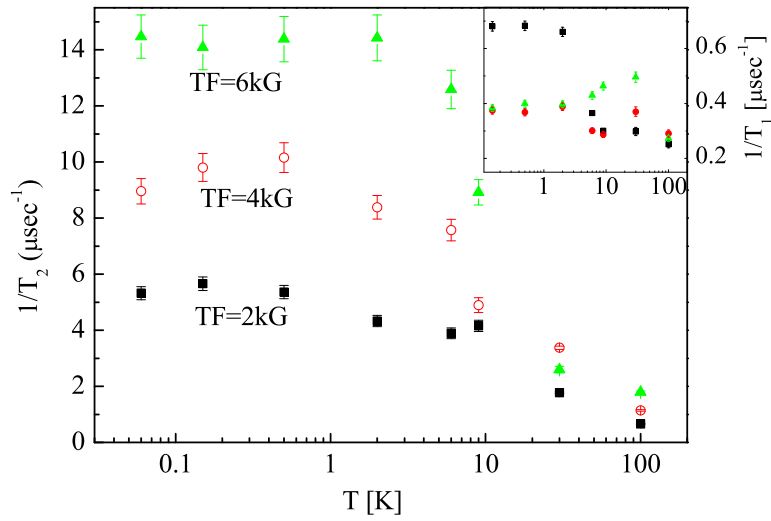
Figure 3.32: The muon spin transverse relaxation rate T_2^{-1} as a function of temperature for three different fields. Inset, the muon spin longitudinal relaxation rates T_1^{-1} at the same temperatures and fields.

deviation of δA respectively. $\Delta(\delta A)/\overline{\delta A}$ is a measure of the relative change in the distances variations due to temperature changes.

To summarize, we compare the transverse relaxation rate resulting from internal field distribution to susceptibility measured by the shift in the muon rotation frequency and DC susceptibility. We find that the relaxation rate has the same temperature dependence as the susceptibility. This indicates that the only reason for increasing relaxation upon cooling is an increase in the electronic moment size. Therefore, there is no evidence for lattice deformation in $Tb_2Ti_2O_7$ that is static on the time scale of 0.1 μsec.
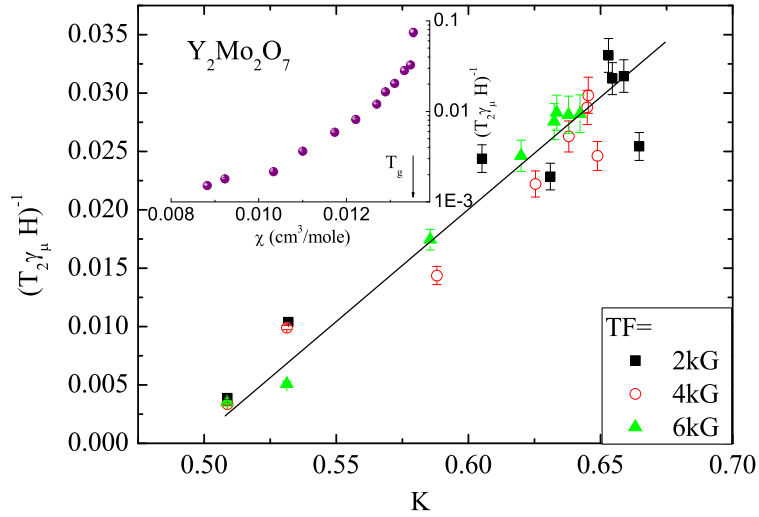
Figure 3.33: Demonstrating the linear relation between the muon spin relaxation rate normalized by the field $(T_2\gamma_\mu H)^{-1}$ versus the shift in muon spin rotation frequency K, which is proportional to the susceptibility χ. The inset shows the same type of measurement on a semi log scale in the pyrochlore compound $Y_2Mo_2O_7$ taken from Ref. [5].

3.2.3   Conclusions

Experimental evidence has been reviewed on two pyrochlore samples, $Y_2Mo_2O_7$ and $Tb_2Ti_2O_7$. [89]Y NMR performed on the Y nuclei, hints to a distortion of the lattice. This finding did not receive confirmation from x-rays or neutron scattering techniques. This discrepancy is not clear to us at present.

μSR on $Tb_2Ti_2O_7$ did not detect any lattice distortion. It might be that since $Tb_2Ti_2O_7$ does not undergo any phase transition, it doesn't deforms, and vice versa.

3.3 Discussion

To summarize, we seen that geometrically frustrated magnets are ideal to explore perturbations beyond the Heisenberg model.

We demonstrated that exchange anisotropies is a relevant perturbation in the kagome herbertsmithite and contributes to its ground-state properties. Others have argued that DMI is also important especially at low T. Most likely for full understanding of the herbertsmithite low-T behavior both perturbation should be taken into account. In the pyrochlore $Y_2Mo_2O_7$ the lattice distortion observed by resonance techniques can be attributed to a magneto-elastic coupling. $Tb_2Ti_2O_7$, seems to be a pure Heisenberg antiferromagnet without magnetoelastic coupling.

Appendix A

Powder Average

In this appendix we derive the powder average NMR spectrum. We start with the Hamiltonian of a spin-1/2 system, with a Knight-Shift tensor $\mathbf{K}$,

$$\mathcal{H} = -\hbar\gamma H_l \mathbf{I} \cdot (\bar{\mathbf{1}} + \bar{\mathbf{K}}) \cdot \hat{\mathbf{H}}_l. \tag{A.1}$$

Our aim is to find the energy (or the resonance frequency), $e = h\nu$. This frequency should be a function of the external field, $H = H(\theta, \varphi)$ and $\mathbf{K}$, thus $\nu = \nu(H, \theta, \varphi, \mathbf{K})$. For a polycrystalline samples the sites are oriented randomly with respect to the field therefore we would like to integrate over all possible orientations.

We use Eq. A.1 and write explicitly,

$$\mathcal{H} = \begin{bmatrix} I_x & I_y & I_z \end{bmatrix} \cdot \begin{bmatrix} 1+K_x & 0 & 0 \\ 0 & 1+K_y & 0 \\ 0 & 0 & 1+K_z \end{bmatrix} \cdot H_l \begin{bmatrix} \sin\theta\cos\varphi \\ \sin\theta\sin\varphi \\ \cos\theta \end{bmatrix}$$

$$= -\hbar\gamma H_l \left[I_x(1+K_x)\sin\theta\cos\varphi + I_y(1+K_y)\sin\theta\sin\varphi + I_z(1+K_z)\cos\theta \right] \tag{A.2}$$

by using the pauli matrices for $\mathbf{I}$,

$$\mathcal{H} = -\hbar\gamma H_l$$

$$\cdot \begin{bmatrix} (1+K_z)\cos\theta & (1+K_x)\sin\theta\cos\varphi - i(1+K_y)\sin\theta\sin\varphi \\ (1+K_x)\sin\theta\cos\varphi + i(1+K_y)\sin\theta\sin\varphi & -(1+K_z)\cos\theta \end{bmatrix} \cdot$$

$$(A.3)$$

The eigenvalues for Eq. A.3,

$$\frac{e_1}{\hbar\gamma H_l} = (1 + 2K_y\sin^2\varphi\sin^2\theta + K_y^2\sin^2\varphi\sin^2\theta$$

$$- K_x^2\sin^2\varphi\sin^2\theta - 2K_x\sin^2\varphi\sin^2\theta + 2K_x\sin^2\theta \tag{A.4}$$

$$+ K_x^2\sin^2\theta + K_z^2 - 2K_z\sin^2\theta + 2K_z - K_z^2\sin^2\theta)^{1/2}$$

$$e_2 = -e_1 \tag{A.5}$$

Small Knighshift

We assume small K_i ($K_{x,y,z}^2 \to 0$), and use $\sqrt{1+\alpha} \simeq 1 + \frac{\alpha}{2}$, thus Eq .A.4,

$$\frac{e_1}{\hbar\gamma H_l} = 1 + K_x\sin^2\theta\cos^2\varphi + K_y\sin^2\theta\sin^2\varphi + K_z\cos^2\theta . \tag{A.6}$$

The energy difference between the two states is therefore, $h\nu = 2e_1$. Using trigonometric identities

$$\frac{h\nu}{\hbar\gamma H_l} = K_z\cos^2\theta + \frac{1}{2}K_x\sin^2\theta\left(1 - \cos 2\varphi\right) + \frac{1}{2}K_y\sin^2\theta\left(\cos 2\varphi + 1\right)$$

$$= \frac{1}{3}\left(K_x + K_y + K_z\right) + \frac{1}{6}\left(2K_z - K_x - K_y\right)\left(3\cos^2\theta - 1\right) + \tag{A.7}$$

$$+ \frac{1}{2}\left(K_y - K_x\right)\left(1 - \cos^2\theta\right)\cos 2\varphi$$

or,

$$\nu_{per}(\mathbf{K}, H_l, \mu, \varphi) = \nu_l\left[K_{\text{iso}} + K_{\text{ax}}(3\mu^2 - 1) + K_{\text{aniso}}(1 - \mu^2)\cos 2\varphi\right]$$

where $\nu_l = H_l \gamma / (2\pi)$, and

$$K_{\text{iso}} = (K_x + K_y + K_z)/3 \tag{A.8}$$

$$K_{\text{ax}} = (2K_z - K_x - K_y)/6$$

$$K_{\text{aniso}} = (K_y - K_x)/2 \ .$$

Axially symmetry

We begin with the eigenvalues for the Hamiltonian A.1, found earlier as Eq. A.4. We assume axially symmetry only, $K_x = K_y$, and gain,

$$\frac{e_1}{\hbar \gamma H_l} = (1 + 2K_y \sin^2 \theta + K_y^2 \sin^2 \theta + K_z^2 - 2K_z \sin^2 \theta + 2K_z - K_z^2 \sin^2 \theta)^{1/2} \tag{A.9}$$

with $\mu = cos\theta$, now the energy difference,

$$\hbar \gamma H_l = \frac{h\nu}{\sqrt{1 + K_y^2 \left(1 - \mu^2\right) + 2K_y \left(1 - \mu^2\right) + 2K_z \mu^2 + K_z^2 \mu^2}} \tag{A.10}$$

such that the resonance field obeys,

$$H_l = \frac{h\nu}{\beta} \frac{1}{\sqrt{1 + 2K_\perp + K_\perp^2 - \mu^2 K_\perp^2 + 2\mu^2 K_\parallel - 2\mu^2 K_\perp + \mu^2 K_\parallel^2}} \tag{A.11}$$

$$= \frac{h\nu}{\beta} \frac{1}{\sqrt{g_\perp^2 - \mu^2 \left(g_\perp^2 - g_\parallel^2\right)}} = \frac{h\nu}{g\beta} \tag{A.12}$$

where we define,

$$\beta = -\hbar \gamma \tag{A.13}$$

$$K_\perp = K_x = K_y \tag{A.14}$$

$$K_z = K_\parallel \tag{A.15}$$

$$\mathbf{g} = 1 + \mathbf{K} \tag{A.16}$$

$$g = \sqrt{g_\perp^2 - (g_\perp^2 - g_\parallel^2)\mu^2} \ . \tag{A.17}$$

The powder pattern, $S(H)$,

$$S(H) = \frac{1}{2}\left(\frac{dH}{d\mu}\right)^{-1}. \tag{A.18}$$

Using $H = H_l(\mu)$ of Eq.A.12,

$$\frac{dH_l}{d\mu} = \frac{h\nu}{2\beta}\frac{2\mu\left(g_\perp^2 - g_\parallel^2\right)}{\left[g_\perp^2 - \mu^2\left(g_\perp^2 - g_\parallel^2\right)\right]^{3/2}} \tag{A.19}$$

thus,

$$S(H) = \frac{1}{2}\frac{\beta}{h\nu}\frac{\left[g_\perp^2 - \mu^2\left(g_\perp^2 - g_\parallel^2\right)\right]^{3/2}}{\mu\left(g_\perp^2 - g_\parallel^2\right)} \tag{A.20}$$

recalling, $\mu^2\left(g_\perp^2 - g_\parallel^2\right) = g_\perp^2 - \left(\frac{h\nu}{H\beta}\right)^2$, we get,

$$S = \frac{1}{2}\frac{\beta}{h\nu}\frac{\left[g_\perp^2 - \mu^2\left(g_\perp^2 - g_\parallel^2\right)\right]^{3/2}}{\sqrt{\frac{g_\perp^2 - \left(\frac{h\nu}{\beta H}\right)^2}{g_\perp^2 - g_\parallel^2}}\left(g_\perp^2 - g_\parallel^2\right)} \tag{A.21}$$

$$= \frac{1}{2}\frac{\beta}{h\nu}\frac{\left[g_\perp^2 - \mu^2\left(g_\perp^2 - g_\parallel^2\right)\right]^{3/2}}{g_\perp\sqrt{g_\perp^2 - g_\parallel^2}\sqrt{1 - \frac{1}{H^2}\left(\frac{h\nu}{g_\perp\beta}\right)^2}} \tag{A.22}$$

we've seen that, $g = \frac{h\nu}{\beta H}$ (Eq. A.12), hence,

$$S = \frac{1}{2}\frac{\beta}{h\nu}\left(\frac{h\nu}{\beta H}\right)^3\frac{1}{g_\perp\sqrt{g_\perp^2 - g_\parallel^2}\sqrt{1 - \frac{1}{H^2}\left(\frac{h\nu}{g_\perp\beta}\right)^2}}$$

$$= \frac{1}{2}\frac{(h\nu)^2}{\beta^2 g_\perp\sqrt{g_\perp^2 - g_\parallel^2}H^2\sqrt{H^2 - \left(\frac{h\nu}{g_\perp\beta}\right)^2}} \tag{A.23}$$

for

$$\frac{h\nu}{g_\perp\beta} \leq H \leq \frac{h\nu}{g_\parallel\beta}$$

and $S(H) = 0$ elsewhere. In Fig. A.1 we plot the expected NMR spectra for a sample with axial symmetry.
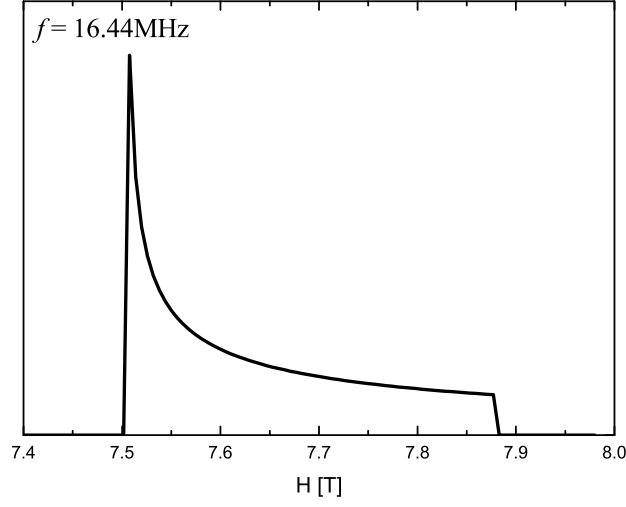
Figure A.1: The theoretical axial symmetric NMR spectrum.

Complete Anisotropy

Here we develop the NMR spectra for a completely anisotropic sample, $K_x \neq K_y \neq K_z$. We once again use the eigenvalue we found in the general case, Eq. A.4,

$$\left(\frac{e_1}{\beta H}\right)^2 = 1 + \sin^2 \varphi \left(1 - \mu^2\right) \left(2K_y + K_y^2 - K_x^2 - 2K_x\right) +$$

$$+ \left(1 - \mu^2\right) \left(2K_x + K_x^2 - 2K_z - K_z^2\right) + K_z^2 + 2K_z \tag{A.24}$$

$$= g_2^2 - \cos^2 \varphi \left(1 - \mu^2\right) \left(g_2^2 - g_1^2\right) - \mu^2 \left(g_1^2 - g_3^2\right) . \tag{A.25}$$

This leads the resonance field to be,

$$H = \frac{h\nu}{\beta} \frac{1}{\sqrt{g_2^2 - \cos^2 \varphi \left(1 - \mu^2\right) \left(g_2^2 - g_1^2\right) - \mu^2 \left(g_1^2 - g_3^2\right)}} \tag{A.26}$$

thus,

$$\frac{dH}{d\mu} = \frac{h\nu}{\beta} \frac{\mu \left[\left(g_1^2 - g_3^2\right) - \cos^2 \varphi \left(g_2^2 - g_1^2\right)\right]}{\left[g_2^2 - \cos^2 \varphi \left(1 - \mu^2\right) \left(g_2^2 - g_1^2\right) - \mu^2 \left(g_1^2 - g_3^2\right)\right]^{3/2}}$$

from the resonance field equation, Eq.A.25 we find $\mu = \mu(H)$,

$$
\left(\frac{h\nu}{\beta H}\right)^2 = g_2^2 - \cos^2\varphi\left(g_2^2 - g_1^2\right) + \mu^2\left(\cos^2\varphi\left(g_2^2 - g_1^2\right) - g_1^2 + g_3^2\right)
$$

$$
\Downarrow
$$

$$
\mu^2 = \frac{\left(\frac{h\nu}{\beta H}\right)^2 - g_2^2 + \cos^2\varphi\left(g_2^2 - g_1^2\right)}{\cos^2\varphi\left(g_2^2 - g_1^2\right) - g_1^2 + g_3^2} \tag{A.27}
$$

therefore,

$$
\begin{aligned}
\frac{dH}{d\mu} &= \frac{h\nu}{\beta}\frac{\sqrt{g_2^2 - \cos^2\varphi\left(g_2^2 - g_1^2\right) - \left(\frac{h\nu}{\beta H}\right)^2}\sqrt{g_1^2 - g_3^2 - \cos^2\varphi\left(g_2^2 - g_1^2\right)}}{\left[g_2^2 - \cos^2\varphi\left(g_2^2 - g_1^2\right) + \left(\frac{h\nu}{\beta H}\right)^2 - g_2^2 + \cos^2\varphi\left(g_2^2 - g_1^2\right)\right]^{3/2}} \\
&= H^3\sqrt{\frac{H^2 - H_2^2}{H^2 H_2^2} - \cos^2\varphi\frac{H_1^2 - H_2^2}{H_1^2 H_2^2}}\sqrt{\frac{H_3^2 - H_1^2}{H_3^2 H_1^2} - \cos^2\varphi\frac{H_1^2 - H_2^2}{H_1^2 H_2^2}} \tag{A.28}
\end{aligned}
$$

where we define,

$$
H_i \equiv \frac{h\nu}{g_i\beta}, i = 1,2,3
$$

The powder pattern should be ($S(H) = \rho(H)$ mentioned above),

$$
\begin{aligned}
S(H) &= \int\int \delta\left(\nu_{app} - \nu\left(H,\mu,\varphi\right)\right) d\mu d\varphi \\
&= \int d\varphi \int d\mu \delta\left(\nu_{app} - \nu\left(H,\mu,\varphi\right)\right) \tag{A.29}
\end{aligned}
$$

where, $\nu(H,\mu,\varphi)$ is derived from A.26. Since $\nu = \nu(H,\mu,\varphi)$ we can change integrands, to simplify our equation,

$$
d\nu = \frac{d\nu}{d\mu}d\mu \tag{A.30}
$$

and get,

$$
\begin{aligned}
S(H) &= \int d\varphi \int \frac{d\nu}{\frac{d\nu}{d\mu}}\delta\left(\nu_{app} - \nu\left(H,\mu,\varphi\right)\right) \\
&= \int d\varphi \int d\nu \left(\frac{d\mu}{d\nu}\right)\delta\left(\nu_{app} - \nu\left(H,\mu,\varphi\right)\right) \tag{A.31}
\end{aligned}
$$

because of the δ-function this reduces to,

$$S(H) = \int d\varphi \left(\frac{d\mu}{d\nu} \right)_{\nu=\nu_{app}} \tag{A.32}$$

hence, the powder pattern in this case (after some work) evaluates to,

$$S(H) = \frac{1}{2} \left(\frac{dH}{d\mu} \right)^{-1}$$

$$= \frac{1}{2H^2} \frac{H_1 H_2 H_3}{\sqrt{(H^2 - H_1^2)}\sqrt{(H_3^2 - H_2^2)}} \frac{1}{\sqrt{1 - \frac{(H_2^2 - H_1^2)H^2}{H_2^2(H^2 - H_1^2)} \sin^2 \varphi} \sqrt{1 - \frac{(H_2^2 - H_1^2)H_3^2}{H_1^2(H_3^2 - H_2^2)} \sin^2 \varphi}} \tag{A.33}$$

using the definition for elliptic integrals of the first kind,

$$K(k) = \int_0^{\frac{\pi}{2}} \frac{d\theta}{\sqrt{1 - k^2 \sin^2 \theta}} \tag{A.34}$$

with $0 \leq k \leq 1$, being the *elliptic modulus*, a.k.a. $m = k^2$ *the parameter*. The integral is symmetric, $\int_0^\pi = 2 \int_0^{\frac{\pi}{2}}$, hence we get a multiplicity of 2.

By defining, $t = \sin \theta$, thus, $dt = \cos \theta d\theta = \sqrt{1 - t^2} d\theta$ we get,

$$K(k) = \int \frac{dt}{\sqrt{1 - t^2}\sqrt{1 - k^2 t^2}} \tag{A.35}$$

After tedious work, it is possible to show that Eq.A.33 has indeed a Legendre elliptic integral form[60]. A theoretical powder averaged NMR line, for a single site, is depicted in Fig. A.2. Each divergence in the spectrum is related to a different K. The field with the lowest divergence is related to K_x, the middle is related to K_y and the highest field is related to K_z. This theoretical spectrum demonstrates that a single site, with a single set of K_x, K_y, K_z, could give rise to only one NMR line peak even under powder averaging.
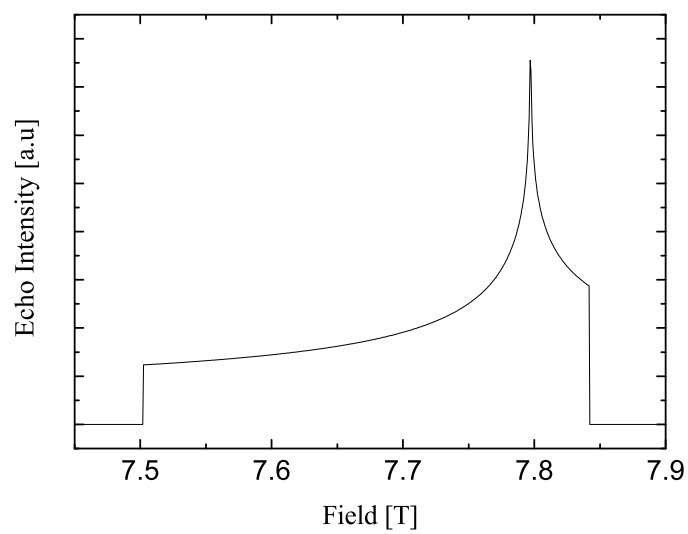
Figure A.2: A theoretical powder-averaged NMR for a spin-1/2, $\gamma = 2.11\text{MHz/T}$, $\nu = 16.44\text{MHz}$.

Appendix B

DMI

Taking into account a weak spin-orbit coupling ($\lambda\mathbf{L} \cdot \mathbf{S}$) and expanding in powers of λ, Moriya showed that the effective magnetic hamiltonian between neighboring spins can represented in the Hamiltonian as,

$$\mathcal{H}_{DM} = \sum_{<i,j>} \mathbf{D}_{ij} \cdot (\mathbf{S}_i \times \mathbf{S}_j) \tag{B.1}$$

where $\mathbf{D}_{ij} \ll J_{ij}$ is the DM vector which defines the interaction ($J \propto \lambda^0$ whereas $D \propto \lambda$). The interaction changes sign if we permute spins j and i (the interaction is antisymmetric), that is, $\mathbf{D}_{ij} = -\mathbf{D}_{ji}$. The interaction described in Eq. B.1 is such that $\mathbf{D}$ is perpendicular to the plane created by $\mathbf{S}_i$ and $\mathbf{S}_j$. In Fig. B.1 and Fig. B.2 we demonstrate the type of order induced by DMI alone (Fig. B.1) and in a more realistic case with a perturbation to the Heisenberg Antiferromagnetic coupling (Fig. B.2).

$\mathbf{D}$ was shown, by Moriya, to be proportional to $\lambda t_{ij}/(\Delta U)$, where Δ is the crystal field splitting and λ is the spin-orbit coupling. [The exchange $J_{ij} = 4t_{ij}/U$ where U is the coulomb repulsion, t_{ij} the intersite hopping]. DMI stems from the spin-orbit couplings. The DM term in the Hamiltonian causes the susceptibility to change by inducing a moment by canting the spins slightly out of the plane, and may give each
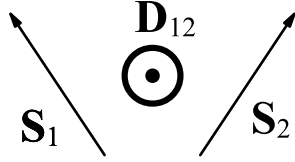
Figure B.1: A typical DMI,
$\mathbf{D}_{12} \cdot (\mathbf{S}_1 \times \mathbf{S}_2)$.
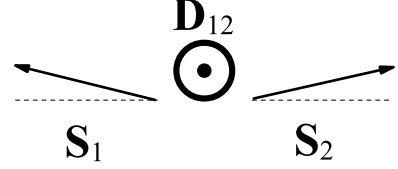
Figure B.2: The type of disorder from DMI in Heisenberg AF coupling, $J \neq 0$. The DMI causes a canting of the spins from an ideal anti-parallel state.

kagomé plane a net ferromagnetic moment. As a consequence of the Hamiltonian being invariant under the symmetry operations which leave the lattice invariant, the direction of $\mathbf{D}_{ij}$ is geometrically constrained and follows rules set by Moriya. The rules are for any general crystal, we observe two ions in the system, 1 and 2, which are located at A and B, respectively. The point bisecting the line AB is defined as C.

1. When a center of inversion is located at C, $\mathbf{D} = 0$.

2. When a mirror plane perpendicular to AB passes through C, $\mathbf{D} \parallel$ mirror plane or $\mathbf{D} \perp$AB.

3. When there is a mirror plane including A and B, $\mathbf{D} \perp$mirror plane.

4. When a two-fold rotation axis perpendicular to AB passes through C, $\mathbf{D} \perp$two-fold axis.

5. When there is an n-fold axis $(n \geq 2)$ along AB, $\mathbf{D} \parallel$AB.
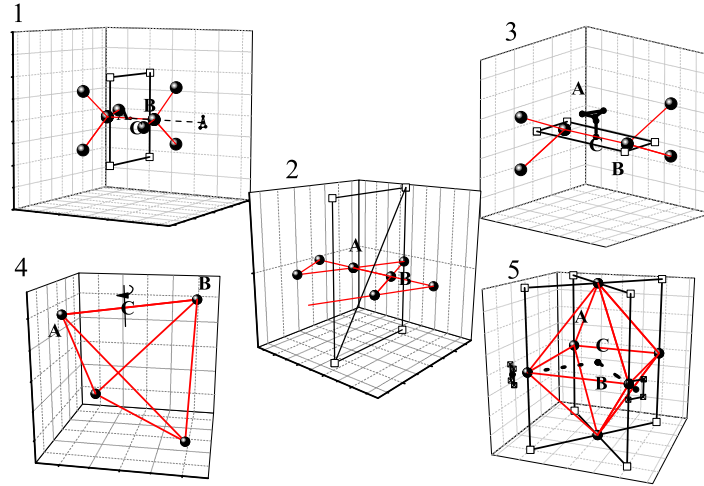
Figure B.3: Examples of DMI rules. Numbers indicate rule number as explained in the text. Sites are shown in circles connected by red lines, mirror planes are indicated in hollow boxes connected by black line.

In Fig. B.3 we demonstrate the rules graphically, the numbers indicate the rule number which the figure is relevant to (in Fig. B.3.5 a four-fold rotation, $n = 4$, is shown).

For the kagomé plane, two of the Moriya's rules give useful information about $\mathbf{D}_{ij}$. Since the middle point between two sites in the triangle of the kagomé is not a center of inversion, $\mathbf{D} \neq 0$ is possible. In a perfect kagomé lattice, $\mathbf{D}_{ij}$ can only be perpendicular to the kagomé plane since this plane is a mirror plane. Most materials however are not perfect kagomé lattices or the surrounding ions affects the crystal field and are involved in the superexchange mechanism between the magnetic sites.

Since the pyrochlore lattice does not have an inversion center at the middle point between sites, $D \neq 0$, and a DMI can occur on the pyrochlore. Considering a single

tetrahedron, the plane which connects two sites and the middle point of the opposite bond in the tetrahedron is a mirror plane. Thus $\mathbf{D}$ can only be perpendicular to this plane. There are thus two possible DMI's between two sites which correspond to the directions for the $\mathbf{D}$ vector.

By taking a mean field approach, we write the heisenberg hamiltonian with DMI as,

$$\mathcal{H} = -\sum_i \mathbf{S}_i \cdot \left(J \sum_{j \neq i} \mathbf{S}_j + \mathbf{D}_{ij} \times \mathbf{S}_j + g\mu_B H \right) \tag{B.2}$$

we've used the vector relation, $\mathbf{A} \cdot (\mathbf{B} \times \mathbf{C}) = \mathbf{B} \cdot (\mathbf{C} \times \mathbf{A})$. this hamiltonian can be written as $\mathcal{H} = -g\mu_B \sum_i \mathbf{S}_i \cdot \mathbf{H}^{eff}$, where the effective field,

$$\mathbf{H}^{eff} = \frac{1}{g\mu_B} \sum_j \left(J\mathbf{S}_j + \mathbf{D}_{ij} \times \mathbf{S}_j \right) + H \tag{B.3}$$

we apply $\mathbf{S}_j \to \mathbf{M}/g\mu_B$ thus gain,

$$\mathbf{H}^{eff} = \frac{Z}{(g\mu_B)^2} \left(J\mathbf{M} + \mathbf{D} \times \mathbf{M} \right) + H \tag{B.4}$$

thus the magnetization,

$$\mathbf{M} = \frac{C}{T} \left(\frac{Z}{(g\mu_B)^2} \left(J\mathbf{M} + \mathbf{D} \times \mathbf{M} \right) + H \right). \tag{B.5}$$

where $C = (g\mu_B)^2 S(S+1)/(3k_B)$ is the currie constant. Eq. B.5 can be written as,

$$\mathbf{M} = \left(\frac{T}{Z}(g\mu_B)^2 - C\mathbf{A} \right)^{-1} \frac{C(g\mu_B)^2}{Z} H \tag{B.6}$$

where $\mathbf{A} = \mathbf{A}(J, \mathbf{D})$ is given by,

$$\mathbf{A} = \frac{Z}{(g\mu_B)^2} \begin{pmatrix} J & -D_z & D_y \\ D_z & J & -D_x \\ -D_y & D_x & J \end{pmatrix}. \tag{B.7}$$

The inverse susceptibility, $\chi_z^{-1} = H_z/\mathbf{M}_{3,3}$ and $\chi_\perp^{-1} = H_\perp/\mathbf{M}_{1,1}$,

$$\chi_z^{-1} = \frac{(T + \theta_{CW})^3 + \left(\frac{\theta_{CW}}{J}\right)^2 (T + \theta_{CW}) |D|^2}{C\left((T + \theta_{CW})^2 + \left(\frac{\theta_{CW}}{J}\right)^2 D_z^2\right)} \tag{B.8}$$

$$\chi_\perp^{-1} = \frac{(T + \theta_{CW})^3 + \left(\frac{\theta_{CW}}{J}\right)^2 (T + \theta_{CW}) |D|^2}{C\left((T + \theta_{CW})^2 + \left(\frac{\theta_{CW}}{J}\right)^2 D_\perp^2\right)} \ . \tag{B.9}$$

The asymptotic expansion of Eq. B.8 in D (with $x = T + \theta_{CW}$) reveals,

$$\chi_z^{-1} \approx \frac{x}{C} + \frac{1}{C}\left(\frac{\theta_{CW}}{J}\right)^2 \left(|D|^2 - D_z^2\right)\frac{1}{x} - \frac{1}{C}\left(\frac{\theta_{CW}}{J}\right)^4 D_z^2 \left(D_x^2 + D_y^2\right)\frac{1}{x^3}$$
$$+ \frac{1}{C}\left(\frac{\theta_{CW}}{J}\right)^6 D_z^4 \left(D_x^2 + D_y^2\right)\frac{1}{x^5} + O\left(\frac{1}{x^7}\right) \tag{B.10}$$

i.e., in a mean-field macroscopic approximation the DMI does not change the Currie-Wiess constant, θ_{CW}.

References

[1] A. Olariu, P. Mendels, F. Bert, F. Duc, J. C. Trombe, M. A. de Vries, and A. Harrison, *Physical Review Letters* **100**, 087202 (2008).

[2] T. Imai, E. A. Nytko, B. M. Bartlett, M. P. Shores, and D. G. Nocera, *Physical Review Letters* **100**, 077203 (2008).

[3] A. Olariu, *PhD Thesis*, Universite de Paris-Sud, 2007.

[4] S. Tanaka and S. Miyashita, *J. Phys.: Condens. Matter* **19**, 145256 (2007).

[5] E. Sagi, O. Ofer, A. Keren, and J. S. Gardner, *Physical Review Letters* **94**, 237202 (2005).

[6] K. Kano and S. Naya, *Prog. Theor. Phys.* **10**, 158 (1953).

[7] P. Lecheminant, B. Bernu, C. Lhuillier, L. Pierre, and P. Sindzingre, *Phys. Rev. B* **56**, 2521 (1997).

[8] F. Mila, *Phys. Rev. Lett.* **81**, 2356 (1998).

[9] J. von Delft and C. L. Henley, *Phys. Rev. B* **48**, 965 (1993).

[10] R. Moessner and J. T. Chalker, *Phys. Rev. Lett.* **80**, 2929 (1998).

[11] A. Chubukov, *Phys. Rev. Lett.* **69**, 832 (1992).

[12] J. Villain, *Z. Phys. B* **33**, 31 (1979).

[13] M. D. Núñez Regueiro, C. Lacroix, and B. Canals, *Phys. Rev. B* **54**, R736 (1996).

[14] S. E. Palmer and J. T. Chalker, *Phys. Rev. B* **62**, 488 (2000).

[15] O. Tchernyshyov, R. Moessner, and S. L. Sondhi, *Phys. Rev. B* **66**, 064403 (2002).

[16] D. L. Bergman, R. Shindou, G. A. Fiete, and L. Balents, *Physical Review B (Condensed Matter and Materials Physics)* **74**, 134409 (2006).

[17] S.-H. Lee, C. Broholm, T. H. Kim, W. Ratcliff, and S.-W. Cheong, *Phys. Rev. Lett.* **84**, 3718 (2000).

[18] J.-H. Chung, M. Matsuda, S.-H. Lee, K. Kakurai, H. Ueda, T. J. Sato, H. Takagi, K.-P. Hong, and S. Park, *Physical Review Letters* **95**, 247204 (2005).

[19] A. Keren and J. S. Gardner, *Phys. Rev. Lett.* **87**, 177201 (2001).

[20] C. H. Booth, J. S. Gardner, G. H. Kwei, R. H. Heffner, F. Bridges, and M. A. Subramanian, *Phys. Rev. B* **62**, R755 (2000).

[21] M. Rigol and R. R. P. Singh, *Physical Review Letters* **98**, 207204 (2007).

[22] M. Rigol and R. R. P. Singh, *Physical Review B (Condensed Matter and Materials Physics)* **76**, 184403 (2007).

[23] M. Elhajal, B. Canals, and C. Lacroix, *Phys. Rev. B* **66**, 014422 (2002).

[24] M. Elhajal, B. Canals, R. Sunyer, and C. Lacroix, *Physical Review B (Condensed Matter and Materials Physics)* **71**, 094420 (2005).

[25] D. Grohol, K. Matan, J.-H. Cho, S.-H. Lee, J. W. Lynn, D. G. Nocera, and Y. S. Lee, *Nature Materials* **4**, 323 (2005).

[26] E. A. Nytko, *PhD Thesis*, Massachusetts Institute of Technology (MIT), 2008.

[27] M. P. Shores, E. A. Nytko, B. M. Bartlett, and D. G. Nocera, *J. Am. Chem. Soc.* **127**, 13462 (2005).

[28] R. K. Wangsness, *The Journal of Chemical Physics* **20**, 1656 (1952).

[29] T. Nakamura and S. Miyashita, *Phys. Rev. B* **52**, 9174 (1995).

[30] A. Zorko, S. Nellutla, J. van Tol, L. C. Brunel, F. Bert, F. Duc, J. C. Trombe, M. A. de Vries, A. Harrison, and P. Mendels, *cond-mat/0804.3107* (2008).

[31] P. Sindzingre, *cond-mat/0707.4264* (2007).

[32] C.-H. Chern and M. Tsukamoto, *cond-mat/0710.1334* (2007).

[33] F. Bert, S. Nakamae, F. Ladieu, D. L'Hôte, P. Bonville, F. Duc, J.-C. Trombe, and P. Mendels, *Physical Review B (Condensed Matter and Materials Physics)* **76**, 132411 (2007).

[34] G. Misguich and P. Sindzingre, *Eur. Phys. J. B* **59**, 305 (2007).

[35] M. Vries, K.V.Kamenev, W.A.Kockelmann, J.Sanchez-Benitez, and A.Harrison, *cond-mat/0705.0654* (2007).

[36] S.-H. Lee, H. Kikuchi, Y. Qiu, B. Lake, Q. Huang, K. Habicht, and K. Kiefer, *Nature Materials* **6**, 853 (2007).

[37] J. S. Helton, K. Matan, M. P. Shores, E. A. Nytko, B. M. Bartlett, Y. Yoshida, Y. Takano, A. Suslov, Y. Qiu, J.-H. Chung, D. G. Nocera, and Y. S. Lee, *Physical Review Letters* **98**, 107204 (2007).

[38] O. Ofer, A. Keren, E. A. Nytko, M. P. Shores, B. M. Bartlett, D. G. Nocera, C. Baines, and A. Amato, *cond-mat/0610540* (2007).

[39] M. J. P. Gingras, C. V. Stager, N. P. Raju, B. D. Gaulin, and J. E. Greedan, *Phys. Rev. Lett.* **78**, 947 (1997).

[40] N. P. Raju, E. Gmelin, and R. K. Kremer, *Phys. Rev. B* **46**, 5405 (1992).

[41] J. S. Gardner, S. R. Dunsiger, B. D. Gaulin, M. J. P. Gingras, J. E. Greedan, R. F. Kiefl, M. D. Lumsden, W. A. MacFarlane, N. P. Raju, J. E. Sonier, I. Swainson, and Z. Tun, *Phys. Rev. Lett.* **82**, 1012 (1999).

[42] N. Hamaguchi, T. Matsushita, N. Wada, Y. Yasui, and M. Sato, *Phys. Rev. B* **69**, 132413 (2004).

[43] I. Mirebeau, P. Goncharenko, Cadavez-Peres, S. Bramwell, M. Gingras, and J. Gardner, *Nature* **420**, 54 (2002).

[44] K. C. Rule, J. P. C. Ruff, B. D. Gaulin, S. R. Dunsiger, J. S. Gardner, J. P. Clancy, M. J. Lewis, H. A. Dabkowska, I. Mirebeau, P. Manuel, Y. Qiu, and J. R. D. Copley, *Physical Review Letters* **96**, 177201 (2006).

[45] I. Mirebeau, I. N. Goncharenko, G. Dhalenne, and A. Revcolevschi, *Phys. Rev. Lett.* **93**, 187204 (2004).

[46] E. Sagi, *MSc Thesis*, Technion, 2005.

[47] M. Abramowitz and I. A. Stegun, *Handbook of Mathematical Functions with Formulas, Graphs, and Mathematical Tables*, Dover, New York, ninth dover printing, tenth gpo printing edition, 1964.

[48] F. Gozzo, B. Schmitt, T. Bortolamedi, C. Giannini, A. Guagliardi, M. Lange, D. Meister, D. Madena, P. Willmott, and B. Patterson, *J. Alloys and Compounds* , 206 (2004).

[49] P. Mendels, F. Bert, M. A. de Vries, A. Olariu, A. Harrison, F. Duc, J. C. Trombe, J. S. Lord, A. Amato, and C. Baines, *Physical Review Letters* **98**, 077204 (2007).

[50] O. Ofer, A. Keren, C. Baines, and J. S. Gardner, *J.Phys.: Condens. Matter* .

[51] A. Keren, Y. J. Uemura, G. Luke, P. Mendels, M. Mekata, and T. Asano, *Phys. Rev. Lett.* **84**, 3450 (2000).

[52] F. Bert, *presented at Trieste School and Workshop on Highly Frustrated Magnets and Strongly Correlated Systems* (2007).

[53] P. Mendels, A. Keren, L. Limot, M. Mekata, G. Collin, and M. Horvatić, *Phys. Rev. Lett.* **85**, 3496 (2000).

[54] J. V. Kranendonk and M. Bloom, *Physica* **22**, 545 (1956).

[55] J. Alicea, O. I. Motrunich, and M. P. A. Fisher, *Physical Review Letters* **95**, 247203 (2005).

[56] P. W. Selwood, *Magnetochemistry*, Interscience, New York, second edition, 1956.

[57] D. C. Johnston and J. H. Cho, *Phys. Rev. B* **42**, 8710 (1990).

[58] A. Kuroda and S. Miyashita, *J. Phys. Soc. Japan* **64**, 4509 (1995).

[59] A. Keren, J. S. Gardner, G. Ehlers, A. Fukaya, E. Segal, and Y. J. Uemura, *Phys. Rev. Lett.* **92**, 107204 (2004).

[60] A. Erdélyi, W. Magnus, F. Oberhettinger, and F. G. Tricomi, *Higher Transcendental Functions*, McGraw-Hill Book Company, third edition, 1953.

השפעת הפרעות על מגנטים מתוסכלים

אורן עופר

השפעת הפרעות על מגנטים מתוסכלים

חיבור על מחקר

אורן עופר

חיבור על מחקר נעשה בהדרכת פרופ' עמית קרן

בפקולטה פיסיקה

הכרת תודה

תקציר

נוזלים צפויים להתגבש בטמפרטורות נמוכות. יוצא הדופן היחיד הידוע הוא יסוד ההליום, אשר יכול להישאר נוזל גם בטמפרטורה המוחלטת, 0 קלווין, עקב תנודות קוונטיות. באופן דומה, המומנטים המגנטים (הספינים) באטומים צפויים להסתדר בסדר ארוך טווח מתחת לטמפרטורת קירי-וייס האופיינית לכל חומר וחומר. מהבחינה הזאת, חומרים מתוסכלים מגנטית מייצגים יוצאי דופן. במערכות אלה, הסימטריה השריגית אינה מאפשרת לכל האינטראקציות המערבות זוגות של אלמנטים (ספין) להיות מסופקות בו זמנית. במערכות עם תסכול מגנטי גיאומטרי ניתן למצוא מצבי יסוד לא מסודרים עם ניוון מקרוסקופי, כלומר ניוון המכיל מספר עצום של מצבים שקולים בעלי אותה אנרגיה. ניוון מסוג זה מונע מהמערכת להסתדר במצב יסוד יחיד בטמפרטורה סופית.

בחומרים אנטי-פרומגנטיים, האנרגיה של כל זוג ספינים תהיה מינימלית כאשר הם מצביעים בכיוונים מנוגדים. לכן, במקרה של שריג משולש, זוג ספינים יכולים להסתדר בצורה הפוכה (אחד לשני) ולהותיר את הספין השלישי מתוסכל שכן הוא לא יוכל להיות הפוך לשני הספינים האחרים בעת ובעונה אחת. השאלה שאנו מתעניינים בה היא מה יקרה בסיטואציה כזו. במחקר זה נתרכז בשני שריגים שונים המבוססים על השריג המשולש, שריג הקגומה הדו-מימדי והשקול התלת-מימדי שלו, שריג הפירוכלור. השם קגומה נגזר משתי מילים יפניות קגו-מה, המשמעות היא תבנית של חורים בסלסלה: "קגו"- סלסלה, "מה"- עיניים. שריג הקגומה מבוסס על שריג משולשים החולקים קודקודים משותפים, כאשר חסר משולש בצורה אי-זוגית בשורות ובעמודות כך שנוצר למעשה מגן-דוד. שריג

הפירוכלור דומה לקגומה אולם תא היחידה בו הוא טטראהדרלי לעומת המשולש בשריג הקגומה, ניתן להסתכל על הפירוכלור כמגדל של שני שריגים מתחלפים, אחד משולש ואחד קגומה עם אינטראקציה ביניהם.

התמונה הניסיונית אינה משתלבת בצורה מושלמת עם התמונה התיאורטית. בתיאור-טית, קיומו של ניוון מקרוסקופי של מצב היסוד על פירוכלור קלאסי (גודל הספין שואף לאינסוף) מביא לחוסר סדר עד לטמפרטורה של $0K$. אולם, כל תרכובות הפירוכלור הקי-ימות, מלבד אחת, קופאות בטמפרטורה סופית. בשריג קגומה התופעה הפוכה; תיאורטית, קגומה קוונטי קופא למצב מסודר ארוך טווח בטמפרטורה אפס, לעומתו קגומה קלאסי צפוי לקפוא בטמפרטורה סופית. אולם, שוב התמונה הניסיונית מדגימה כי הקגומה הקוונ-טי היחיד - הרברטסמטייט אינו קופא.

הניוון המקרוסקופי מתקבל מהמליטוניאן הייזנברג האנטיפרומגנטי (המתאר מערכת מגנטית בסיסית) בצורה הבאה,

$$ H = J \sum_{<i,j>} \mathbf{S}_i \cdot \mathbf{S}_j = \frac{J}{2} \sum_{\Delta} \left(\sum_{i=1}^{q} \mathbf{S}_i \right)^2 - \frac{J}{2} \sum_i S_i^2 $$

כאשר הסכום הראשון הוא על משולשים (במקרה הקגומה) או טטראהדרונים (במקרה הפירוכלור). ללא הקבוע האחרון, נקבל

$$ H = \frac{J}{2} \sum_{\Delta} \mathbf{L}^2 $$

כך ש L מתאר את סכום הספינים של תא יחידה. לכן, מצב היסוד מתקבל כאשר L מתאפס. מאחר שיש מספר עצום של אפשרויות לקבל מצב שכזה, מצב היסוד מנוון מקר-וסקופית. ניוון זה מרמז על כך שהאנטרופיה בטמפרטורה אפס שונה מאפס וסופית, דבר המפר את החוק השלישי של התרמודינמיקה הטוען כי האנטרופיה של גביש מושלם של חומר טהור מתקרבת לאפס כאשר הטמפרטורה מתקרבת לאפס המוחלט (ג. לואיס ומ. רנדל, 1923) .

מפאת הניוון המקרוסקופי של המילטוניאן הייזנברג הקלאסי, המערכת המתוסכלת רגישה לאיברים נוספים בהמילטוניאן. בעבודה זו נחקור את האפשרות להסיר את התסכול

בעזרת שלושת סוגי הפרעות שונות: עיוות שריגי (דרך איבר מגנטו-אלסטי), שינוי בסו-
ספטביליות (דרך אינטראקצית דז'לושינסקי-מוריה) ואנאיזוטרופיה באינטגרל החילוף (J).
כמובן, שישנן אפשרויות שונות כגון אינטראקציה עם שכנים מסדר גבוה, או אחרים אולם
אנחנו לא נרחיב עליהם כאן.

על מנת להסיר את הניוון של מצב היסוד, הוצע כי השריג מתעוות. בעיוותים אלה, התו-
ספת באנרגיה האלסטית קטנה מההפחתה באנרגיה המגנטית. תופעה זו ידועה כאפקט
יאן-טלר, כאשר ניוון של מצב היסוד של אלקטרונים במולקולה מוסר על ידי עיוות המול-
קולה. ההבדל כמובן, הוא בכך שבמגנט מתוסכל גיאומטרית הספין המגנטי הוא הגורם
לעיוות (לעומת הניוון האלקטרוני). עיוות מגנטו-אלסטי גורם לזוגות של קשרים קצרים
וארוכים בכל תא יחידה (טטראהדרון או משולש). כאשר אינטרגל החילוף תלוי במרחק
בין הזוגות, $J = J(r)$, הקשרים הארוכים יקיימו $J_l < J$ והקצרים $J_s > J$. לכן, קשרים
קצרים יעודדו להערך בצורה אנטי-פרומגנטית (הספינים יצביעו בכיוונים הפוכים) וקשר-
ים ארוכים יתיישרו בצורה פרומגנטית (הספינים יצביעו באותו כיוון). האיבר הדו-ריבועי
המגנטו-אלסטי בהמליטוניאן נרשם בצורה,

$$\mathcal{H} = J \sum_{<i,j>} \mathbf{S}_i \cdot \mathbf{S}_j - \frac{1}{3k}\left(\frac{dJ}{dr}\right)^2 \sum_{i>j}(\mathbf{S}_i \cdot \mathbf{S}_j)^2$$

כאשר k הוא קבוע האנרגיה האלסטית (קפיץ). לכן, האיבר המגנטואלסטי גורם להתארכות
או התקצרות הקשר בין הספינים בהתאם לכיוונם היחסי והסימן של נגזרת איבר החילוף.
בצורה כזו ייתכן סדר ארוך טווח.

בעבר הודגם כי ניתן להסביר תופעות מגנטיות בעזרת אינטראקצית דז'לושינסקי-
מוריה. אינטראקציה זו יכולה לשנות משמעותית את ההתנהגות המגנטית של שריגי קגומה
ופירוכלור. איבר אינטראקצית דז'לושינסקי-מוריה (להלן, ד.מ.) הדו-לינארי נכתב בצורה

$$\mathcal{H}_{DM} = \sum_{<i,j>} \mathbf{D}_{ij} \cdot (S_i \times S_j)$$

כאשר $\mathbf{D}_{ij} \ll \mathbf{J}_{ij}$ הוא וקטור ד.מ. המתאר את האינטראקציה. ניתן להראות כי תחת

קירוב שדה ממוצע, עבור שריגי קגומה ופירוכלור, $\sum_{i \neq j} \mathbf{D_{ij}} = \mathbf{0}$, לכן אינו תורם לשינוי טמפרטורת קירי-וייס.

לבסוף, אנאיזוטרופיה של איבר החילוף באה לידי ביטוי באופן שהאינטראקציה בתוך מישור $x - y$ והאינטראקציה מחוץ למישור z אינן זהות בעצמתן. עובדה זו מתוארת בצורה הבאה

$$\mathcal{H} = -\sum_{<i,j>} J_z S_i^z S_j^z + J_\perp S_i^\perp S_j^\perp - g\mu_B \sum_i \mathbf{S}_i \cdot \mathbf{H}$$

כאשר תחת קירוב שדה ממוצע מתקבל כי המגנטיזציה הנמדדת בכיוונים שונים שונה ומביאה לטמפרטורות קירי-וייס שונות בכיוונים שונים. במקרה כזה על שריג הקגומה כל הספינים נמצאים על מישור אחד לכן ישנה זווית אחת המגדירה את כיוון הספינים המקיימת $\cos \varphi = -J_z/(J_z + J_x)$. עקב כך המומנט המגנטי לספין לאורך ציר $\hat{z}$ יהיה סופי וחיובי, לפיכך אנאיזוטרופיה של איבר החילוף על שריג הקגומה מביאה לתרומה פרומגנטית במצב היסוד.

בעבודה זו אנו חוקרים שלושה חומרים שונים, אחד בעל שריג קגומה - הרברטסמ- טייט, ושניים בעלי שריג פירוכלור - $Y_2Mo_2O_7$ (איטריום מוליבדנום חמצן ו-$Tb_2Ti_2O_7$ (טרביום טיטאניום וחמצן). ההרברטסמטייט, נקרא על שמו של הרברט סמיט, הראשון לגלותו במכרה בצי'לה בתחילת שנות ה-07. הוא נחשב לגביע הקדוש של התרכובות בעלות סימטרית הקגומה שכן הוא המימוש הראשון של שריג קגומה מושלם (ללא פגמים) עם ספין קוונטי. ההרברטסמייטט הוא בעל הצורה הכימית $ZnCu_3(OH)_6Cl_2$. והינו חלק ממשפחת הפרטקמייט $Zn_xCu_{3-x}(OH)_6Cl_2$. התכונות המגנטיות של המשפחה מתקבלות מתוך אלקטרון יון הנחושת Cu^{2+} הנושא כאמור ספין $\frac{1}{2}$. בעבודה זו משולבות מדידות תהודה מגנטית גרעינית על גרעין הכלור, מדידות מגנטיזציה ומדידות μSR. עבודות תהודה מגנטית בוצעו בקבוצות שונות בעולם על גרעינים אחרים. מתוך מדידות אלה קיימת הסכמה בקרב החוקרים כי אין הפרש אנרגיה לערור. לעומת זאת, קיים חוסר ודאות לגבי המוצא של המגנטיזציה של מישורי הקגומה. הרעיון מאחורי טכניקת הμSR היא למדוד את ההתפתחות בזמן של הספין המיואוני בחומר, דבר המתאר את את המגנטיות

של החומר. ממדידות μSR התגלה כי הרברטסמטייט אינו קופא (לפחות עד לטמפרטורה של $60mK$) ובנוסף לא התגלו עיוותים שריגיים.

הפירוכלור $Y_2Mo_2O_7$ ממשפחת ה־$A_2B_2O_7$ מהווה בעיה פיסיקלית מעניינת. חומר זה הינו מגנט מתוסכל בעל ספין 1, אשר מבצע מעבר פאזה לזכוכית ספינית בטמפרטורה קריטית של כ־$22K$, מה שרומז על סוג של אי סדר שמקורו אינו ידוע. אי סדר זה עשוי להיגרם על ידי עיוות של השריג. קיימות לכך ראיות ניסיוניות קודמות לדוגמא, ניסוי $XAFS$ המראה על אי סדר באורך הצלע של טטרהדרוני המוליבדנום וניסוי μSR המדגים כי קיימת התפלגות רחבה מאוד של שדות פנימיים בחומר. בעבודה זו המשכנו ניסוי של תהודה מגנטית לטמפרטורה הקרובה לטמפרטורת מעבר הפאזה. התגלה כי קיימת התפתחות לשני (ייתכן אף שלושה) אתרי Y לא זהים. מדידות של קרני X ברזולוציה גבוהה לא גילו בצורה חד משמעית שינויים מבניים.

הפירוכלור $Tb_2Ti_2O_7$ ייחודי במשפחת הפירוכלורים בכך שהוא מהווה נוזל ספיני; למר- ות קורלציות אנטיפרומגנטיות המתפתחות בטמפרטורה הנמוכה מ $100K$, $Tb_2Ti_2O_7$ נשאר במצב פארמגנטי עד לפחות לטמפרטורה של $70mK$. בעבר הוצע כי מנגנון מסוג מגנטו־אלסטי גורם לסדר ארוך טווח הנגרם תחת לחץ אנאיזוטרופי. במחקר על חומר זה השתמשנו בטכניקת הμSR על מנת לבדוק האם ייתכן כי חוסר קיומו של מנגנון מגנטו-אלסטי הוא הגורם לכך שהחומר אינו קופא. התברר כי אין עדות לעיוותים בשריג בסקלת הזמן של ה μSR שהיא 1.0 מיקרושנייה.

העבודה מאורגנת כדלקמן. בפרק 1 אנו מביאים הסברים תיאורטיים לשני השריגים המתוסכלים, הקגומה והפירוכלור עם תמצית על התרכובות שעליהם מתבססת עבודה זו. פרק 2 דן באמצעים ובטכניקות המדידה השונות שאיפשרו ביצוע מדידות שונות ומדויקות של התרכובות. לבסוף בפרק 3 אנו מציגים ומנתחים את תוצאות המדידה.